I. EQUILIBRIUM AND NON-EQUILIBRIUM SUPERCONDUCTING QUANTUM INTERFERENCE PHENOMENA

II. APPLICATIONS OF SUPERCONDUCTING QUANTUM MAGNETOMETER

Thesis by

Run-Han Wang

In Partial Fulfillment of the Requirements

for the Degree of

Doctor of Philosophy

California Institute of Technology

Pasadena, California

1975

(Submitted June 26, 1974)

ACKNOWLEDGMENTS

It is a great pleasure to express my profound gratitude to my adviser, Professor J. E. Mercereau for his invaluable suggestions, constructive criticism and inspiring guidance throughout the course of this research. I wish to thank Dr. H. A. Notarys for his assistance and experienced advice which have always exceeded the level of my expectation, and also for his pioneer work in the quantum interference effects.

For their most valuable helps and enlightening conversations, I wish to express my deep appreciation to those who directly collaborated with me on the various projects. But to do this adequately proves no simple task, among those I would like to specifically thank are:

Dr. H. E. Hoenig of Physikalisches Institüt at Frankfurt for his instrumental help in the early stage of the work on applications of magnetometer and the fluctuation experiment; Professors H. B. Gray, G. R. Rossman, and E. H. Shoemaker for bringing my attention to the fields of magnetochemistry and paleomagnetism respectively and for sharing many informative discussions with me; Professor M. Cerdonio of the Institute of Physics at Rome for his enthusiasm and the fruitful collaboration during the latter stages of the magnetochemical research; Professor M. Delbruck for his illuminating introduction on the subject of vision; Dr. G. J. Dick for his kind help in electronics.

This work was made possible by the various samples prepared and furnished to me at different phases of the research. Special thanks go to Professor R. D. Parks of University of Rochester for his generous

offer of $La_{3-x}Ga_xIn$ samples for the fluctuation experiment; Drs. C. A. Root and R. C. Rosenberg for the Carboxypeptidase A protein; Dr. J. W. Dawson for the Hemerythrin sample; and Dr. H. A. Notarys for sharing his interferometers with me.

Many thanks are extended to Dr. M. L. Yu for his extensive help. I have received tremendous benefit from constant and stimulating discussions with my colleagues and from their in-depth suggestions and advice, both solicited and unsolicited. In particular I am indebted to S. K. Decker, T. Ganz, and D. W. Palmer in the friendly environment of the "Bosonics" Laboratory, and H. C. Yen of the "Hippodrome".

The ever-ready technical assistance provided by Edward Boud and Sandy Santantonio are gratefully acknowledged. I am also immensely grateful to Fred Wild for going out of his way in preparing and repairing the glass apparatus, and to Miss G. Kusudo for her kind assistance and warm friendship.

To the co-authors, I wish to thank them and the Institute of Electrical and Electronics Engineers for their permission to use the published paper reproduced in Part II of this thesis. I would like to thank the National Academy of Science for permission to use Figs. 1 and 2 (of Part II) which appeared in Proc. Nat. Acad. Sci. USA, Vol. 70, 1973. The careful and excellent typing of this thesis is due to Mrs. Kathy Ellison.

My graduate study has been made financially possible by grants from the Office of Naval Research. This work was also supported in part by IBM and Caltech President's Fund provided by NASA.

Finally, I would like to thank my parents for their loving care and their teachings, and my deepest gratitude to my wife, Susie, for her encouragement and patience in bearing the trials and tribulations of a student husband for all these years. And to them I dedicate this thesis.

ABSTRACT

Experimental investigations were made on the equilibrium and non-equilibrium quantum interference phenomena in superconductors. A new instrument was developed for measuring magnetic susceptibility and moment with an improvement of sensitivity of nearly two orders of magnitude over the conventional magnetometers.

A quantitative determination was made on the relaxation rate of a perturbed superconducting phase to relax back to its equilibrium state. The temperature-dependent relaxation time is found to be consistent with the known quasiparticle relaxation time in nonequilibrium superconductors. The effect of relaxation processes on macroscopic quantum interference phenomena was observed for the first time through the temperature modulation of quantum interference in multiply connected superconducting circuits, and implies a modification of the Josephson frequency-voltage relationship. A relaxation model was developed and found adequate to account for nearly all the experimental results.

The development and performance of an ultrasensitive superconducting magnetometer instrument based on various unique properties of superconductors were discussed. Applications of this instrument over a temperature range of 200°K in the fields of magnetochemistry, paleomagnetism and the study of fluctuation effects in superconductivity were illustrated with actual data.

TABLE OF CONTENTS

	Page
ACKNOWLEDGMENTS	iii
ABSTRACT	vi
GENERAL INTRODUCTION	1
PART I SUPERCONDUCTING QUANTUM INTERFERENCE PHENOMENA	4
Chapter 1 Equilibrium and Non-equilibrium Superconductivity	4
1.1 Superconducting Phenomena	4
1.2 The Electrochemical Potential in Superconductor	6
1.3 Fluxoid Conservation in Superconducting Rings	9
1.4 Macroscopic Quantum Phenomena	11
Chapter 2 AC Quantum Interference Phenomena in Superconductors	16
2.1 Introduction	16
2.2 Fabrication of Proximity Effect Bridges and Quantum Interferometers	17
2.3 Electrical Characteristics of Proximity Effect Bridges	22
2.3.1 General Characteristics	22
2.3.2 The DC and AC Josephson-like Effects	23
2.4 Superconducting Quantum Interferometer	25
2.4.1 Josephson Junction and Josephson Junction Interferometer	25
2.4.2 Normal Conducting Ring	30

Page

2.4.3 Interferometer with a Proximity Effect Bridge 31

2.4.4 Quantum Transitions and Superconducting Dissipations 35

2.4.5 Circuit Analysis 39

2.4.6 Experimental Considerations and Measurements 50

2.4.7 Experimental Results 54

(A) DC and RF Characteristics 58

(B) Temperature Dependence 61

(C) Parametric Impedance 64

(D) Temperature-Modulated Signal near the Transition Tempature 70

2.5 Non-equilibrium Superconductivity 72

2.5.1 Non-equilibrium Processes in Superconductors 72

(A) Thermalization 73

(B) Branch Mixing 73

(C) Recombination of Quasiparticles 74

2.5.2 The Two-Potential Concept 74

2.5.3 Non-equilibrium Quantum Interference Phenomenon 77

REFERENCES 100

Page

PART II APPLICATIONS OF SUPERCONDUCTING QUANTUM MAGNETOMETER 103

Introduction 103

Chapter 1 Magnetochemical Studies 105

1.1 The Nature of the Magnetobiochemical Problem 105

1.2 The Superconducting Magnetometer and its Performance 107

1.2.1 Introduction 108

1.2.2 Experimental Apparatus 108

1.2.3 Experimental Procedures 109

1.2.4 Tests of the System 110

1.2.5 System Performance 110

1.2.6 Biochemical Studies 111

1.2.7 Stereochemical Identification 113

1.3 General Experimental Considerations 117

1.3.1 The Effect of Temperature Variations on Penetration Depth 117

1.3.2 Paramagnetic Materials and Thermal Contractions 117

1.3.3 Johnson Noise and Eddy Current in Copper Shield 118

Chapter 2 Paleomagnetism and Fluctuation Effects in Superconductivity 120

2.1 Paleomagnetism 120

2.1.1 Reversal of the Earth's Magnetic Field 120

Page

2.1.2 Paleomagnetism and Superconducting Magnetometry 121

2.2 Fluctuation Effects in Superconductivity 122

REFERENCES 124

GENERAL INTRODUCTION

Superconductivity is a macroscopic quantum effect. This important concept was first introduced by F. London[1]. In this state a macroscopic number of electrons condense into a single state in the momentum-space represented by a single wave function $\psi \sim e^{i\phi}$ which extends throughout an entire macroscopic sample. Although the absolute phase of the wave function ψ has no meaning, the phase differences ϕ can be determined: fixing the value of the phase at one point determines its value at any other point in the superconductor. It is the phase of ψ which establishes the long-range ordering throughout a superconductor. Many interesting phenomena are manifested by this condensate. Below the transition temperature a type I superconductor abruptly loses its dc electrical resistance and expels magnetic field from its interior -- a perfect diamagnet.

When two superconductors are completely isolated from each other, the phases of ψ in each are free to alter arbitrarily. As in a capacitor, an applied voltage between the two pieces of superconductors results in no real current flowing between them. On the other hand, if two superconductors are tightly pressed together, a supercurrent can flow without developing a voltage. In between these two extreme cases of purely capacitive and conductive effects for de-coupled and strongly coupled superconductors respectively, the "weakly coupled" superconductors exhibit some fascinating phenomena. Two superconductors are weakly coupled if there is a small local reduction of the strength of superconductivity compared to the neighboring superconductors. When the

thickness of a barrier of normal metal or insulator between the two superconductors is gradually reduced to zero, it may be reasonable to expect the properties of the system of two isolated superconductors to change continuously to those of a single superconductor. In 1962 Josephson[2] found that the coupling energy which is a periodic function of the phase difference increases as the two superconductors are brought closer and closer until the phases of the two pieces are effectively locked together. Weakly coupled superconductors possess two characteristic effects: an ac supercurrent resulting from a dc voltage across the weak link and quantum interference effect in a magnetic field.

Historically, weak coupling has been achieved experimentally by means of a tunnel junction (SIS). Tunneling is not essential to the Josephson effect[3]. Weak links or bridges can also take the form of a superconducting/normal/superconducting junction (SNS) where the local normal state is effected either by a normal metal[4] or a current-induced breakdown of the superconducting state[5]. In addition to the existence of a single macroscopic quantum state in a superconductor and a weak link, the theoretical criterion for the degree of weak coupling in Josephson junction is that the coupling energy be strong enough to overcome the thermal energy and the zero point energy[6]. The coupling energy is the energy needed to maintain internal phase coherence of the superconducting electrons.

The contents of this thesis fall into two parts. Part I of this work deals with macroscopic superconducting quantum interference phenomena in multiply connected superconductors. We first give an

account of the equilibrium fluxoid quantization in a multiply connected superconducting ring. This is followed by an analysis of the quantum interference behavior of a superconducting ring containing a weak link. The effects of the electrical, magnetic, and chemical potentials are examined for a multiply connected circuit with special emphasis on situations in which pairs and single electrons may have separate electro-chemical potentials. A model is developed which analyzes the response of a weakly connected superconducting ring in terms of these potentials as well as the characteristic parameters of the circuit. The general functional dependence of the interference phenomenon on the physical parameters, frequency, critical current, resistance of the junction, and inductive impedance of the superconducting ring is given in terms of an equivalent circuit. Experimental technique is presented and experimental results are compared with analysis.

In Part II of the thesis we describe the development of these unique and remarkable properties of superconductors into a sensitive superconducting magnetometer instrument. As an illustration of the performance of this instrument we discuss the application of the magnetometer to the study of metalloproteins. This includes the significance of magnetic susceptibility data, the experimental set-up and unique features of the superconducting magnetometer, the measuring technique and the implication of the result. Finally, the possible applications of such an instrument in various other scientific disciplines such as physics, geology and biology will be indicated.

PART I

SUPERCONDUCTING QUANTUM INTERFERENCE PHENOMENA

CHAPTER 1

EQUILIBRIUM AND NON-EQUILIBRIUM SUPERCONDUCTIVITY

1.1 Superconducting Phenomena

An ideal type I superconductor exhibits zero dc electrical resistance and is a perfect diamagnet (Meissner effect) when it is below its transition temperature T_c and critical magnetic field $H_c(T)$[7]. Gorter and Casimir[8] proposed a two fluid model in which a fraction $f_s = n_s/n$ of the conduction electrons was condensed into a zero entropy condensate while a fraction $f_n = n_n/n$ remained as "normal" electrons and

$$n = n_s + n_n \quad , \qquad (1\text{-}1)$$

where n, n_s and n_n are densities of total conduction, super- and normal electrons respectively. F. London introduced the idea that superconductivity is a coherent macroscopic quantum state. The condensation of a macroscopic number of electrons into a single quantum state means that a single wave function

$$\psi(\vec{r},t) = \sqrt{\rho_s}\; e^{i\phi(\vec{r},t)} \quad , \qquad (1\text{-}2)$$

can be used to represent the collective behavior of an enormous number of electrons all of which share the same phase ϕ. In this sense Ginzburg and Landau (G-L)[9] interpreted $\psi^*\psi$ as the local density of the Cooper pairs.

$$\rho_s = |\psi|^2 = \frac{1}{2} n_s \quad . \qquad (1\text{-}3)$$

Upon substituting this wave function into the usual expression for quantum mechanical current density, the supercurrent density is given by

$$\vec{J}_s = \frac{2\hbar q^* \rho_s}{m^*} \vec{\nabla}\phi - \frac{2q^{*2} \rho_s}{m^*} \vec{A} \quad , \qquad (1\text{-}4)$$

where the effective mass $m^* = 2m$ and charge $q^* = 2q$ are twice that of a normal electron respectively, $2\pi\hbar$ = Planck's constant and $\vec{A}$ the magnetic vector potential. By taking the curl of Eq. (1-4), we obtain the Meissner effect. The magnetic field decays to zero over a penetration depth

$$\lambda(T = 0°K) \sim 10^{-5} \text{ cm} \quad .$$

Frohlich[10] first proposed that the basic mechanism of superconductivity was a phonon mediated electron-electron attractive interaction. In 1956 Cooper[11] discovered a basis for such an interaction in that the ground state of quasiparticles can be unstable with respect to the formation of bound pairs of electrons. Bardeen, Cooper and Schrieffer (BCS)[12] in 1957 advanced a successful microscopic theory of superconductivity based on this idea. In this theory a macroscopic number of electrons pair together in the same center of mass momentum state, resulting in a lowering of their individual energy by an amount known as the gap energy or the pair potential $\Delta(T = 0) \sim kT_c \sim 10^{-4}$ eV per electron. The mean separation between the bound electrons in a pair or the range of their momentum coherence is expressed by the "coherence length", $\xi(T = 0) \sim 10^{-4}$ cm which is orders of magnitude longer than the interatomic spacing. Hence the scattering of Cooper pairs by lattice or

impurity conserves the total momentum of the pair and there is no resistance (de-pairing requires a minimum amount of energy $2\Delta(0) \sim \hbar v_F/\xi(0)$ supplied to the Cooper pair). Within a sphere of diameter ξ there are some 10^6 other Cooper pairs. The strong overlap of such a large number of pair wave functions extending through individual spheres of diameter ξ results in correlation in phase of the pair wave-function and establishes long-range ordering throughout the entire piece of superconductor. In this way the large coherence length gives rise to the macroscopic coherent nature of a superconductor. The temperature dependence of ξ, λ and Δ are as follows:

$$\xi(T) \propto \lambda(T) \propto \Delta^{-1}(T) \propto (T_c - T)^{-\frac{1}{2}} \quad T \lesssim T_c \qquad . \qquad (1\text{-}5)$$

Gorkov[13] has identified the G-L wavefunction to be proportional to the BCS pair potential.

1.2 The Electrochemical Potential in a Superconductor

Gorkov[14] first noted the special role of Fermi level in the phenomenology of superconductivity. He noted that unlike normal metals, the chemical potential in a superconductor is not only a macroscopic thermodynamic variable but also can be thought of as a microscopic variable determining the local state, which is coupled to the rest of the superconductor by the long-range ordering. In terms of the pair electrochemical potential $\bar{\mu}_p$, the pair wave function in the absence of an applied magnetic field can be written as

$$\psi = \sqrt{\rho_s}\ e^{-\int 2i\bar{\mu}_p dt/\hbar} \quad . \qquad (1\text{-}6)$$

The pair electrochemical potential $\bar{\mu}_p$ is defined relative to the chemical potential of the pair μ_p by

$$\bar{\mu}_p = \mu_p + qV \quad , \qquad (1\text{-}7)$$

where q is the charge of the electron and V the electrostatic potential. Physically $\bar{\mu}_p$ is half the energy necessary to add a Cooper pair isothermally to a superconductor kept at constant volume and at a potential V. From Eqs. (1-6) and (1-7) $\bar{\mu}_p$ can be identified as[15]

$$\bar{\mu}_p = \frac{i\hbar}{4|\psi|^2}\left(\psi^* \frac{\partial\psi}{\partial t} - \frac{\partial\psi^*}{\partial t}\psi\right) \quad , \qquad (1\text{-}8)$$

and physically is related to the average "frequency" of the macroscopic state. At thermal equilibrium, the electrochemical potential of the pairs $\bar{\mu}_p$ and of the quasiparticles (normal electrons) $\bar{\mu}_e$ are the same everywhere and $\bar{\mu}_p = \bar{\mu}_e$.

However, perturbations of the condensate[16] and/or quasiparticles[17] may cause a non-equilibrium situation in which $\bar{\mu}_p \neq \bar{\mu}_e$. Experimentally such a situation might be generated by any (or combinations) of the following processes: thermal or photon excitation[18], external injection of quasiparticle at a S/N interface[19] or inside a proximity effect bridge, and spatial variation of the pair density[20].

For small perturbation of the equilibrium system, it is assumed that the concept of local equilibrium is still valid. That is, the intensive parameters like temperature, pressure and electrochemical potential vary sufficiently slowly with position that they can be

regarded as spatial constants over a region with a characteristic distance Λ large enough to contain many particles. Each such small volume element is a thermodynamic phase and it is labeled by a position coordinate. This assumption implicitly implies that the concept of energy gap and excitation spectrum can be defined on a local basis. In addition, these parameters must vary sufficiently slowly in time that within the thermodynamic phase they remain close to equilibrium. Viewed microscopically, the condition for local-equilibrium concept to be valid is that the time in which an intensive parameter changes by a significant amount must be very long compared with some relaxation time τ associated with the interaction with other phases to re-establish a near-equilibrium state.

To describe the non-equilibrium behavior of a system, it is assumed that (1) the local-equilibrium concept is valid and that (2) intensive and extensive parameters may depend on position, and (3) currents generated by the spatial gradients of the intensive parameters exist and interconnect the phases[21]. Although the currents depend on the space derivatives of intensive parameters to first order, the spatial dependence of the state functions of the phase (e.g. the internal energy and entropy) is only of second order.

The characteristic distance Λ, beyond which the intensive parameter begins to vary appreciably, and the characteristic time τ may vary depending upon the relaxation processes involved and the mean free path of the quasiparticles ℓ. In the course of his investigation of non-equilibrium processes at S/N interface, Yu[20] found that the typical time

scales for various relaxation processes are of the order $\tau \lesssim 10^{-10}$ sec. Since all the electrons involved are near the Fermi surface, the distance over which the non-equilibrium process propagate in a thin film (e.g. Sn) with $\ell \sim 100$ Å is roughly $(v_F \ell \tau)^{1/2} \lesssim 1$ μ where the Fermi velocity is $v_F \sim 10^8$ cm/sec.

The original BCS and G-L theories were formulated for equilibrium properties in superconductivity. Although the validity of some of the above postulates has yet to be justified, some theoretical extensions of the equilibrium theories into the non-equilibrium regime have been made[17,22] based on these assumptions. One important concept put forward by Rieger, Scalapino and Mercereau is that as a consequence of a perturbation on the condensate, the electrochemical potential of the pairs $\bar{\mu}_p$ need not be the same as that of the quasiparticles $\bar{\mu}_e$. Experimental results from the local conversion of quasiparticle current into a pair current in a S/N interface and a quantum mechanical interference effect in a superconducting proximity effect bridge[19,20] lend support to this concept. Another manifestation of the quantum phase effects, when the proximity effect bridge is shorted by a superconducting inductor, will be treated in detail in Chap. 2.

1.3 Fluxoid Conservation in Superconducting Rings

In 1948, London[23] suggested that the "fluxoid" or the action integral, $\oint \vec{P} \cdot d\vec{r}$ taken around a superconducting ring (where $\vec{P}$ is the canonical momentum of the superconducting electrons) should be both conserved and quantized. The fluxoid consists of the mechanical angular momentum of the electrons and the magnetic flux trapped by the ring.

If the non-dissipating supercurrent density (Eq. 1-4) is written as $j_s(T) = n_s(T)qv_s$, then $\hbar\nabla\phi$ is just the canonical momentum of the condensate. The application of Bohr-Sommerfeld quantization condition to the canonical momentum of the pairs is equivalent to the requirement that the pair wave function (Eq. 1-2) be single valued when the phase is integrated along any closed path in the superconductor. In this situation Eq. (1-4) becomes

$$\frac{q^*}{h}\Phi_c \equiv \frac{1}{h}\oint\left(m\vec{v} + q^*\vec{A}\right)\cdot d\vec{r} = \frac{1}{h}\oint\vec{P}\cdot d\vec{r} = n \quad , \qquad (1\text{-}9)$$

where n is an integer and h is Planck's constant. This idea has been experimentally confirmed and $q^* = -2e$ has been found to be twice the electron charge -e.[24]

Deep inside a thick superconducting ring (thickness $\delta >> \lambda$) the current is zero due to the Meissner effect and the mechanical angular momentum ($v_s = 0$) contribution to the fluxoid is negligible compared to the magnetic flux term. Equation (1-9) then leads to quantization of the trapped magnetic flux Φ

$$\Phi = \oint\vec{A}\cdot d\vec{r} = n\Phi_o \quad , \qquad (1\text{-}10)$$

where the fundamental unit of quantum flux Φ_o is

$$\Phi_o = \frac{h}{2e} = 2.07 \times 10^{-7}\ \text{G-cm}^2 \quad . \qquad (1\text{-}11)$$

For a thin superconducting ring with thickness $\delta << \lambda$, fluxoid conservation implies that a temperature variation changes the relative contribution of the mechanical and electromagnetic angular mementa. In this

case the magnetic flux reduces to[25]

$$\Phi = n\Phi_o \left(1 + \frac{2\lambda^2(T)}{r\delta}\right)^{-1} \quad , \qquad (1\text{-}12)$$

where r is the radius of the ring. Consequently, though the amount of the trapped flux may vary with temperature, the fluxoid is adiabatically invariant as has been experimentally verified[26].

1.4 Macroscopic Quantum Phenomena

The macroscopic coherent nature of the superconducting state can be characterized by representing $\sim 10^{22}$ electrons/cm^3 by a single pair wave function Eq.(1-2). The existence of this wave function ψ, common to a single continuous block of superconductor, entails at a given moment a definite value of the relative phase between any two points in the superconductor. In fact, the superconducting condensation energy results entirely from this precise phase coherence though the total phase of the sample as a whole is meaningless. One of the many consequences of phase coherence is the fluxoid quantization.

For a traslationally invariant system, the energetically favorable BCS pairing for supercurrent-carrying state is

$$[(\vec{k} + \vec{q}/2)\uparrow, \ (-\vec{k} + \vec{q}/2)\downarrow] \quad ,$$

with a resultant electron net drift velocity $\vec{v}_d = \hbar\,\vec{q}/2m$ so long as $\hbar q < 2\Delta/v_F$. The orbital wave function of the pair can be represented by[27]

$$\psi(\vec{r}_1,\vec{r}_2) = \phi_q(\vec{r}_1 - \vec{r}_2)\, e^{i\vec{q}\cdot\vec{R}} \quad , \qquad (1\text{-}13)$$

where $\vec{R} = (\vec{r}_1 + \vec{r}_2)/2$ is the center-of-mass (C.M.) coordinate and $\vec{q}$ is, in general, the C.M. canonical momentum. The exponential factor in Eq. (1-4) represents a traveling wave of the pair with the de Broglie wavelength $\lambda = 2\pi/q$. For a drift velocity $v_d \sim$ a few cm/sec, the associated de Broglie wavelength λ of the pair is roughly $\sim$1 cm as examplified in the case of a persistent current in a ring. This very long range coherence is a consequence of the strong overlap of the Cooper pairs.

The time evolution of the relative phase $\Delta\phi$ (Eqs. 1-2 or 1-6) in a superconductor is determined by the electrochemical potential difference $\Delta\bar{\mu}_p$ according to the de Broglie relation $\omega = E/\hbar$:

$$\Delta\dot{\phi} = \omega = -2\Delta\bar{\mu}_p/\hbar \quad , \qquad (1\text{-}14)$$

where $\Delta\bar{\mu}_p$ is usually identified with an applied voltage difference V through $\Delta\bar{\mu}_p = qV$. The lack of temporal phase difference, $\Delta\dot{\phi} = 0$, implies inside a bulk superconductor at a steady state the electrochemical potential is everywhere the same, i.e. $\Delta\bar{\mu}_p = 0$. This together with Eq. (1-4) leads to

$$\vec{J}_s = -\frac{2n_s q^2}{mc}\vec{A} \quad , \qquad (1\text{-}15)$$

and hence the macroscopic quantum effects of zero dc electric resistance, perfect diamagnetism and persistent current in a ring are recovered.

Although the macroscopic quantum phenomenon and the current-phase difference relationship of the superconductor were well known, it was Josephson who first recognized that the intrinsic time dependence of

the phase difference had observable effects for two weakly coupled superconductors[2]. The original theoretical prediction was made for electrons tunneling from one superconductor to the other through a thin oxide layer.

The supercurrent density j_J in a Josephson junction is proportional to the sine of the gauge-invariant phase difference $\Delta\tilde{\phi}$ between the two macroscopic wave functions associated with superconductors on both sides of the junction:

$$j_J = j_o \sin \Delta\tilde{\phi} \quad , \qquad (1\text{-}16)$$

where the amplitude of the wave function of finding an electron on either side (1 or 2) of the junction are given by

$$\psi_j(\vec{r}_j) = \sqrt{\rho_j}\; e^{i\phi_j(\vec{r}_j,t)} \qquad j = 1,2 \quad , \qquad (1\text{-}17a)$$

$$\psi_j(\vec{r}_k) = \psi_j(\vec{r}_j) e^{i\frac{2q}{\hbar}\int_{r_j}^{r_k} \vec{A}\cdot d\vec{r}} \qquad j,k = 1,2 \quad , \qquad (1\text{-}17b)$$

and

$$\Delta\tilde{\phi} = \phi_2 - \phi_1 - \frac{2q}{\hbar}\int_1^2 \vec{A}\cdot d\vec{r} \quad . \qquad (1\text{-}18)$$

When the critical current J_o of the junction is exceeded, a finite voltage developed across the junction. The supercurrent oscillates with a frequency given by the Josephson frequency-voltage relationship of Eq. (1-14). In terms of the gauge-invariant electrochemical potential difference of the pair $\Delta\tilde{\mu}_p$, the second Josephson equation becomes

$$\Delta\dot{\tilde{\phi}} = -\,2\,\Delta\tilde{\mu}_p/\hbar \qquad , \qquad (1\text{-}19)$$

whereupon dropping the subscript "p" from $\bar{\mu}_p$

$$2\Delta\tilde{\mu}_p = 2(\bar{\mu}_2 - \bar{\mu}_1) + 2q\int_1^2 \frac{\partial\vec{A}}{\partial t}\cdot d\vec{r} \qquad . \qquad (1\text{-}20)$$

The supercurrents in different parts of the Josephson junction can be forced to interfere by applying an external magnetic field. This dc quantum interference effect was elegantly demonstrated in the configuration of two Josephson junctions connected in parallel by Jaklevic et al.[28] The total Josephson current through the symmetric dc interferometer has the form

$$I_T = 2I_o \frac{\sin e\Phi_J/\hbar}{e\Phi_J/\hbar} \cos\,(e\Phi_T/\hbar) \qquad , \qquad (1\text{-}21)$$

where Φ_J is the flux in the junction and Φ_T is the flux enclosed by the dc interferometer. The quantum mechanical interference between the currents flowing through separate junctions, $\cos(e\Phi_T/\hbar)$, in analogy to the double-split interference phenomenon in optics, has been observed in interferometers with apertures as large as 3 cm^2.

If an electrochemical potential difference is established by an applied voltage V across the junction

$$V = V_o + V_1 \cos\,\omega t \qquad , \qquad (1\text{-}22)$$

the ac voltage would phase modulate the Josephson oscillations. Expanding Eq. (1-16) into a Fourier-Bessel series would give

$$j_s = j_o \sum_{m=-\infty}^{\infty} J_m(2eV_1/\hbar\omega)\,\sin\,[\phi_o + (m\omega + 2eV_o/\hbar)] \qquad , \qquad (1\text{-}23)$$

where J_m is the m^{th} order Bessel function and ϕ_0 is the phase angle between the ac field V_1 and the spontaneous Josephson current at frequency $2eV_0/h$. In particular, whenever $2eV_0/\hbar\omega = m$, an integer, the current is perfectly periodic with frequency $\omega/2\pi$. Under suitable conditions, in the presence of a slight change of applied V_0 or ω_0 the system can accommodate itself by adjusting ϕ_0 so as to lower its free energy. Such ac synchronization results in current steps on the I-V characteristics and has been observed by Shapiro[29]. To summarize: as long as the superconductor can be characterized as a macroscopic quantum state, dc and ac Josephson effects result from the requirement of phase coherence across a weak link.

Having briefly reviewed the properties of a superconducting ring and the Josephson effect, we will consider the behavior of a superconducting ring interrupted by a single Josephson junction or a weak link in an external electromagnetic field -- the ac superconducting quantum interferometer.

CHAPTER 2

AC QUANTUM INTERFERENCE PHENOMENA IN SUPERCONDUCTORS

2.1 Introduction

If a superconductor S is superimposed on a normal metal N so that there is a good electrical contact between the two, Cooper pairs from the superconductor can leak to the normal metal. The superconducting order parameter falls off exponentially from its full strength deep inside S to zero over a decay length typically $\sim 10^3$ Å or longer in the normal metal. This proximity effect provides a region in N where supercurrent and normal current can coexist. Unlike the oxide junction, the comparatively long-range proximity effect allows one to study the non-equilibrium pairing and depairing processes inside the conversion region with well-defined chemical composition and reproducible characteristics.

Experimentally it has been found that when two S/N interfaces are brought together to form a S/N/S structure with the two S regions being about one micron apart, phase coupling between the wave functions of the two strong superconductors is established through the N region. Quantum phase coherence and interference effects in these "proximity effect bridges" result in Josephson-like phenomena. Other than the oxide junction, a number of metallic weak link structures also exhibit Josephson-like effects[6,31]. A common feature of such metallic weak links is the existence of a small inhomogeneous region where the magntiude of the superconducting order parameter is reduced as compared

to the neighboring superconductors. An electrical current above the critical current of the bridge can develop a voltage between the two superconductors with resulting supercurrent oscillating at a frequency given by Eq. (1-14). In earlier investigations[20,30] of the time dependent superconducting state inside the weak link region, the voltage sustaining state was brought about by a dc current bias in the weak link. In the present work some details of non-equilibrium quantum interference effects are examined by establishing the electric field inside the weak link by an external time-varying magnetic field. This configuration consists of a weak link interrupting an otherwise superconducting thin film cylinder - an rf quantum interferometer - inductively coupled to an rf tank circuit.

In this chapter we will describe the fabrication of the proximity effect bridge used and briefly summarize its electrical characteristics and results from earlier investigations. This is followed by a discussion of possible non-equilibrium processes and measurements made on the superconducting quantum interferometer. A physical model will be presented to account for observed effects.

2.2 Fabrication of Proximity Effect Bridges and Quantum Interferometers

Two techniques have been developed to produce a normal region in a S/N/S structure. The first one is simply to use either a normal metal or a superconductor above its transition temperature as the center of a "sandwich" structure. The second is realized by a current-induced breakdown of the superconducting state in a small "weak" region contained

in a larger structure; where "weak" is defined as having a transition temperature (T_c') less than that (T_c) of the neighboring strong superconductors. Selective weakening can be achieved via the proximity effect. When a normal film or a "weaker" superconducting film with transition temperature, T_{cn}, is superimposed on a superconducting film with transition temperature $T_{cs} > T_{cn}$, the transition temperature of the resulting composite film depends on the relative thicknesses t_n and t_s of the films and the materials used. In very thin films, probably due to variations in structure, T_c also varies with thickness of the film.

A structure of superconducting refractory metals (eg. Nb, Ta, Hf, Zr) in a multi-layer form has been developed by Notarys and Mercereau[5] as a system with which to study non-equilibrium quantum interference effects. The configuration of the weak coupling region or "bridge" is shown in Fig. 2.1a. At the inhomogeneous bridge area, part of the film with higher transition temperature ($T_{cs} > T_{cn}$) has been removed so that due to the proximity effect the thickness ratio t'_s/t'_n renders a lower transition temperature $T_c' < T_c$ of the composite film. The fabrication of the most extensively used Nb/Ta structure will be described.[54]

To prepare the superconducting substrate, 200 Å Ta is first evaporated on a rotating, clean sapphire rod (3 mm in diameter) heated to 400°C and this is immediately followed by deposition of 100 Å Nb in an ultra high vacuum system (pressure $\sim 10^{-8}$ mm Hg). Removal of thin-film refractory superconductor by anodization provides precise control

and reproducibility in physical configuration and characteristics of proximity effect bridges. The metal oxide resulting from anodization forms a strong protective insulator tenaciously adhering to both the metal and the sapphire substrate. The thickness of the oxide layer formed is proportional to the applied voltage with a rate of about 15 Å/V which corresponds to the removal of Ta at 8 Å/V or Nb at 6 Å/V. Hence this technique allows thickness control to a few Angstroms.

The operation of the S/W/S proximity effect bridge depends on the overlap of the two wave functions induced in the weak region. The typical length along the current flowing direction of the bridge, ℓ', for phase coherence phenomena to occur is about one micron. Such fine structures ($\ell' \gtrsim 0.3\ \mu$, the resolution limit of the optical microscope) can be fabricated on these superconducting substrates by photoresist masking and anodization techniques. To prepare the bridge, the superimposed film is first coated with a thin layer of positive photoresist ($\lesssim 1\ \mu$) and a fine line ($\sim 1\ \mu$) is exposed across the film by the reduced image of a mask in the optical path of a microscope. A drop of weak electrolyte (boric acid) is applied to the exposed line of the film. Gold wire immersed in the electrolyte is used as the cathode and copper wire attached to the film by silver paint serves as the anode lead. The film is anodized by a voltage of proper wave form and duration. The quantum interferometer can be shaped by selective anodization of the film into its final form (Fig. 2.1b). Nearly all the interferometers investigated in the course of this work were prepared

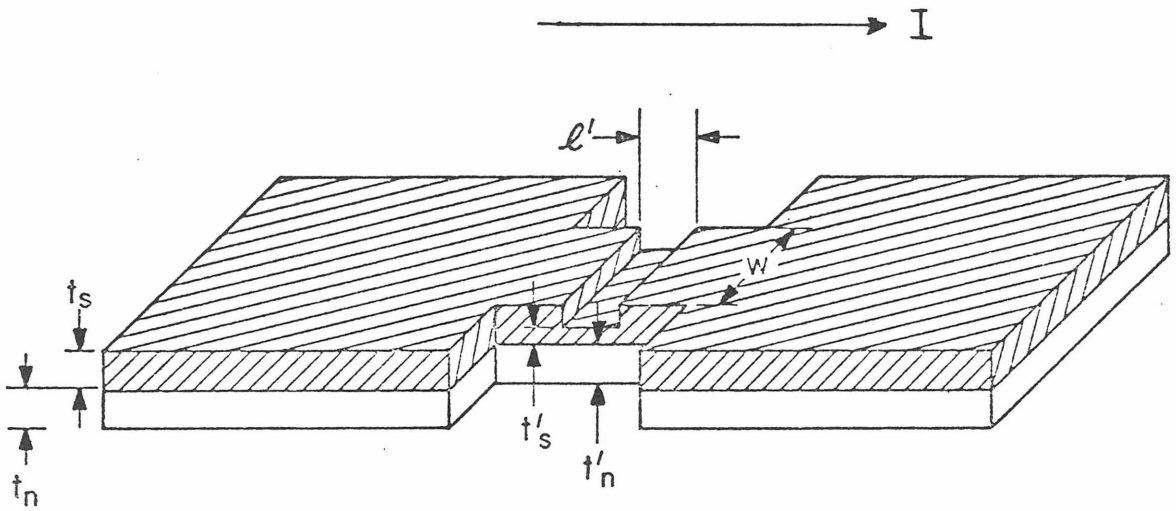

Fig. 2.1a Schematic drawing of proximity effect bridge constructed from two-layer thin film substrate (Nb on Ta). t_s and t_n are the thicknesses of superconducting films of higher and lower transition temperatures (T_{cs} and T_{cn}) respectively. The bridge region has a local thickness ratio t'_s/t'_n, length ℓ' along the current I direction, width W, and a lower transition temperature T'_c than the adjoining region T_c.

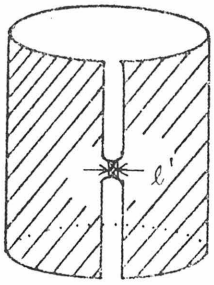

Fig. 2.1b Diagram of superconducting quantum interferometer consisting of a superconducting thin film cylinder (typically ~ 1-3 mm in diameter and height) shorted by a proximity effect bridge.

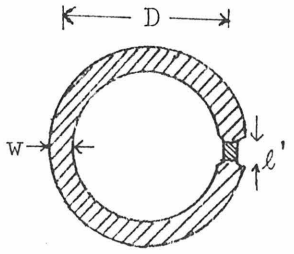

Fig. 2.1c Top view of superconducting quantum interferometer on a flat substrate with diameter of the ring D ~ 0.1-3 mm and width of the ring w ~ 10-50μ typically.

in this way. However, by using this technique it has also been possible to fabricate working interferometers on flat substrates with diameters ranging from 0.1 - 3 mm and widths of the ring 10 - 50μ (Fig. 2.1c). Structures finer than ~ 0.3μ can be obtained by exposure of photoresist in an electron microscope. Ion and plasma etchings have also been used successfully in the removal of the metal films.

The range of the transition temperature of the weak region T_c' is 1.3 - 4.2°K and normal resistance of the junction R is between 10^{-2} - 10Ω. These structures are electrically reliable and mechanically stable. Repeated thermal cyclings between room temperature and 4°K over a period of two years have not changed the characteristics.

2.3 Electrical Characteristics of Proximity Effect Bridges

2.3.1 General Characteristics

When the kinetic energy due to the motion of the supercurrent is equal to the condensation energy, the order parameter is driven to zero and the supercurrent decays spontaneously. According to the G-L theory in a superconductor this velocity limited critical current is proportional to $(T_c - T)^{3/2}$ for T near T_c. However, the critical current of the proximity effect bridge is determined by the maximum overlap of the induced order parameter at the center of the bridge. The critical current of the bridge is smaller than that of the main film and hence is the limiting critical current in such S/N/S structures. For S/N/S structures the predicted[33] temperature dependence is exponential in $(T_c' - T)$. Experimentally the critical current can be made to range

between these two predictions by proper choice of the length. For very short bridges the predicted exponential temperature dependence can always be achieved.

When the critical current of the bridge is exceeded, there is an initial rapid rise in voltage with increasing current. But at high current the dynamic resistance dV/dI approaches the thermodynamically normal resistance R. In this voltage sustaining superconducting state, the dc I-V characteristic exhibits an "excess current" (Fig. 2.2, trace a) and the current induced by a given voltage is always greater than that of the normal state I indicating an extra dissipation from the superconducting state (Trace c in Fig. 2.2). The super current in this type of the bridge follows the empirical relation[34]

$$I_s = (I_c/2)(1 + \cos \frac{2e}{\hbar} \int V \, dt) \quad . \quad (2\text{-}1)$$

This type of non-equilibrium superconductivity with dissipation will be discussed later and compared with the non-dissipating Josephson effect.

2.3.2 The dc and ac Josephson-like Effects

The critical current of the proximity effect bridge can be modulated by an applied magnetic field normal to the film. The Meissner effect in the strong superconducting region tends to concentrate the applied field on the weak region where the bridge is located. Fluxoid quantization (Eq. 1-9) in the bridge area results in the modulation of the critical current by magnetic field with periodicity of a flux quantum if the large demagnetization effect is taken into account.[5] The dc Josephson interference effect from two such bridges in parallel has also been

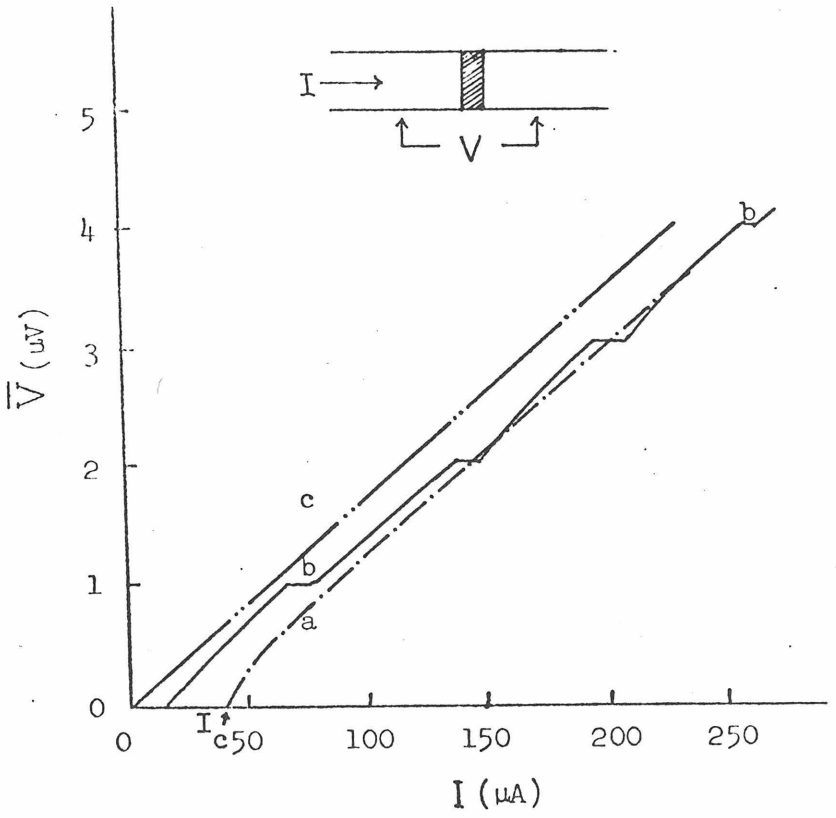

Fig. 2.2 Current-voltage I-$\bar{V}$, characteristics for zero magnetic field. Curve c is for $T > T_c'$, the bridge is in the normal state. Curve a is for $T < T_c'$ with no external radiation; curve b shows the effect of external radiation at about 0.5 GHz. For the case of curve a, the potential developed across the bridge is always less than the normal state potential V_n and at a current $I \gg I_c$ tends to be less than V_n by $RI_c^n/2$.

observed.[35]

When a proximity effect bridge is irradiated with an EM wave of frequency ν, current steps appear at voltages corresponding to the Josephson frequency as given by the relationship $m2eV = nh\nu$ (m,n integers). Figure 2.2 shows the effect of $\sim$0.5 GHz radiation on the I-V characteristics of a 0.65μ x 19μ Nb/Ta bridge. Not shown in the figure is the rich subharmonic structure which is prominently shown in a dV/dI vs I curve. The size of the n^{th} oscillating current step is proportional to $J_n(2eV_{rf}/h)$ when the radiation frequency is equal to the Josephson frequency set by the dc bias voltage.[36,37] Direct observation of Josephson ac effect has also been made when the bridge is dc voltage biased.[38]

2.4 Superconducting Quantum Interferometer

2.4.1 Josephson Junction and Josephson Junction Interferometer

A superconducting quantum interferometer consists of a multiply connected superconductor (e.g. in the form of a superconducting ring) interrupted by a weak link. We wish to investigate some of the equilibrium and non-equilibrium superconducting processes by using a superconducting quantum interferometer with a proximity effect bridge as the weak link. Whereas a singly connected geometry allows the use of a battery as a voltage source; in the case of a single junction interferometer the voltage in the bridge is induced by a time-dependent magnetic flux through the interferometer ring. Unlike the singly connected structure used in earlier investigations, the boundary condition for the wavefunction in a superconducting interferometer is somewhat simplified

in the sense that the wavefunction is required to be continuous at points far away from the bridge inside the superconducting ring.

Before we consider the properties of an interferometer with a dissipating proximity effect bridge (2.3.1), we first review the behavior of a Josephson junction, and briefly examine the responses of an interferometer with Josephson junction as the weak link, and a normal conducting ring in an external time-varying magnetic flux.

For two superconductors separated by a sufficiently thin insulating layer, a dc supercurrent dependent on the phase difference across the junction $\Delta\tilde{\phi}$ can develop even in the absence of a pair electrochemical potential difference $\Delta\bar{\mu}_p = \Delta\mu_p + qV$ across the junction where $\Delta\mu_p$ is the pair chemical potential difference, and V the electrostatic potential difference. This dc Josephson effect is sometimes described as the tunneling of Cooper pairs across the junction. In the ac Josephson effect a non-zero pair potential difference $\Delta\bar{\mu}_p$ across the junction implies Cooper pairs on different sides of the junction have energies differing by $\Delta E = -2\Delta\bar{\mu}_p$ and gives rise to an oscillating current at a frequency ν which depends on $\Delta\bar{\mu}_p$ (Eq. 1-14) i.e.

$$\Delta E = -2\Delta\bar{\mu}_p = h\nu \quad . \qquad (2\text{-}2)$$

The tunneling of a Cooper pair in the presence of a potential difference across the junction is a quantum transition between states of different energies with $\Delta E = -2\Delta\bar{\mu}_p$ while ν corresponds to the "frequency of transition".

Since superconductivity is a coherent macroscopic quantum state in

which the gauge-invariant phases $\tilde{\phi}$ of the wavefunctions of Cooper pairs all coincide, a single wavefunction (1-17)

$$\Psi = \sqrt{\rho_s}\, e^{i\tilde{\phi}} \quad , \qquad (2\text{-}3)$$

can represent the collective behavior of the condensate. In terms of the gauge-invariant electrochemical potential difference of the pair across the barrier $\Delta\tilde{\mu}_p$, the fundamental Josephson equation (2-2) is in general given by (1-19) or

$$\Delta\dot{\tilde{\phi}} = \omega = -2\Delta\tilde{\mu}_p/\hbar \quad , \qquad (2\text{-}4)$$

where $\Delta\tilde{\mu}_p$ is defined in terms of the electrochemical potential $\bar{\mu}_p$ of the pairs and the magnetic vector potential $\vec{A}$ as

$$2\Delta\tilde{\mu}_p = 2(\bar{\mu}_{p2} - \bar{\mu}_{p1}) + 2q\int_1^2 \dot{\vec{A}} \cdot d\vec{r} \qquad (1\text{-}20) \ .$$

Similarly the gauge-invariant electrochemical potential difference of the quasiparticles $\Delta\tilde{\mu}_e$ can be defined in terms of the electrochemical potential difference $\Delta\bar{\mu}_e = \Delta\mu_e + qV$ where $\Delta\mu_e$ is the quasiparticle chemical potential difference and V the electrostatic potential difference.

$$\Delta\tilde{\mu}_e = \Delta\mu_e + qV + q\int_1^2 \dot{\vec{A}} \cdot d\vec{r} = \Delta\bar{\mu}_e + q\int_1^2 \dot{\vec{A}} \cdot d\vec{r}$$

$$= \Delta\mu_e - q\int \vec{E} \cdot d\vec{r} \equiv qU(t) \quad . \qquad (2\text{-}5)$$

In the absence of a magnetic field the otherwise time-dependent potential difference U(t) as defined in (2-5) is just the usual voltage $(\Delta\bar{\mu}_e/q)$ as read on a (non-electrostatic) voltmeter. At thermodynamic equilibrium

the pair and quasiparticle potentials are equal, $\tilde{\mu}_p = \tilde{\mu}_e$, and in the absence of a magnetic field Eq. (2-2) or (2-4) reduces to the usual Josephson frequency-voltage relationship

$$\hbar\dot{\Delta\tilde{\phi}} = \hbar\omega = -2\Delta\tilde{\mu}_e \qquad . \qquad (2\text{-}6)$$

In the limit of weak coupling Josephson's model for the supercurrent density in a superconducting tunneling junction depends on the quantum phase difference $\Delta\tilde{\phi}$ across the junction

$$j_J = j_o \sin \Delta\tilde{\phi} \qquad (1\text{-}16) \quad ,$$

where $\Delta\tilde{\phi}$ is given by (1-18) or the time integral of (2-4). Thus at thermodynamic equilibrium ($\tilde{\mu}_p = \tilde{\mu}_e$), we obtain

$$j_J = j_o \sin \frac{2q}{\hbar}\left(\int U\, dt + \Phi_{dc}\right) \qquad , \qquad (2\text{-}7)$$

where Φ_{dc} is the dc magnetic flux due to a magnetic field applied in the plane of the junction. In a Josephson junction the basic time dependence comes from the quantum phase difference and it is commonly assumed that the amplitude of the supercurrent $\sim \rho_s$ is time-independent and the phase gradient in the oxide barrier is zero. A zero voltage current (U = 0 in Eq. 2-7) arises from the non-dissipative tunneling of Cooper pairs from one superconductor to the other across the junction.

For a Josephson junction in a superconducting ring in the absence of $\Delta\bar{\mu}_p$, the phase difference $(\phi_2 - \phi_1)$ in $\Delta\tilde{\phi}$ defined by

$$\Delta\tilde{\phi} = \phi_2 - \phi_1 - \frac{2q}{\hbar}\int_{1\ \text{junction}}^{2} \vec{A} \cdot d\vec{r} \qquad (1\text{-}18) \quad ,$$

can be obtained by spatial integration of $\nabla\phi$ in the superconducting ring, where $\nabla\phi$ is given by (1-4). In the limit of thick superconducting ring as discussed in (1.3) the phase difference can be approximated by

$$\phi_2 - \phi_1 = \int_{1}^{2}_{\text{ring}} \nabla\phi \cdot d\vec{r} \cong \frac{2q}{\hbar} \int_{1}^{2}_{\text{ring}} \vec{A} \cdot d\vec{r} \quad . \qquad (2\text{-}8)$$

Hence combining Eqs. (1-18) and (2-8) the supercurrent in a Josephson interferometer operating under the above assumptions reponds to the external flux $\Phi_x(t)$ like

$$j_J = j_o \sin \frac{2q}{\hbar} \oint \vec{A} \cdot d\vec{r} = j_o \sin \left(2\pi\Phi_x(t)/\Phi_o\right) \quad . \qquad (2\text{-}9)$$

In particular, the supercurrent varies periodically with an applied magnetic flux enclosed by the interferometer ring with period Φ_o.

Many models of Josephson tunneling junctions and Josephson interferometers have been proposed[39-40] which in their proper limits seem to describe these non-dissipating structures reasonably well. However, we are interested in the "transition energy" ΔE (or the equivalent quantum mechanical transition frequency, $\nu = \Delta E/h$) involved in the dynamics of the dissipating superconducting state as exemplified by proximity effect bridges which also exhibit Josephson-like behavior (2.3). The dynamics of the dissipation and the rate of quantum response will be characterized in terms of physical parameters like the normal resistance and the critical current of the bridge, the inductance of the interferometer ring, amplitude and frequency of external magnetic flux at rf and near dc levels.

2.4.2 Normal Conducting Ring

For a normal conducting ring with self-inductance L and resistance R in an external time-varying flux $\Phi_x(t)$, the energy loss per electron qV = qIR is balanced by the energy supplied from the external power source which can be treated as a voltage source $\dot{\Phi}_x(t)$ less the back emf $L\dot{I}$ of the ring circuit:

$$\Delta E = q(\dot{\Phi}_x(t) - L\dot{I}) = qIR \quad , \qquad (2\text{-}10)$$

where I is the induced current in the ring. The corresponding quantum transition frequency ν can be defined as

$$\nu = \Delta E/h \quad . \qquad (2\text{-}11)$$

For a harmonic drive flux $\Phi_x(t) \sim e^{i\omega t}$, in a harmonic approximation the current also varies like $e^{i\omega t}$ and from (2-10) the induced current I is given by

$$I = \frac{i\omega\Phi_x}{R + i\omega L} \quad . \qquad (2\text{-}12)$$

In the resistive limit ($R \gg \omega L$) the drive flux and the induced current are $\sim\pi/2$ out of phase due to the fact that in a resistor the current and voltage are in phase and the induced voltage is $\pi/2$ out of phase with the drive flux. For $\omega L \gg R$, the current and the drive flux are in phase because the induced voltage leads both the current in an inductor and the drive flux by $\pi/2$. Substituting (2-10), (2-12), into (2-11) the "transition frequency" in the harmonic approximation becomes

$$\nu = i\omega \frac{q}{h} \frac{R}{Z} \Phi_x(t) \quad , \qquad (2\text{-}13)$$

where the impedance $Z = R + i\omega L$. Since the drive flux $\Phi_x(t)$ is a function of time, the frequency response ν is not constant in time, but will be dominated by frequency modulation effect. In the inductive limit of $\omega L \gg R$, the transition rate is essentially determined by the L/R time constant; whereas in the resistive limit of $R \gg \omega L$, the imaginary ν is indicative of the dissipation in such circuit.

Implicit in the above circuit analysis is the assumption that lumped constants like L and R can adequately represent the circuit parameters at the operating frequency ω. In this sense, the above analysis for a normal conductor ring also applies to a superconducting ring of same inductance L with part of the ring made of a normal metal with resistance R.

2.4.3 Interferometer with a Proximity Effect Bridge

Based on the two fluid model (1.1) an equivalent circuit for a proximity effect bridge consists of a junction element denoted by J in parallel with a resistor R (Fig. 2.3a). Below the critical current of the bridge, the current across the bridge is solely carried by superconducting electrons through the junction J referred to as I_J and the current through the resistor I_R is zero. When the total current I exceeds the critical current of the bridge, while the supercurrent I_s still flows through the junction element J, the amount of current in excess of the supercurrent is carried by the quasiparticles through the resistor R (with resistance R equal to the normal resistance of the bridge for T near T_c') i.e. the normal current, $I_n = I - I_s = I_R$.

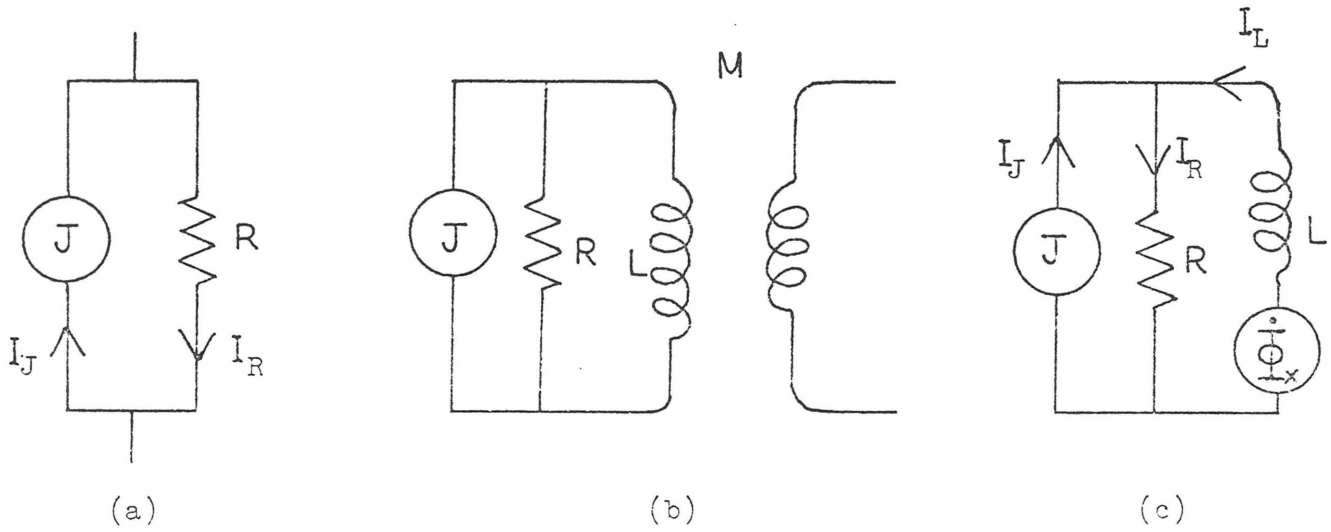

Fig. 2.3 Schematic representations of equivalent circuits for a proximity effect bridge (a), and an interferometer with such a bridge as the weakly superconducting region inductively coupled (M) to a power source (b) as discussed in the text (2.4.3). In (c) the power source is approximated as a voltage source ($\dot{\Phi}_x$) in the interferometer circuit.

We assume that the equivalent circuit for a superconducting interferometer with a proximity effect bridge as the weak link is a superconducting inductor L in parallel with a bridge (Fig. 2.3b). In the inductor L, which excludes the bridge region, as long as the critical current of the strongly superconducting part of the ring is not exceeded, the current in the inductor I_L is carried solely by the superconducting electrons.

Since I_J is not a source of power, in order to study the dynamic properties of the interferometer a power source is introduced by applying an rf flux $\Phi_x(t)$ through the superconducting ring. Experimentally, this was accomplished by inductive coupling of the interferometer to an rf circuit. In the circuit analysis this rf power source is approximated as a voltage source $\dot{\Phi}_x(t)$ in the interferometer circuit (Fig. 2.3c). The exact functional form of the supercurrent in the bridge depends on the model for the bridge and will be considered later. However, from the experimental fact that these bridges show Josephson-like phenomena we would expect that the supercurrent in the bridge I_J would have sinusoidal dependence on the gauge-invariant quantum phase difference across the bridge $\Delta\tilde{\phi}$ similar to a Josephson junction (1-16). In fact it will be shown that the functional dependence of I_J on $\Delta\tilde{\phi}$ need not be sinusoidal (sine or cosine), any reasonably smooth oscillating function which passes through zero twice per period will lead to essentially the same qualitative conclusions. The response of this inductively coupled circuit to the quantum phase dependent supercurrent I_J is to be analyzed here based on certain assumptions, with the introduction of explicit functional form of

I_J postponed till a later section.

In order to be able to write a circuit equation for an interferometer inductively coupled to an rf power source, the following assumptions will be made: It is assumed that (1) we can treat the supercurrent in the bridge I_J as a current (but not power) source which depends on the quantum phase difference $\Delta\tilde{\phi}$ across the bridge; (2) the quantum effect due to I_J is a small perturbation on the classical effect due to external rf flux Φ_x; (3) the shielding effect due to LI_J is small relative to the classical flux so that essentially all the contribution to the flux comes from the external rf flux Φ_x; (4) there is little or no feedback effect from I_J to the classically induced current due to Φ_x so that we can to first order write current and voltage response of the circuit as a linear combination of the classical and quantum effects.

Applying Kirchkoff's law to the equivalent circuit (Fig. 2.3c) under the stated assumptions leads to

$$I_L + I_J = I_R \quad , \qquad (2\text{-}14)$$

$$\Phi_{total} = \Phi_x - LI_L \quad , \qquad (2\text{-}15)$$

$$\dot{\Phi}_{total} = \dot{\Phi}_x - L\dot{I}_L = I_R R \quad . \qquad (2\text{-}16)$$

Since it is assumed that the quantum effect is small compared to the classical response ($I_J \ll I_L$), it would be presumed that a harmonic drive $\Phi_x(t)$ would give rise to quasi-harmonic response with the current passing through zero twice per cycle. Instead of solving for a complete analytic solution, we assume that a continuous solution to Eqs. (2-14) -

(2-16) exists for a harmonic drive flux if the supercurrent due to quantum effect I_J is sufficiently small relative to the contribution to I_L from classical response due to $\dot{\Phi}_x$. Substituting I_R from (2-14) into (2-16) we get

$$I_L = \dot{\Phi}_x/Z - RI_J/Z \quad , \qquad (2\text{-}17)$$

where $Z = R + i\omega L$. In the limit that the quantum effect is negligible in comparison with the classical behavior of the circuit (i.e. $RI_J/Z \ll \dot{\Phi}_x/Z$) Eq. (2-17) reduces to (2-12) and the discussion following (2-12) regarding the phase relationship between the current I_L and the drive flux Φ_x is also applicable here. The variation of I_L from its classical response $\dot{\Phi}_x/Z$, i.e.

$$\delta I_L \equiv RI_J/Z \quad , \qquad (2\text{-}18)$$

due to quantum response and its effects will be our main concern here. The assessment of this quantum response depends on the functional form and thus the model of I_J, which we will develop in the next section.

2.4.4 Quantum Transitions and Superconducting Dissipations

One experimental fact which occurs in common at the S/W interface and in a proximity effect bridge (S/W/S) is that the dissipation potential in these structures (energy loss per electron) is less than the normal state IR at a given current (Fig. 2.2). In order to explain this fact observed in weak superconductors a phase slip model has been advanced to account for the behavior of supercurrents in an electric field.[41] The electric field across a weak superconductor may be in the form of an

electrochemical potential across the bridge as in earlier investigations or of time-varying magnetic potential in the configuration of interferometers.

Basically the "phase slip" model describes a local process in a superconductor in which the supercurrent at a local weak region is accelerated to its critical value, followed by a local collapse of superconductivity and a discontinuous (and undefined) "transition" to a new superconducting state whose relative phase with respect to the original state has shifted by 2π. For thin films, the maximum supercurrent density j_c occurs at the critical velocity $v_c = v_m/3^{\frac{1}{2}}$ where v_m is the maximum electron drift velocity.[42] At low velocity, the supercurrent accelerates according to Eq. (1-4) but can be cast as follows to show explicitly the dependence on the electric field E and the gauge-invariant phase gradient $\nabla\tilde{\phi}$

$$\frac{\partial j_s}{\partial t} = 2n_s q^2(E - \nabla\mu_p/q)/m = n_s q\hbar(\nabla\dot{\tilde{\phi}})/m \quad . \qquad (2\text{-}19)$$

When the critical velocity v_c is exceeded, the supercurrent density becomes unstable and spontaneously decays to zero on a time scale probably comparable to the pairing time $\tau \sim \frac{h}{\Delta} \sim 10^{-12}$ sec.

However, in weakly coupled superconductors the sudden destruction of superconductivity occurs within the weak link and extends roughly over the coherence length ξ. From Eq. (2-19) it is evident that a transition to a lower current state to re-establish phase coherence can be made by decreasing the quantum phase difference $\Delta\tilde{\phi}$ across the weak link by 2π. The new state which appears after the phase slip process

then accelerates to its critical velocity and decays again.[42] The process repeats itself at a rate as given by the Josephson oscillation frequency ν (Eq. 2-2 or 2-4) with a power loss for the entire circuit $\bar{I}_s U = (\bar{I}_s \Phi_o)\nu$ or a superconducting dissipation of $\bar{I}_s \Phi_o$ per cycle where $\bar{I}_s$ is the time average supercurrent existing before and after the phase slip and U is the dissipation voltage defined in (2-5).

On a two fluid model, normal current I_n can also flow in the weak link and when such a circuit is current biased to a current I, the normal current is $I_n = I - I_s$ with the normal dissipation $I_n R$ where R is the normal resistance of the weak link. Rieger et al[43] have shown analytically that the oscillating supercurrent predicted by time-dependent G-L theory across a weak link in the voltage sustaining state is consistent with Eq. (2-1) as observed experimentally. In that analysis it is assumed that the relaxation time or the time during which phase slip occurs is short in comparison with the time of acceleration to v_c so that during a large fraction of an oscillation period the approximation of equal potentials of the pairs and quasiparticles ($\tilde{\mu}_p = \tilde{\mu}_e$) is a valid one. Thus the result of this analysis for I_s ($I > I_c$) in general is a periodic function of the gauge-invariant phase difference $\Delta\tilde{\phi}$ similar to a Josephson junction below its critical current (1-16)

$$I_s = \frac{I_c(B,T)}{2}\left[1 + \cos \Delta\tilde{\phi}\right] \quad . \qquad (2\text{-}20)$$

In most experiments, the bridges are almost always current biased due to the low resistance of the bridge. Their [43] analysis also predicts that as the time-averaged potential across the bridge $\bar{U}$ goes to zero,

the time averaged supercurrent $\bar{I}_s$ approaches I_c, and at $\bar{U} \gg RI_c$, the oscillation is nearly harmonic with $\bar{I}_s \cong I_c/2$. The asymmetry of the supercurrent with respect to zero implies that for a given total current I the potential U developed by dissipation in these proximity effect bridges can be approximated by

$$U = RI_n = R(I-I_s) \equiv RI - v_s(t) \quad , \qquad (2\text{-}21)$$

$$U = RI - \frac{1}{2} RI_c(B,T)[1 + \cos \Delta\tilde{\phi}] \quad . \qquad (2\text{-}22)$$

Not explicitly expressed in (2-21) or (2-22) is the fact that inside the (non-equilibrium) bridge to conserve current, $I \equiv I_s + I_n \equiv I_s + U/R$, I_s and I_n are π out of phase in a harmonic approximation for current. Outside the bridge region the normal current in a conductor is in phase with the potential U, whereas the supercurrent is inductive ($\dot{j}_s \sim -\nabla U \sim E$) and is $\pi/2$ out of phase with the potential U. Outside the bridge region, for current density below the critical value the current is carried by the superconducting electrons. Inside the bridge for current I greater than the critical current of the bridge, the excess current $I - I_s = I_n$ develops a dissipating potential according to the Ohm's Law, $U = I_n R$.

Often it is convenient to think of the two currents I_s and I_n in terms of voltages: a dissipating voltage U and a non-ohmic voltage $v_s(t)$ source associated with the supercurrent as defined in Eq. (2-21). The above analytic result is consistent with experimental observations[30] on the amplitude and frequency spectrum of the potential developed across a large number of proximity effect bridges of various dimensions,

material combinations, critical currents and resistances.

2.4.5 Circuit Analysis

Most of the early analysis[44,45] of the single junction quantum interferometer was based on the equilibrium characteristics of the magnetic flux enclosed by the superconducting inductor. The equilibrium magnetic flux enclosed by the interferometer ring varies periodically with the applied flux with period Φ_o. Based on electrodynamics discussed in this chapter, through the potential $\Delta\tilde{\mu}_p$, it is possible to determine the dynamics of the dissipation and the rate of quantum response in terms of known physical parameters.

Physically, as the flux changes in the ring, the supercurrent makes the quantum transition from the intial quantized state of current $I_i = n\Phi_o/L$ to the adjacent final quantized state $I_f = (n-1)\Phi_o/L$ where n is an integer. The difference in energy between these two quantized flux states is

$$\Delta E = (n\Phi_o)^2/(2L) - (n-1)^2\Phi_o^2/(2L) \quad , \qquad (2\text{-}23)$$

which can be expressed in terms of I_i and I_f as

$$\Delta E = (I_i + I_f)\Phi_o/2 \equiv \bar{I}_s\Phi_o \quad , \qquad (2\text{-}24)$$

as discussed in (2.4.4). In the following non-equilibrium description of the superconducting interferometer the flux is not necessarily quantized, but the rate of change of the relative quantum phase across the bridge is set by the difference in the gauge-invariant electrochemical potential across the bridge, $2\Delta\tilde{\mu}_p$ (Eq. 2-4).

To analyze the circuit of (2.4.3) or Fig. (2.3.c) we can substitute an explicit form for the junction current I_j in (2-18) by I_s as given in (2-20). Making use of the relation (2-4) $\Delta\tilde{\phi} = -\int 2\hbar^{-1}\Delta\tilde{\mu}_p dt$, the thermodynamic equilibrium assumption $\Delta\tilde{\mu}_p = \Delta\tilde{\mu}_e$, and the definition for $U = \Delta\tilde{\mu}_e/q$ (2-5), the supercurrent across the bridge (2-20) can be written as

$$I_s = \frac{I_c}{2}\left[1 + \cos\left(\int U'(t)dt + \Phi'_{dc}\right)\right] \quad , \qquad (2\text{-}25)$$

where Φ_{dc} is the static magnetic flux enclosed by the ring, and the primed quantity X' is related to the unprimed quantity X by a normalizing factor $2\pi/\Phi_o$

$$X' = 2qX/\hbar = 2\pi X/\Phi_o \quad . \qquad (2\text{-}26)$$

The variation in supercurrent caused by the quantum phase difference $\Delta\tilde{\phi}$ in (2-17) or (2-18) is separated out as δI_s

$$\delta I_s \cong (v_s/Z)\cos\left(\int U'dt + \Phi'_{dc}\right) \quad , \qquad (2\text{-}27)$$

where v_s is defined as $v_s = RI_c/2$.

It is instructive and convenient to use an equivalent voltage model (Fig. 2.4a) for the bridge instead of the current model in Fig. (2.3c) to do the circuit analysis and to show that this approach will also lead to (2-27). Making the same assumptions as in (2.4.3), but stated in terms of v_s: it is assumed that (1) we can treat the supercurrent as a voltage source $v_s(t) = RI_s$ as defined in (2-21) or (2-22); (2) the quantum effect v_s is small compared to classical effect

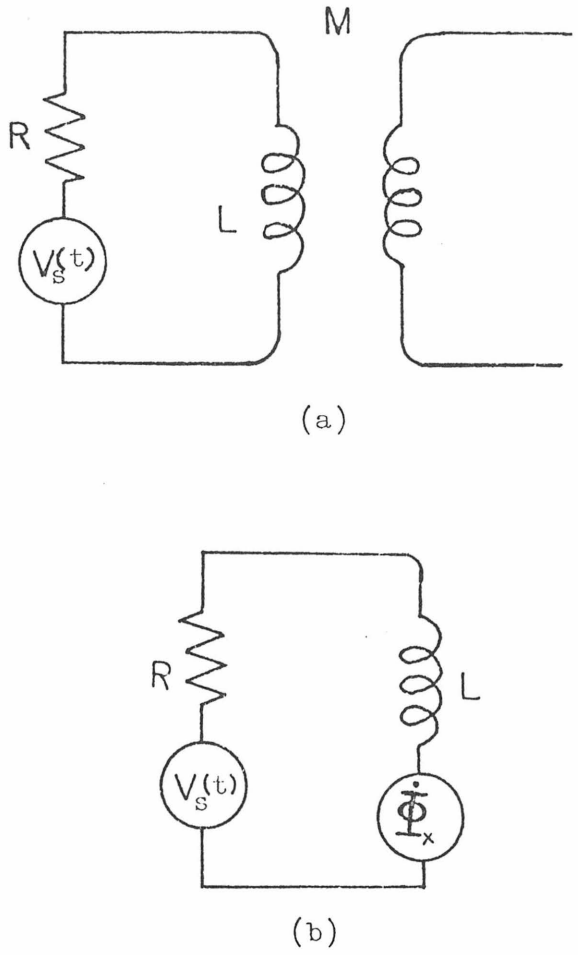

Fig. 2.4 Schematic representation of the interferometer circuit. The equivalent circuit for the bridge is a resistor (R) in series with a voltage source $v_s(t)$. The interferometer (inductance L) is inductively (M) coupled to an rf power source, as discussed in (2.4.4), which is approximated as a voltage source $(\dot{\Phi}_x)$ in the interferometer circuit.

of $\dot{\Phi}_x(t)$; (3) the shielding effect $L\delta I_s$ due to v_s is small compared to the classical flux so that essentially all the contribution to the flux comes from the external rf flux Φ_x. This condition of small screening flux $L\delta I_s$ will be shown to be equivalent to the requirement of $v_s < \omega\Phi_0$; (4) there is little or no feedback effect from v_s to $U \propto \dot{\Phi}_x$ so that we can treat both voltage sources separately and the circuit responds to a linear combination of the two voltage sources. From Eq. (2-21), the equivalent model for the proximity effect bridge is a voltage (but not power) source v_s in series with a resistor of resistance R (Fig. 2.4a).

Upon applying Kirchhoff's law to the equivalent circuit of an interferometer (Fig. 2.4b) we obtain

$$U(t) = \dot{\Phi}_x(t) - L\dot{I} = RI - v_s(t) \quad , \qquad (2\text{-}28)$$

where

$$v_s(t) = v_s \left[1 + \cos\left(\int U'dt + \Phi'_{dc}\right)\right] \quad . \qquad (2\text{-}29)$$

Again assuming a harmonic drive flux and the existence of a continuous solution to (2-28), the current I can be written as

$$I = i\omega\Phi_x/Z + v_s(t)/Z \quad , \qquad (2\text{-}30)$$

which is just (2-17) with I_J given by (2-25). The first term is the classical response to external drive flux and the second term arises from the quantum effect v_s with δI_s given by (2-27). If quantum effects are small then the current I can be approximated classically in terms of the voltage $i\omega\Phi_x$ and impedance Z as is evident from Eq. (2-30): for

$v_s \ll \dot{\Phi}_x$, $I \cong \dot{\Phi}_x/Z$ and $U \cong IR \cong (R/Z)\dot{\Phi}_x$. Since U is a function of time, inserting this U into $v_s(t)$ as given by (2-29) leads to a $\delta I_s = v_s(t)/Z$ whose behavior is essentially frequency-modulated. For a harmonic drive flux $\Phi_x(t) = \Phi_x \sin \omega t$, by expanding $\cos\left[\left(R/Z\right)\Phi'_x \sin \omega t + \Phi'_{dc}\right]$ in Bessel functions and keeping the lowest order terms, δI_s in this limit becomes

$$\delta I_s = \frac{v_s}{Z}\left\{J_o\left(R\Phi'_x/Z\right)\cos \Phi'_{dc} + 2J_1\left(R\Phi'_x/Z\right)\sin \omega t \sin \Phi'_{dc}\right\} . \tag{2-31}$$

The contribution to δI_s at the drive frequency ω is

$$\delta I_s = \frac{2v_s}{Z} J_1\left(R\Phi'_x/Z\right)\sin \Phi'_{dc} \sin \omega t \quad . \tag{2-32}$$

Equation (2-32) suggests that for $R \gg \omega L$ or $Z \cong R$ the supercurrent δI_s is in phase with the drive flux. In this resistive limit the effect of v_s is mainly dissipative with an associated energy loss per electron of $R\delta I_s$ and is predominately an effective parametric resistance. For $\omega L \gg R$ or $Z \cong i\omega L$, expanding $\cos\left[\left(R/i\omega L\right)\Phi'_x \sin \omega t + \Phi'_{dc}\right]$ leads to

$$\delta I_s = \frac{v_s}{i\omega L}\left\{J_o\left(\frac{R\Phi'_x}{\omega L}\right)\cos \Phi'_{dc} + 2J_1\left(\frac{R\Phi'_x}{\omega L}\right)\sin \omega t \sin \Phi'_{dc}\right\} , \tag{2-31a}$$

and δI_s at the frequency ω:

$$\delta I_s = \frac{2v_s}{\omega L} J_1\left(\frac{R\Phi'_x}{\omega L}\right)\sin \Phi'_{dc} \cos \omega t \quad . \tag{2-32a}$$

Thus for $\omega L \gg R$, the impedance Z in the Bessel argument of (2-31) or (2-32) is $Z \simeq \omega L$ and the variation in supercurrent δI_s is $\pi/2$ out of

phase with the drive flux. In this inductive limit, the quantum effect δv_s is essentially a modification of the flux by an amount $L\delta I_s$ and behaves as an effective parametric reactance. In general δI_s has contributions from both terms: $2v_s|Z|^{-1}\{J_0(A)J_1(B)\cos\omega t - J_1(A)J_0(B)\sin\omega t\}\sin\Phi'_{dc}$ where $A-iB = \frac{R}{|Z|}\Phi'_x e^{-i\theta}$ and $\theta = \arctan(\omega L/R)$.

In order to verify the functional dependence of δI_s on the various parameters Φ_x, Φ_{dc}, R, ωL, and T, the superconducting interferometer is inductively coupled to an rf tank circuit. The presence of the superconducting circuit modifies the characteristics of the tank circuit. The induced changes in the impedance of the tank circuit are measured as a function of the above parameters. Since the rf tank is driven from a constant current source this variation in the reflected impedance (from the interferometer to the tank circuit) shows up as a signal voltage. In this sense the rf tank acts as an impedance transformer between the quantum interferometer and the detection system.

The modulation of supercurrent due to v_s is reflected into the rf tank circuit as a variation of tank voltage δV due to the quantum effect v_s

$$\delta V = i\omega M\delta I_s \quad . \qquad (2\text{-}33)$$

For $R \gg \omega L$, δV can be expressed as an equivalent $I\delta R$ and the component at ω

$$\delta R = \frac{2v_s}{I}\left(\frac{\omega M}{R}\right) J_1\left(\Phi'_x\right)\sin\left(\Phi'_{dc}\right) \quad , \qquad (2\text{-}34a)$$

and for $R \ll \omega L$, as an equivalent reactance at frequency ω

$$-\omega\delta L = \frac{2v_s}{I}\left(\frac{M}{L}\right) J_1\left(\frac{R}{\omega L}\Phi'_x\right)\sin\left(\Phi'_{dc}\right) \quad . \qquad (2\text{-}34b)$$

This situation is analogous to the classical coupled circuit with an untuned secondary consisting of a resistance R in series with an inductance L. The coupled impedance Z_c is

$$Z_c = \frac{R}{R^2 + (\omega L)^2} (\omega M)^2 - i \frac{\omega L}{R^2 + (\omega L)^2} (\omega M)^2 \quad . \qquad (2\text{-}35)$$

Examination of (2-35) shows that the coupled impedance introduced into the primary circuit by this R-L secondary consists of a resistance in series with a capacitive reactance. In the resistive limit of $R \gg \omega L$, the coupled impedance becomes

$$Z_c \sim R^{-1}(\omega M)^2 \quad , \qquad (2\text{-}36a)$$

and the effect of the coupled resistance is to increase the effective resistance in the primary circuit. For $\omega L \gg R$,

$$Z_c \sim -i(\omega L)^{-1}(\omega M)^2 \quad . \qquad (2\text{-}36b)$$

The effect of an inductive secondary produces a capacitive coupled reactance between the terminals of the primary coil and neutralizes a portion of the primary inductance.

Therefore, for $R \gg \omega L$, the main effect caused by the quantum voltage v_s is a change in Q of the rf tank and will be referred to as an amplitude modulation (AM). For $\omega L \gg R$ the main effect is a shift of frequency of the tank circuit which we define as frequency modulation (FM).

The small I_s approximation (leading to Eq. 2-32) remains valid as long as $v_s(t)$ is small compared to the classical contribution to the

potential U(t). Since $v_s(t)$ increases with decreasing temperature, at sufficiently low temperature the potential U may be significantly modified by the quantum effect. From Eq. (2-28) the variation of U due to quantum effect can be estimated to be the term $L\delta I_s$ in

$$U = \dot{\Phi}_x - L\dot{I} \cong \dot{\Phi}_x + j\omega L I_n + j\omega L \delta I_s \quad .$$

Here it is assumed that the induced current in the strongly superconducting part of the ring does not exceed the critical current of the ring outside the weak link and therefore the current is carried by the supercurrent δI_s (i.e. $I_n = 0$ in the superconducting ring excluding the bridge region). The quantum voltage across the bridge is $\sim\omega\Phi_o$ produced by passing one Φ_o at a time at the rate ω. The requirement that the shielding effect $\omega L\delta I_s$ (produced by δI_s around the inductor L at the frequency ω) be small relative to $\omega\Phi_o$ is equivalent to a statement that a variation in the instantaneous frequency of $\delta\Omega \sim \omega L\delta I_s/\Phi_o$ be small compared to $\omega \sim U/\Phi_o$. Therefore one of the conditions that Eq. (2-32) be valid is $L\delta I_s/\Phi_o < 1$. A more general condition comes from Eq. (2-32) by noting the maximum $J_1(z)$ is of the order ~ 0.5 and thus $\delta I_s \sim |v_s/Z|$ so that the above requirement on frequency becomes

$$v_s < \Phi_o \left|\frac{Z}{L}\right| = \Phi_o \omega \left| 1 + \frac{R}{i\omega L} \right| \quad ,$$

or

$$I_c < \omega\Phi_o \left| \frac{1}{R} + \frac{1}{i\omega L} \right| \quad . \qquad (2\text{-}37)$$

For I_c greater than this value, the result given by (2-32) may no longer be valid.

This condition on I_c in Eq. (2-37) can be understood by considering the equivalent circuit as given by Fig. 2.3. In order to keep the self-modulation effect of the bridge element J small, the critical current of the junction I_c should be small compared to the current given by the quantum voltage across the bridge, $\omega\Phi_o$ divided by the effective impedance of the circuit Z_e determined by the parallel combination of normal resistance of the bridge R and inductive impedance $i\omega L$ of the ring $Z_e^{-1} = R^{-1} + (i\omega L)^{-1}$; i.e. the supercurrent must be small with respect to the normal current, $I_c < \omega\Phi_o/Z_e$. Thus if $R \gg \omega L$ the bridge is nearly voltage biased and the region of validity of (2-32) is that the critical current of the bridge I_c be less than the shielding current induced by a flux quantum in the inductor, $I_c < \Phi_o/L$. And when $\omega L \gg R$ the bridge is nearly current biased, and the limit on the voltage across the bridge is $RI_c < \omega\Phi_o$.

When v_s exceeds the limit set by Eq. (2-37), the (interferometer) circuit can no longer follow the rf drive voltage in the manner described by Eq. (2-32). Instead of a harmonic response, the emf generated by flux transfer across the ring is composed of a series of pulses: As v_s increases above the limit, the voltage U which determines the frequency response of the circuit becomes seriously modulated by the internal frequency $\Omega \sim (\omega L/Z)(v_s/\Phi_o)$ which results in strong feedback from v_s to U. Since at high frequency the reactive impedance dominates over the resistance, the internal frequency approaches $\Omega \sim v_s/\Phi_o$. Hence the resultant voltage is pulse-like with amplitude $v_s \sim \Omega\Phi_o \sim \Phi_o/\tau$ where $\tau \sim \Phi_o/v_s$ is the duration of the pulse separated by time T between the

adjacent pulses. The voltage pulse is the spontaneous dissipation incurred during a quantum transition (phase slip). The effect of the external drive flux Φ_x is to trigger these pulses and provides the energy dissipated away by the voltage pulses at the rate of twice per cycle.

This limit has been analyzed before by Fourier expansion of the pulse train.[46] Assuming that the emf U is a series of square pulses with interval τ and spaced by T sec in time between the pulses and ignore the initial transients, then U is

$$U \sim \sum_n a_n \cos(2\pi nt/T)$$

$$a_n = \frac{1}{T} \int_0^T \frac{\Phi_o}{\tau} \cos(2\pi nt/T)\, dt = \frac{1}{T} \frac{\Phi_o}{\tau} \int_0^\tau \cos(2\pi nt/T)\, dt$$

$$= -\frac{\Phi_o}{2\pi n\tau} \sin(2\pi n\tau/T) \quad .$$

Thus,

$$U \sim \frac{\Phi_o}{2\pi\tau} \sum_n n^{-1} \sin(2\pi n\tau/T) \cos(2\pi nt/T) \quad . \qquad (2\text{-}38)$$

In order to use the flux Φ as the expansion variable, by averaging the emf $\frac{d\Phi}{dt}$ over T we approximate

$$\frac{\Phi}{t} \sim \frac{\Phi_o}{T} \quad , \qquad (2\text{-}39)$$

in (2-38) and get

$$U \sim \frac{\Phi_o}{2\pi\tau} \sum_n n^{-1} \sin(2\pi n\tau/T) \cos(2\pi n\Phi/\Phi_o) \quad . \qquad (2\text{-}40)$$

In the limit of $\tau \ll T$ the emf becomes independent of τ and equals

$$U \sim \frac{\Phi_o}{T} \sum_n \cos\ (2\pi n\Phi/\Phi_o) \quad . \qquad (2\text{-}41)$$

If the applied flux varies like $\Phi = \Phi_x \sin \omega t$, then (2-39) can be approximated by $\Phi_o/T \sim \Phi_x/t \sim \omega\Phi_x$. Taking into account of the existence of an ambient dc flux Φ_{dc} and that the emf in the interferometer ring is reduced from the applied rf flux Φ_x by a factor R/Z (as in 2-31) the signal with a large harmonic content has an amplitude $\delta I_s \sim U/R$ at the drive frequency ω:

$$\delta I_s \sim \frac{\omega\Phi_x}{Z} J_1\left(\frac{R}{Z}\Phi'_x\right) \sin \Phi'_{dc} \quad . \qquad (2\text{-}42)$$

With increasing v_s or I_c, the drive flux Φ'_x becomes increasingly modified by the shielding effect. A first order approximation of this effect is the reduction of Φ_x by a flux Φ_c equivalent to the shielding current I_c (2-37) or a resulting effective flux $(\Phi_x - \Phi_c)$. Thus with this shielding effect taken into account, (2-42) becomes

$$\delta I_s \sim \frac{\omega(\Phi_x - \Phi_c)}{Z} J_1\left[\frac{R}{Z}(\Phi'_x - \Phi'_c)\right] \sin (\Phi'_{dc}) \quad . \qquad (2\text{-}43)$$

Therefore as v_s increases at lower temperature, the signal remains periodic with the dc magnetic flux. However the rf response of the signal does not become periodic with the rf drive flux until a "critical flux" Φ_c is exceeded and the signal increases until it reaches a maximum of about $\omega\Phi_o/Z$ before it decreases.

2.4.6 Experimental Considerations and Measurements

In this section a few experimental considerations and the electronic systems used for investigations of the quantum properties of superconducting interferometers will be briefly considered, and followed by the experimental measurements.

The superconducting interferometer and the rf tank circuit are immersed in a liquid helium dewar within a nitrogen dewar. The temperature of the helium bath can be varied from 4.2° to 1.3°K with a resolution of 1 m°K by controlling its vapor pressure.

Since the measurements were sensitive to variations in the ambient magnetic field and the pickup of undesirable electromagnetic signal in the room, a number of precautionary steps were taken to minimize such external interferences. To reduce the static magnetic field to the milligauss level, a mu-metal shield was placed around the dewars and demagnetized before each run. A superconducting lead shield provided additional shielding from fluctuations of external field. To provide electromagnetic shielding, all measurements were made in an rf-shielded room with its power mains filtered.

The electronic system used for measurements is shown in Fig. 2.5. An rf (at 10 or 30 MHz) current was introduced into the tank circuit at the resonance frequency ω. If in addition there was a low frequency flux Φ_{dc} enclosed by the interferometer, then the resultant emf due to quantum effects in the rf tank at frequency ω was given by Eqs. (2-32) and (2-33)

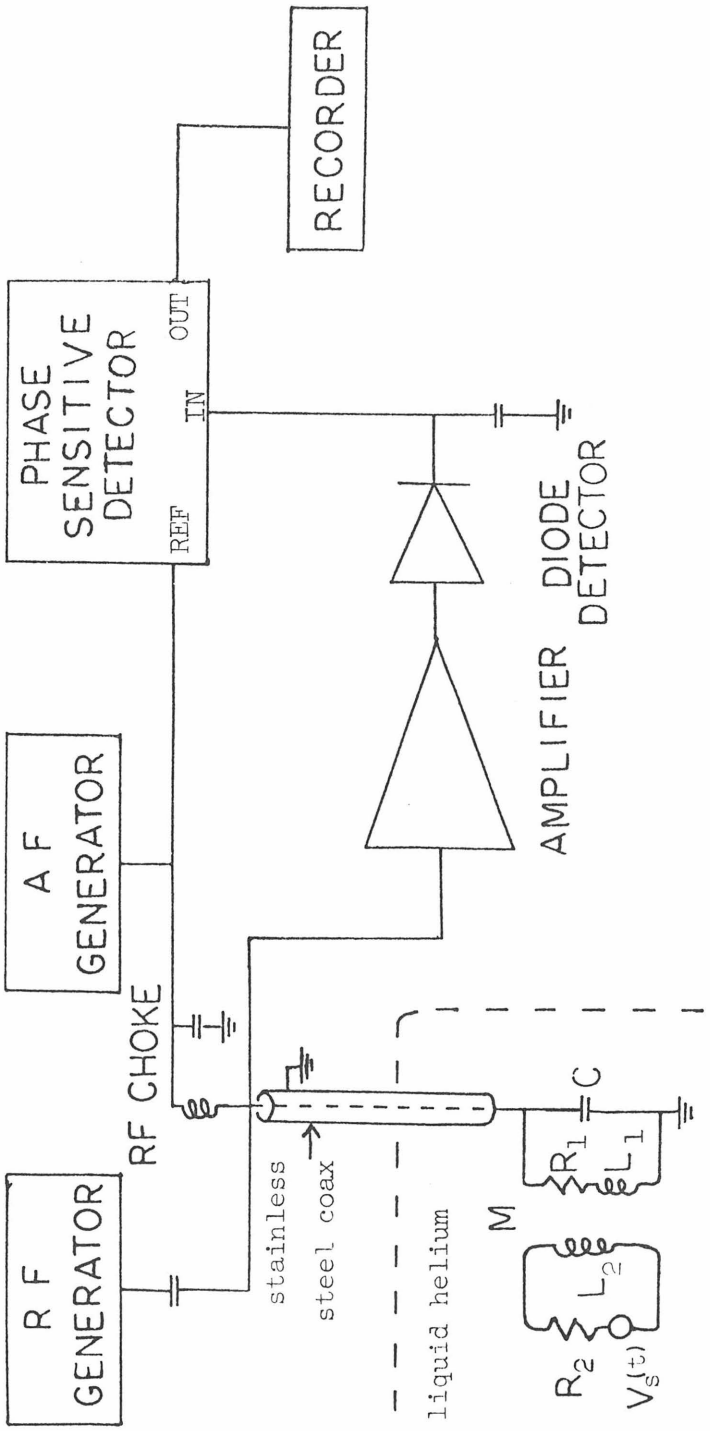

Fig. 2.5 Bloch diagram of the electronics system used for observing quantum properties of superconducting interferometer.

$$\delta V \sim v_s \frac{\omega M}{Z} J_1(R\Phi_x'/Z) \sin \Phi_{dc}' \quad . \qquad (2\text{-}44)$$

This emf was amplified and demodulated to produce a dc voltage which is periodic in Φ_{dc} and $R\Phi_x/Z$. To eliminate the effects of dc drifts in the amplifier instrument, a small audio-frequency (AF) flux ($< \Phi_o/2$) was used to modulate the rf signal. The above dc signal after being converted to the AF signal was phase sensitively detected at the autio-frequency. Thus the classical emf ($V \cong \omega\Phi_x(t)$) response does not appear in the AF phase-detected signal. The magnitude of the quantum voltage $\omega\Phi_o$ is $\sim$0.4 μV at 30 MHz. Hence in this detection technique the AF signal δV (Eq. 2-44) can be taken as the variation of the tank impedance due to the quantum effect $v_s(t)$. The response time of the system was typically $\sim$1 sec. and was set by the requirements on the amplifier noise.

In order to be able to make a quantitative evaluation of this circuit analysis, it was necessary to measure all of the electrical characteristics separately.

The characteristics of the coupled circuit can be determined by driving the circuit with a constant current source. Using simple circuit analysis, the loaded and unloaded (with and without the interferometer coupled to the tank) resonance frequencies of the rf tank f_R and f_o and quality factors Q and Q_o are related as follows

$$\Omega^{-2} = 1 - \frac{\alpha}{1 + \beta_R^2} \quad , \qquad (2\text{-}45)$$

$$\Omega Q_o = Q \left(1 + \frac{\alpha Q_o \beta_o}{1 + \beta_R^2} \right) \quad , \qquad (2\text{-}46)$$

where the coupling constant α, the reduced resonance frequency Ω and the impedance ratio of the interferometer β_o or β_R are defined as

$$\alpha = M^2/(L_1 L_2) \quad , \qquad (2\text{-}47)$$

$$\Omega = \omega_R/\omega_o \quad , \qquad (2\text{-}48)$$

$$\omega_o^2 = (L_1 C_1)^{-1} \quad , \qquad (2\text{-}49)$$

$$Q_o = \omega_o L_1/R_1 \quad , \qquad (2\text{-}50)$$

$$\beta_o = \frac{R_2}{\omega_o L_2} \qquad \text{and} \qquad \beta_R = \frac{R_2}{\omega_R L_2} \quad . \qquad (2\text{-}51)$$

Here the subscripts "1" and "2" refer to parameters associated with the rf tank and the interferometer respectively (Fig. 2.5). From Eqs. (2-45) and (2-46) the coupling constant α and the impedance ratio β_o can be expressed in terms of measurable quantities ω_o, ω_R, Q and Q_o. In many cases where the approximation $\omega_o L_2 > R_2$ is valid, α and β_o are given by

$$\alpha \cong 2(\Omega\text{-}1)(1 + \beta_o^2) \quad , \qquad (2\text{-}52)$$

$$\beta_o \cong \left(\frac{\Omega}{Q} - \frac{1}{Q_o}\right) 2^{-1} (\Omega\text{-}1)^{-1} \quad . \qquad (2\text{-}53)$$

The mutual inductance M can be measured directly by determining the dc current in the rf drive coil, I_{Φ_o}, required to change the interferometer flux by one flux quantum Φ_o:

$$M = \Phi_o / I_{\Phi_o} \quad . \qquad (2\text{-}54)$$

Since the coil inductance L_1 is known, using Eqs, (2-47) and (2-54) the ring inductance L_2 can also be determined. In this work L_2 was typically $\sim 3 \times 10^{-9}$ H, or an impedance of 0.2Ω at 10 MHz. Because of the low impedance level of these experiments, the difference in the dielectric constants of gaseous and liquid helium can give rise to errors in the measurements of resonance frequency due to a change in the liquid He level. The stainless steel coax was arranged so as to minimize the dielectric effect in frequency measurements.

2.4.7 Experimental Results

From the circuit analysis under the stated assumptions (2.4.5) in the small quantum effect limit an inductively coupled interferometer is expected to exhibit certain quantum interference effects. These quantum effects will show up as variations of the rf tank impedance from its classical behavior. Since the rf tank is driven from a constant current source, these impedance variations give rise to signal voltages. From Eq. (2-44) this signal (at the drive frequency) is expected to vary sinusoidally with dc magnetic flux with a period of 1 Φ_0 independent of temperature, frequency and rf drive level.

The analysis also leads us to expect a Bessel function J_1 oscillation of signal as the rf drive amplitude is varied, with a period of a flux quantum. The rf drive level required to produce a particular Bessel maximum (say, the first max.) scales like $R/(R + i\omega L)$ with the interferometer parameters. Hence for the same interferometer (i.e. the ratio of R/L fixed) the rf drive necessary for the first Bessel maximum increases with frequency for a circuit with $\omega L \gg R$, and is nearly

independent of frequency in the limit of $\omega L \ll R$. By the same token in different interferometers of different R/L ratios measured at the same frequency, the rf drive should scale like R/Z. For $R > \omega L$ a predominantly AM effect should appear, whereas for $\omega L > R$ the quantum effect would be manifested as an effective parametric reactive impedance and the FM signal becomes increasingly pure as $\omega L/R$ increases.

Since I_c and v_s increase with decreasing temperature, the signal amplitude is expected to grow as temperature decreases. At low temperature the drive flux must exceed certain critical flux before Bessel-like modulation of signal by rf flux would appear.

The fabrication techniques of quantum interferometers developed thus far allowed one to controllably vary the characteristic parameters of these structures including transition temperatures T_c' and T_c of the bridge and the main film, the normal resistance R, length ℓ, width W, thickness t and the critical current I_c of the bridge. Junction parameters were varied widely in the course of this study: $0.5\mu < \ell < 25\mu$, $1\mu < W < 300\mu$, $1.4° < T_c' < 4.2°K$, $10^{-3}\Omega < R < 0.5\Omega$, and $0.01 < R/\omega L < 1.2$. Typical values for the inductance of the interferometer are $(2\text{-}3) \times 10^{-9}$ H.

Typical rf circuit parameters at 30 MHz are: unloaded $Q_o \sim 550$, loaded Q varying between 60 and 400, tank inductance $L_1 \sim 10^{-7}$ H, capacitance $C_1 \sim 300$ pf and the coupling constant $\alpha = M^2/L_1L_2$ ranging from 0.01 to 0.04. Over fifteen interferometers with these wide ranges of physical parameters at different frequencies, coupling constants and material compositions were measured on different probes. An order of magnitude estimation for mutual inductance M is $\sim 10^{-9}$ H, the quantum

voltage $\Phi_o\omega \sim 0.4$ μV at 30 MHz, and I_c near T_c' approaches 10^{-7} μA.

The calculated absolute impedance ratio $R/\omega L$ based on measured values of frequency, Q and Eq.(2-53) is accurate to $\sim \pm$ 15% independent of the frequencies, coupling constants, Q and probes used in the measurements. The estimated absolute values for L and R of the interferometer, M, and α share the same accuracy of $\sim \pm$ 15%. However, relative values of some of these parameters could be determined to about 1 part in 10^4. It turned out to be difficult to determine these parameters with absolute precision much better than the stated $\sim \pm$ 15% when measurements were carried out in the presence of strong electromagnetic interference from nearby radio and TV stations and the power lines were subject to pulses from several accelerators in the same building. At 30 MHz the wavelength (10 m) is comparable to the lengths of the cables and the stainless steel coax cable connecting the room temperature instruments with the interferometer of 1.5 mm in radius at the bottom of a liquid helium bath. Thus the circuit analysis based on lumped parameters is no longer a good approximation. In determining the coupling constant α and the impedance ratio $R/\omega L$ of the interferometers (2-52 and 2-53), quantities like $(\Omega - 1)$ and $(\Omega Q^{-1} - Q_o^{-1})$ are each given by differences of two relatively large and comparable parameters (the typical normalized resonance frequency $\Omega \sim 1.01$ and Q, Q_o of the order $\sim 10^2$) with relative difference of the order of $10^{-2} - 10^{-3}$. Therefore the estimated value for α and $R/\omega L$ are sensitive to small uncertainties of a few percent in the determination of $(\Omega-1)$ and Q. It should also be noted that a $\sim \pm$ 15% accuracy determination of impedance implies an

uncertainty of about $\delta L_2 \sim 10^{-10}$ H in these measurements or a characteristic dimension of only 10^{-4} m .

Since the loaded Q increases with decreasing coupling between the rf tank and the interferometer, the product of αQ stays nearly constant for a given interferometer and rf tank throughout the measurable range of α. In this sense the general features to be described are to a large extent independent of the coupling constant. In general the operation of the interferometers depends strongly on the product of RI_c and the impedance ratio $R/(\omega L)$.

All of the general features described in this section (2.4.7) were observed on interferometers with several different impedance ratios $R/\omega L$. There are at least three different ways to vary this ratio: fabrication of interferometers of different R/L ratios, observations made on the same interferometer but at different frequencies, and variations of the temperature dependent resistance of the same bridge. Experimentally when the small critical current of the bridge is exceeded the resistance of the bridge is found to be the same as the normal resistance of the bridge for temperature T near T_c'. On the other hand, at sufficiently low enough temperature, the bridge region becomes so strongly superconducting that it is difficult to induce enough current to drive the bridge dynamically normal and thus R = 0. In between these two limiting values for R, the resistance of the bridge typically decreases as shown along the horizontal axis of Fig. 2.11a or b.

(A) DC and RF Characteristics. Figure 2.6 shows the typical signal variation with an applied dc magnetic field with period Φ_o. This sinusoidal dc periodicity is independent of rf drive levels over a span of three decades, is temperature independent to $<10^{-4}\ \Phi_o \sim 10^{-11}$ G-cm^2 at least over a range of $(1-T/T_c') < 0.7$ and shows no frequency dependence as expected from the analysis. It is this dc characteristics of the interferometer that forms the basis of using it as a magnetometer to be discussed in Part II of this thesis.

The dc magnetic flux can easily be adjusted to within $\sim 0.1\ \Phi_o$ and the rf frequency f to $\sim f/(10Q)\sim$ a few KHz of yielding maximum signal (Figs. 2.6 and 2.10). If the dc flux and frequency are so optimized as to give maximum signal at a given temperature near T_c' and held constant, the typical signal as a function of rf drive flux Φ_x is shown in Fig. 2.7. The signal amplitude represents the variation in impedance resulting from a change in the rf flux. A Bessel function type of oscillation is expected from Eq. (2-32). The rf drive level necessary to produce successive maxima can be estimated once the ratio R/Z is determined. The calculated and the experimentally measured values for the rf drive ΔI for one period of the Bessel-like response due to the quantum effect δI_s are shown in Table 1 for four interferometers and they agree to within ±15%. Table 1 also gives the length and width of the bridges ℓ/W, the frequency f at which the measurements were made, the effect of the coupling constant α and the quality factor Q, and the normal resistance R of the bridge.

When two interferometers of different $R/\omega L$ ratios are measured, the rf drive levels required to produce one period of the Bessel-like response scale roughly like the ratio of their $R/\omega L$ values for $R << \omega L$. Similarly

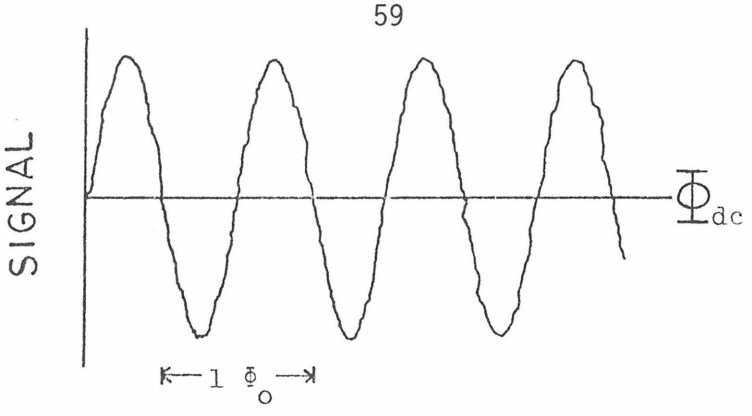

Fig. 2.6 Detected signal voltage across the tank circuit containing an interferometer as a function of an applied dc magnetic flux.

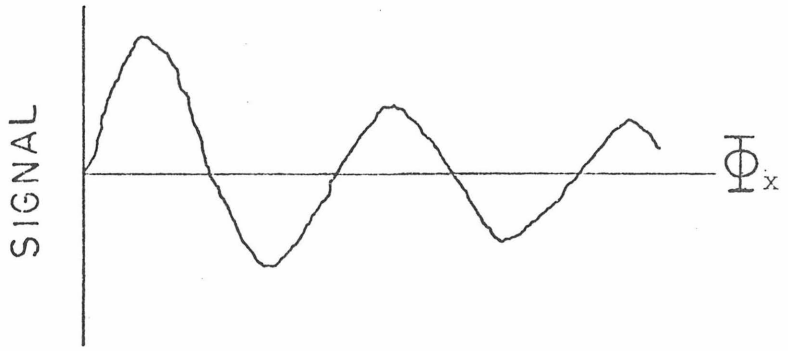

Fig. 2.7 Detected signal voltage as a function of the amplitude of applied rf magnetic flux Φ_x for temperature T near T_c' ($T \sim T_1$ of Fig. 2.8).

TABLE 1

No.	[c] ℓ/W (μ)	f (MHz)	α (%)	T (°K)	Q	αQ	L (10^{-9}H)	R (Ω)	$\frac{R}{\omega L}$	[a] $\Delta I_{measured}$ (μA)	[a] $\Delta I_{calc.}$ (μA)	[b] ΔT (°K)
1	0.8/20	30	1.15	3.8	170	2.0	1.8	0.14	0.43	1.8	1.9	0.04
				3.7	180	2.1		0.13	0.39	2.0	2.1	0.03_5
		30	2.3	4.0	103	2.3	1.7	0.15	0.46	1.7	1.8	0.05
				3.8	110	2.5		0.14	0.42	1.8_4	1.9_5	0.03
				3.7	113	2.5		0.11	0.34	2.2	2.4	0.02
2	0.75/36	30	1.15	4.2	286	3.3	2.7	0.089	0.17_8	2.7	3.0_5	0.1
				4.1	300	3.4_5		0.078	0.15_5	3.3	3.5	0.08
				4.0	340	3.9		0.063	0.12_5	3.4	4.3	
		10	1.2	4.2	134	1.6	2.1	0.082	0.63	0.9	1.1	>0.05
				4.1	142	1.7		0.057	0.44	1.4	1.6	0.03_5
3	1.1/20	30	2.55	4.2	74	1.9	3.3	0.42	0.67	0.66	0.65	0.02
				4.1	74	1.9		0.42	0.67	0.66	0.65	0.02
4	4.5/65	30	2.97	3.94	151	4.5	3.1_5	0.098	0.16_8	3.4	2.8	0.01
				3.935	184	5.5		0.073	0.12_4	4.4	3.8	

a. ΔI is the RMS value of the amount of rf current for one period of the Bessel-like response due to δI_s (Fig. 2.7).

b. ΔT is the interval of temperature between the adjacent zero signals as discussed in (2.4.7 D).

c. Length and width of the proximity effect bridge in an interferometer.

it is also verified that the rf drive level for one period of the Bessel-like response for the same interferometer measured at 30 MHz is about three times the rf level at 10 MHz if $\omega L >> R$.

(B) Temperature Dependence. Over a wide range of temperature ($1-T/T_c' < 0.2$, $T_c' \sim 4°K$), Fig. 2.8 shows the temperature dependence of the signal as the rf drive level is varied. At high temperature T_1 and T_2 where the analysis based on small quantum effect is expected to be valid, the amplitude increases with decreasing temperature indicating the onset of superconductivity and the increase of supercurrent. However a close examination of the temperature dependence of the signal in this temperature range reveals a complicated temperature dependence to be discussed in (D). The rf drive level necessary to produce the first Bessel-like maximum increases by some thirty-fold as temperature is lowered from T_1 to T_6 presumably because of the rapid rise in I_c as a function of decreasing temperature, $I_c \sim (T_c' - T)^{3/2}$. At lower temperature, more rf drive is needed to induce enough current in the interferometer so that the critical current of the bridge can be exceeded to bring about a quantum transition (the model for I_s (2-25) applies only for current greater than I_c).

At T_3 the first clear onset of critical flux discussed in (2.4.5) shows up and at lower temperature the pure Bessel character changes to a more complicated amplitude response. Such kind of complicated response is expected from the analysis when the quantum effect begins to seriously modulate the classical response. The large harmonic contents in (2-41) implies that contributions from mixings of higher harmonics to the

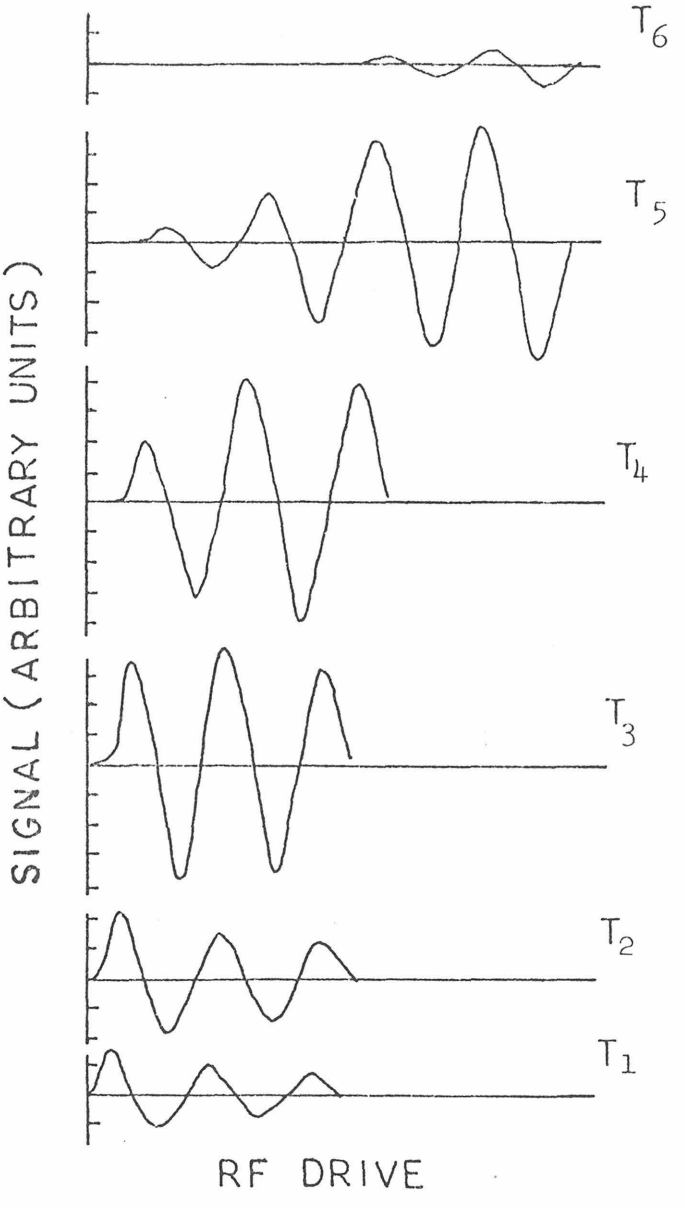

Fig. 2.8 Temperature dependence ($T_c' > T_1 > T_2 > \cdots > T_6$) of the typical interferometer response as a function of rf drive in the temperature range $1-T/T_c' < 0.2$.

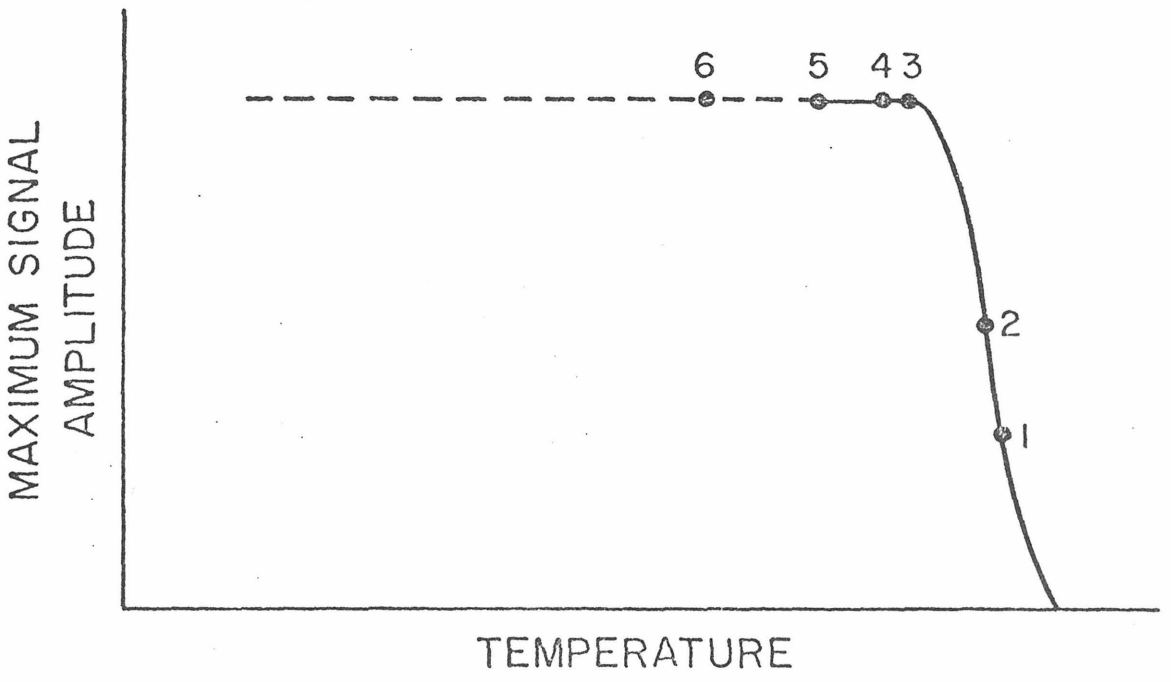

Fig. 2.9 Envelope of the maximum signal amplitude as a function of temperature. Near the transition temperature T_c', the maximum signal increases rapidly with decreasing temperature as does I_c or v_s until it saturates at about $(\omega M/R)\omega\Phi_o$ (dashed line).

amplitude at the drive frequency can cause considerable modification to the amplitude at the fundamental frequency as given in (2-43). Instead of the first peak of the Bessel-like response being the maximum signal, higher rf drive level produces bigger signal. The quantum signal seems to persist at the lowest temperature and is still periodic in dc flux but the rf drive level is set by the critical current.

As the temperature decreases, the effective dynamic resistance of the bridge decreases slowly (Fig. 2.11a or b) towards zero (as discussed earlier in this section) and a corresponding monotonic increase of resonance frequency f_R and Q as expected from (2-45) and (2-46) was also observed. The oscillating behavior of the signal as a function of the temperature will be discussed in (D) and 2.5.

The maximum signal amplitude as a function of temperature is shown in Fig. 2.9. The signal is optimized at each temperature as a function of rf and dc flux and frequency. Overall behavior of the signal near the transition temperature is a rapid rise in the amplitude with decreasing temperature, probably due to the temperature dependence of the factor v_s or I_c in (2-32), until it saturates at about $\omega\Phi_0\omega M/R$ (Eqs. 2-33 and 2-43) and remains there at low temperature (dashed line). Experimentally this saturation level can be estimated from the signal amplitude, gain of the amplifying system and Eq. (2-43) with the effective flux $(\Phi_x - \Phi_c)R/Z$ at about Φ_0/π for maximum Bessel-like response.

(C) Parametric Impedance. The effect of the relative impedance $R/\omega L$ of the interferometer on the signal as a function of the frequency near the resonance is shown in Fig. 2.10. The dashed line represents the frequency dependence of the magnetiude of the impedance of the rf tank

circuit inductively coupled to the quantum interferometer. The variation of this impedance due to one quantum change of the flux in the ring (i.e. r.f. drive level set at first Bessel maximum) for a constant dc and rf bias is given by the solid curve.

If the resistance of the bridge, R,is small compared to the inductive impedance of the superconducting ring, ωL, then primarily frequency modulation (FM) effects are expected. FM effect is equivalent to a shift in resonance frequency and thus a translation of the resonance curve with respect to the purely classical response of such an rf inductively coupled circuit. Such FM effect as observed is shown in Fig. 2.10a which is indicative of an effective parametric reactance as anticipated (Eq. 2-34b). For $R << \omega L$ the magnitude of the two peaks of the signal is about equal and the excursions are anti-symmetric with respect to the resonance frequency as expected from a nearly pure FM effect.

For $R \gtrsim \omega L$ the signal is nearly symmetric and always of the same sign (solid curve in Fig. 2.10b). The impedance response in this limit is mainly of amplitude modulation (AM). The interferometer essentially acts as a parametric resistance as expected (Eq. 2-34a).

For certain interferometers with the proper choice of the impedance ratio, it is possible to observe the transition from predominantly AM to FM effects at a fixed tank frequency as the resistance decreases slowly with decreasing temperature. For example it was observed that the same interferometer (#1) with $R/\omega L \sim 0.48$ at 4.1°K (measured at 30 MHz) exhibits predominantly an AM effect between 4.1 and 3.7°K and gradually switches to an FM effect at around 3.7°K with a corresponding drop $R/\omega L$ to ~ 0.3 (Fig. 2.11a), presumably due to the decrease of R as indicated

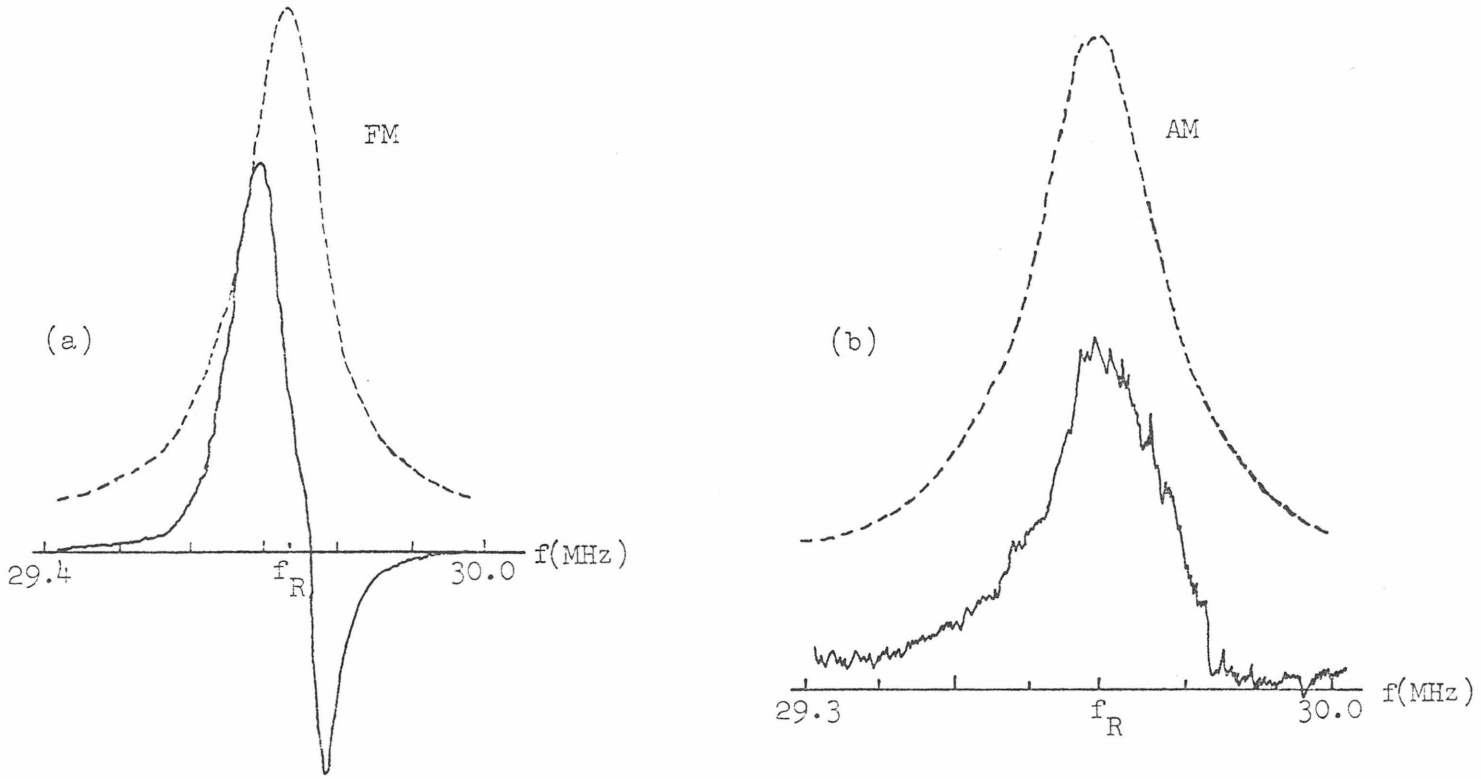

Fig. 2.10 The dashed line represents the frequency dependence of the magnitude of the impedance of an rf tank circuit inductively coupled to an interferometer. Solid curve shows the variation of this impedance due to one quantum change of the flux in the ring. (a) and (b) correspond to situations with $R/\omega L$ of about 0.3 and 0.5 respectively with the rf drive level set at the first Bessel-like peak.

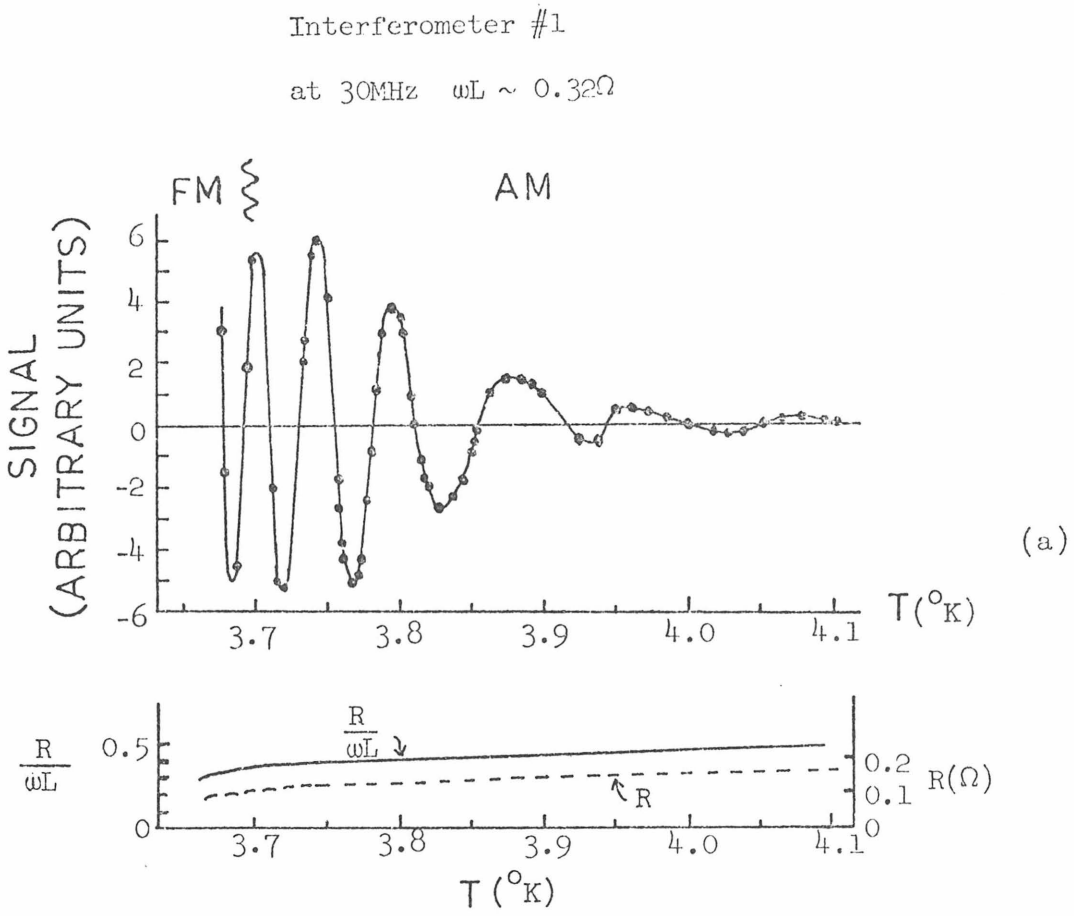

Fig. 2.11a Temperature dependence of the interferometer response, the resistance R of the bridge and the approximate impedance ratio $R/(\omega L)$ of the interferometer for temperature T near T_c'. In (a) the response of Interferometer #1 (measured at 30 MHz with $R/(\omega L) \sim 0.5$ near 4.1°K) changes slowly from a predominantly AM effect to a FM effect at about 3.7°K due to a decrease in the impedance ratio. The rf drive level is set at the value so as to yield the first Bessel-like peak at $T \sim T_c'$.

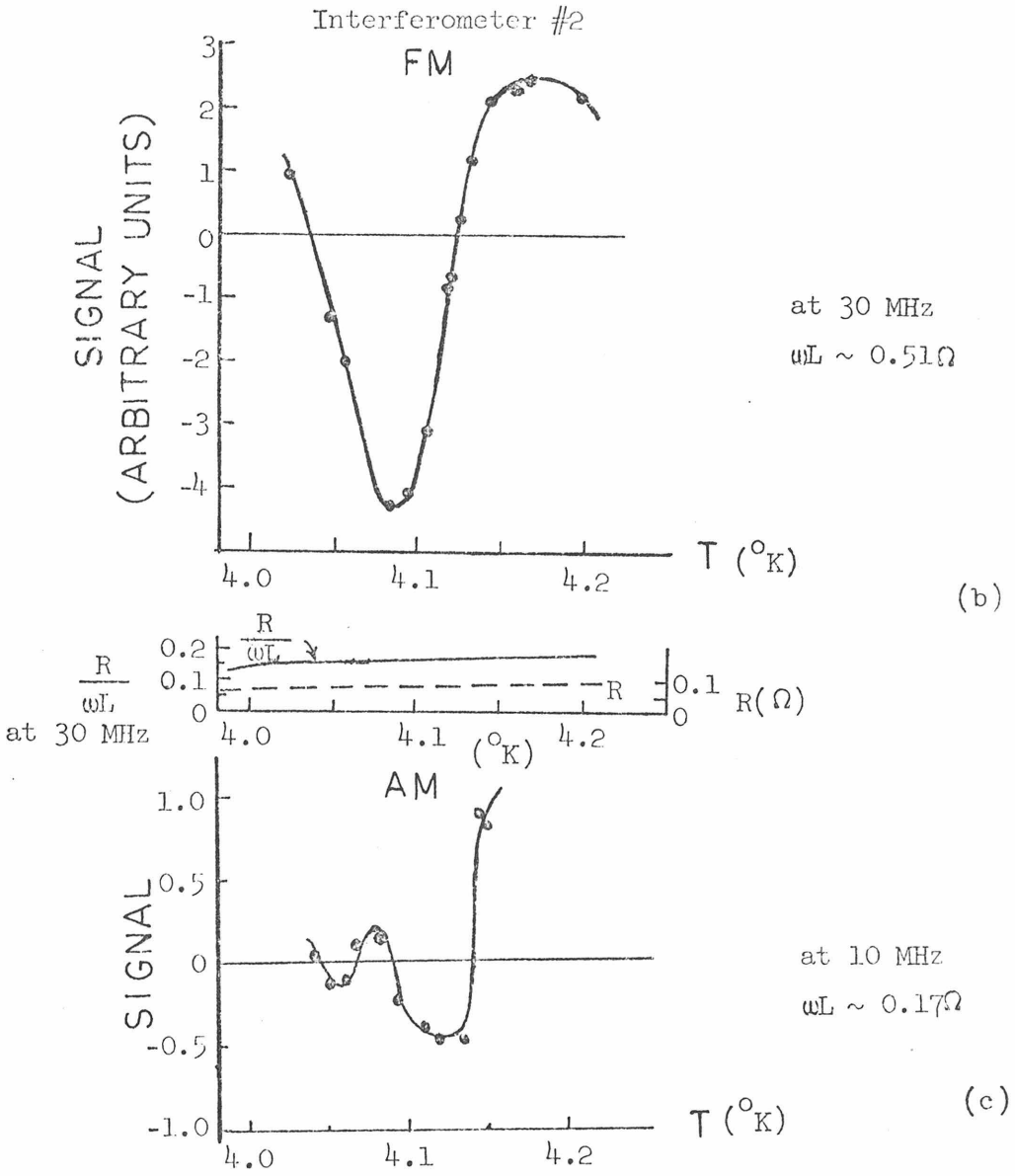

Fig. 2.11 b,c The response of Interferometer #2 measured at 30 MHz and 10 MHz are shown in (b) and (c) respectively. The change of the impedance ratio in going from 30 to 10 MHz not only changes the response from an FM to an AM effect, but also makes the "period" of the temperature-modulated signal smaller as discussed in (2.5). The rf drive level is set for the first Bessel-like peak.

in the figure. Figure (2.11c) shows the result of a second interferometer (#2) with $R/\omega L \sim 0.52$ at 10 MHz very close to the value of #1 at 30 MHz. Since in both cases (Fig. 2.11a and c) the impedance ratio $R/\omega L$ is about 0.5, both of them show AM effects as expected. On the other hand, the same interferometer (#2) measured at a higher frequency of 30 MHz and hence a lower $R/\omega L \sim 0.17$ shows up mainly as an FM effect as indicated in Fig. (2.11b).

As discussed before, the rf drive required to bring about a first Bessel maximum should scale like $R/\omega L$ for $\omega L >> R$. Experimentally the rf drive level for the first Bessel maximum at 30 MHz reduces by the expected factor of three when the same interferometer (#2) is measured at 10 MHz. For the same interferometer at a given frequency, the rf drive level needed to reach the first Bessel maximum was found experimentally to increase slowly in proportion to the increase of $\omega L/R$ with decreasing temperature and R.

In passing we would like to point out that the exact functional dependence of the suppercurrent I_s on the dissipating voltage U(t) is not important in arriving at the conclusion as expressed in Eq. (2-34). If a sine function $\sin\Delta\tilde{\phi}$ (as in a Josephson junction) instead of $(1 + \cos\Delta\tilde{\phi})$ has been used, it would lead to essentially the same interference effect of $\delta I_s \sim J_1(\Phi'_x)\sin\Phi'_{dc}$. In fact, any reasonable periodic function of $\Delta\tilde{\phi}$ which passes through zero twice per cycle would give the same qualitative feature.

The experimental results described up to now are all consistent with the phase slip model and the equivalent circuit developed for the time-dependent dissipating state of superconductivity which accompanies

quantum phase transitions. Thus under the stated assumptions the model used for the proximity effect bridge and the circuit analysis for the rf coupled interferometer can adequately describe and explain quantitatively (to within the experimental accuracy ~±15%) the absolute magnitude of experimental observations in their proper limits.

(D) Temperature-Modulated Signal Near the Transition Temperature.

In addition to the above experimental results it was also observed for the first time that near the transition temperature T_c' the induced impedance due to quantum effects oscillates in phase as a function of temperature. In other words, there are certain temperatures at which the signal vanishes, while above and below this temperature the signal reappears with opposite signs. Such a temperature-dependent oscillation of δI_s is <u>not</u> expected from the analysis made so far (2-44) and is indicative of the possible breakdown of certain assumption used in the analysis. Before we assess the validity of the assumptions and the analysis, we will first describe the experimental observations.

Near the transition temperature T_c' of the bridge ($1-T/T_c' \lesssim 0.07$) the temperature dependence of the quantum interference signal for very short bridges ($\ell \sim 0.8\mu$) is shown in Fig. 2.11 where the frequency, dc and rf flux were optimized and held fixed throughout this temperature range. Curves a, b, and c are for different impedance ratios. The oscillation "period" of the signal decreases with decreasing temperature and seems to be inversely proportional to R.

The operating temperature range is usually smaller than 0.2°K for longer bridges due to a weaker overlap of the superconducting wavefunctions from the neighboring regions. Since the resistance in these

longer bridges are usually higher, the "period" in temperature is smaller. Hence such interferometers are more sensitive to small variations in the temperature especially at lower temperature as compared to shorter bridges.

Figures 2.11a and b show the temperature-modulated signal as a function of temperature. Both interferometers 1 and 2 were measured at the same rf frequency of 30 MHz and have the inductive impedance $\omega L \sim 0.32\Omega$ and 0.51Ω respectively. The resistance of the first interferometer is nearly 1.5 times that of the second with a slight temperature dependence as shown. The impedance ratio $R/\omega L$ for #1 and #2 interferometers are about 0.48 and 0.18 respectively at high temperatures. It is difficult to determine the critical current for these interferometers at temperature close to T_c' of the bridge. Since both of these bridges are relatively short, 0.8μ and 0.75μ long respectively, the critical currents are expected to depend exponentially on $(T_c'-T)$ for T near T_c' and gradually the temperature dependence of I_c becomes $(T_c'-T)^{3/2}$ as discussed in (2.2). Although the critical current may be estimated at low temperature from the critical shielding flux (Fig. 2.8), extrapolation of I_c to higher temperature is at best difficult because of lack of knowledge of both T_c' and the temperature at which the exponential dependence of I_c on $(T_c'-T)$ switches over to the 3/2 power. However the general trend for the oscillating period in temperature seems to be decreasing with increasing normal resistance. The envelope of the oscillating signal increases rapidly as temperature decreases and eventually levels off at low temperature (Fig. 2.9).

For the same interferometer measured at different frequencies (10 and 30 MHz), this period in temperature is directly proportional to the frequency (Fig. 2.11b and c, and Table 1).

Since at the zero crossing point, the signal is independent of the applied dc or rf magnetic flux at that temperature, this disappearance of signal cannot be due to any paramagnetic impurity enclosed by the interferometer or a change in the rf bias level. These observations can be emparically summarized as some Bessel-like function J(x) with its argument x proportional to $Rf(T)/\omega$ for T near T_c' where f(T) is some temperature dependent function increasing monotonically with increasing $(T_c'-T)$. The oscillation period in temperature is found to be independent of the coupling constant α, although in these experiments it was impossible to independently vary α and the quality factor, Q.

A plausible explanation for this phenomenon based on a non-equilibrium correction to the Josephson frequency-voltage relation will be developed in the next section and can adequately account for the experimental observations.

2.5 Non-Equilibrium Superconductivity

2.5.1 Non-Equilibrium Processes in Superconductors.

Most of the equilibrium phenomenon in superconductors can be understood in the framework of BCS theory. Being a model for the description of equilibrium superconductivity, the microscopic (BCS) theory does not explain how equilibrium is established through non-equilibrium processes. The study of non-equilibrium mechanisms in superconductivity is a developing and not well understood area. Recently, considerable attention has been devoted to problems like depairing processes at super-normal (S/N) and super-weak (S/W) interfaces[19,20], the motion and structure of the fluxoid[47] and the time-dependent Josephson-like behavior of weak superconductivity as observed in proximity effect bridges. The experimental

observations described in 2.4.7(D) and shown in Fig. (2.11) are believed to be the first direct probing of another aspect of non-equilibrium superconductivity hitherto unexplored -- the non-equilibrium quantum interference phenomenon in superconductors.

At thermal equilibrium, the gauge-invariant electrochemical potentials of Cooper pairs $\tilde{\mu}_p$ and of quasiparticles $\tilde{\mu}_e$ are equal. A number of possible mechanisms resulting in perturbations of the condensate and/or quasiparticles were mentioned in Section (1.2). Some of the better understood processes can be summarized as follows:

(A) Thermalization. Without loss of generality, we consider quasiparticles in the electron-like branch $k_> > k_F$ where k_F is the Fermi wave vector. If electron-like quasiparticles are injected into a superconductor, the quasiparticles within this branch (of density $n_> > n_<$ of the hole-like branch) would cool down to the lattice temperature through phonon emission. The thermalization time τ_{TH} required is typically[20] $\tau_{TH} \sim 2 \times 10^{-10}$ sec.

(B) Branch Mixing. The injected quasiparticles can cause an imbalance of the densities of the quasiparticles in the two momentum branches. Equilibrium between the two branches can be re-established largely through inelastic phonon scatterings resulting in crossing of quasi-particles from one branch to the other over a time period referred to as the branch mixing time τ_Q[48]:

$$\tau_Q(T) = 0.068\ \tau_\theta \left(\frac{\theta}{T_c}\right)^3 \frac{\Delta(0)}{\Delta(T)} \quad . \qquad (2\text{-}55)$$

where τ_θ is the electron-phonon scattering time at the Debye temperature θ of the lattice ($\tau_\theta \sim 10^{-14}$ sec for normal metal) and $\Delta(T)$ is the temperature dependent gap energy of the superconductor. For tantalum, $\tau_Q(0) = 0.65 \times 10^{-10}$ sec.

(C) Recombination of Quasiparticles. When equal numbers of quasiparticles are generated in both branches either by external pair breaking processes such as phonon or photon excitations or upon completion of thermalization and branch mixing processes in the case of quasiparticle injection, these excess quasiparticles depress the energy gap and are out of equilibrium with the condensate. To achieve electrochemical equilibrium with the condensate these quasiparticles can emit phonons and recombine into Cooper pairs. Since the quasiparticle population is described by the Fermi distribution, the recombination time τ_R at low temperature ($T \lesssim 0.9\ T_c$) is of the form[49]

$$\tau_R = \Gamma_R T^{-1/2} e^{\Delta/kT} \qquad \text{for } \Delta \gtrsim kT \quad . \qquad (2\text{-}56)$$

With Γ_R ranging from 2×10^{-8} sec-°$K^{-1/2}$ for aluminum to 2×10^{-12} sec-°$K^{-1/2}$ for lead.

However, it is not clear which, if any, of these processes is the controlling mechanism (or bottleneck) in maintaining the phase equilibrium which is necessary for quantum interference effects. In this section (2.5) a model based on non-equilibrium quantum interference effects in weak superconductors will be proposed as a possible cause for the temperature-dependent signal described in 2.4.7(D). One analytic approach adopted here is to use time-dependent Ginzburg-Landau (TDGL) theory in investigating the non-equilibrium relaxation process first at S/N and S/W interfaces, then apply it to S/W/S structure in an electric field.

2.5.2 The Two-Potential Concept

At thermodynamic equilibrium, the free energy of the superconducting

condensate F

$$F = \int d^3x \left\{ a|\Psi|^2 + \frac{b}{2}|\Psi|^4 + \frac{h^2}{2m}\left| \left(\nabla - \frac{i2q}{\hbar} A\right)\Psi \right|^2 \right\} \quad ,$$

as originally introduced by Ginzburg and Landau[50] is at a minimum and the gauge-invariant electrochemical potentials of the pairs and quasiparticles are equal ($\tilde{\mu}_p = \tilde{\mu}_e$). In TDGL theory it is assumed that perturbation of the condensate can lead to a difference of the two potentials ($\tilde{\mu}_p \neq \tilde{\mu}_e$) with the quasiparticles remaining in thermal equilibrium with the lattice. In the absence of an applied magnetic field the perturbed condensate relaxes back to its equilibrium electrochemical potential $\bar{\mu}_e$ by releasing the extra amount of free energy according to TDGL as:

$$\left(\frac{\partial}{\partial t} + \frac{2i\bar{\mu}_e}{\hbar}\right)\Psi = \frac{1}{a\tau_{GL}} \frac{\delta F}{\delta \Psi^*} \qquad T \text{ near } T_c \quad , \qquad (2\text{-}57)$$

where a is the usual GL coefficient[50], δF is the deviation in F from equilibrium[22], and the GL relaxation time of the condensate, τ_{GL}, is given by the microscopic theory:

$$\tau_{GL} = \hbar\pi(8k|T_c - T|)^{-1} \cong 10^{-12}|T_c - T|^{-1} \text{ sec-°K} \quad . \qquad (2\text{-}58)$$

The time evolution of the wavefunction is given by Eq. (1-17) or $\Psi = \sqrt{\rho_s}\, e^{-2i\int \tilde{\mu}_p dt}$ and the supercurrent density (Eq. 1-4) can be rewritten as

$$\vec{j}_s = -\frac{n_s q}{m}\left(\int 2\nabla\bar{\mu}_p \, dt + 2q\vec{A}\right) \quad . \qquad (2\text{-}59)$$

In the absence of a temperature gradient, the quasiparticles

obey the Ohm's Law:

$$\vec{j}_n = -(\sigma/q)(\nabla\bar{\mu}_e + q\frac{\partial\vec{A}}{\partial t}) \quad , \qquad (2\text{-}60)$$

where $\bar{\mu}_e$ is the electrochemical potential of the quasiparticles and the effective conductivity of the quasiparticles σ can be taken as the normal conductivity of the metal for T near T_c.[20] The fact that, even in the absence of $\nabla\bar{\mu}_p$ and $\nabla\bar{\mu}_e$, j_s and j_n are $\pi/2$ out of phase (comparing Eqs. 2-59 and 2-60) when driven by an oscillating $\vec{A}(t)$ has some interesting and important consequences to be discussed later.

Based on the assumption of a two fluid model and the concept of two different electrochemical potentials in a non-equilibrium region, Rieger et al. (RSM)[22] conclude that there is a general relationship between $\bar{\mu}_p$, $\bar{\mu}_e$ and $\nabla\cdot\vec{j}_s$. Recall that $\bar{\mu}_p$ has been defined such that $-2q\bar{\mu}_p = h\dot{\phi}$ (1-14),

$$\bar{\mu}_p - \bar{\mu}_e = \frac{m\,\xi^2(T)}{4e\,\tau_{GL}} \cdot \frac{\nabla\cdot\vec{j}_s}{|\psi|^2} \quad , \qquad (2\text{-}61a)$$

where the charge of an electron is $q = -e < 0$. A finite divergence of j_s implies pairing and depairing processes accompanied by an electric field on the superconducting side of the interface. From the definitions of the gauge-invariant electrochemical potentials (1-18) and (1-20), the result of the RSM analysis can be extended to include the magnetic potential as

$$\tilde{\mu}_p - \tilde{\mu}_e = \frac{m\xi^2}{4e\tau_{GL}} \frac{\nabla\cdot\vec{j}_s}{|\psi|^2} \quad . \qquad (2\text{-}61b)$$

That the potentials $\tilde{\mu}_p$ and $\tilde{\mu}_e$ are different in a non-equilibrium steady superconducting state has been shown in experiments of quasiparticle

injection at the S/N and S/W interfaces[19,20] to be in qualitative agreement with (2-61); but that the relaxation time is longer than τ_{GL}.

The underlying assumption in the derivation of (2-61) is that the relaxation rate of the order parameter is taken as proportional to the deviation of the free energy from its equilibrium value. One of the important physical consequences of this two-potential concept is a modification[22] of the Josephson frequency-voltage relation (Eq. 2-4 or 2-6), which is a thermodynamic equilibrium relationship[51] where the pair and quasiparticle potentials are equal $\tilde{\mu}_p = \tilde{\mu}_e$, in non-equilibrium situations.

2.5.3 Non-equilibrium Quantum Interference Phenomenon

In this section a physical model for non-equilibrium quantum interference will be proposed which can adequately explain the temperature-modulated quantum interference phenomenon reported in 2.4.7(D). The physical origin of this interference effect lies in the possibility of pair-quasiparticle interconversion processes in a non-equilibrium region of a superconductor where locally the gauge-invariant electrochemical potentials of pairs and quasiparticles may differ from each other (Eq. 2-61). At equilibrium the free energy of the condensate is a minimum. In the presence of a gauge-invariant electrochemical potential gradient $\nabla\tilde{\mu}_p$ the supercurrent density j_s accelerates according to the London Eq. (2-19) reproduced here for convenience:

$$\frac{\partial j_s}{\partial t} = \frac{\nabla\tilde{\mu}_p/q}{-\frac{m}{2n_s q^2}} = \frac{\hbar\nabla\dot{\tilde{\phi}}}{\frac{m}{n_s q}} \quad , \qquad (2\text{-}62)$$

where $\tilde{\phi}$ is the gauge-invariant phase, $n_s = 2|\Psi|^2$, and $\nabla\tilde{\mu}_p = \nabla\tilde{\mu}_e = \nabla\mu_e - qE$ (here the first equality arises from the thermodynamic equilibrium condition and the second equality from the definition given by Eq. 2-5) as before. For a harmonic potential $\tilde{\mu}_p \sim e^{i\omega t}$, the current would also vary harmonically in time, $j_s \sim e^{i\omega t}$, and the London Eq. (2-62) becomes

$$j_s = \frac{-\nabla\tilde{\mu}_p/q}{\frac{i\omega m}{2n_s q^2}} = \frac{\hbar\nabla\tilde{\phi}}{\frac{m}{n_s q}} \quad . \qquad (2\text{-}63)$$

At equilibrium the potentials of the pair and the quasiparticles are the same, $\tilde{\mu}_p = \tilde{\mu}_e$, which is one of the assumptions made in the earlier circuit analysis for the rf coupled interferometer.

Out of thermodynamic equilibrium the perturbed condensate has a higher free energy than at equilibrium. If the system is given enough time, it would relax back to its equilibrium state by releasing some of the excess energy, for example by pair-quasiparticle interconversion. Within the equilibrium region, in general the supercurrent can be described by the simple relation of Eq. (2-63). In the non-equilibrium regime because of the depairing process (Eq. 2-61) some of the supercurrent is converted into the normal current. We propose that it is the interconversion of the resistive normal current and the inductive supercurrent in the non-equilibrium region that is mainly responsible for the temperature-modulated quantum interference effect of the preceeding section.

Our approach here is to relax the thermodynamic equilibrium condition used in the early analysis to allow two distinct and different

potentials to develop in the non-equilibrium regime. And unless otherwise explicitly stated, the assumptions and approximations introduced in the early analysis (2.4) will be retained in this section (2.5.3) at the respective steps as they appeared before. In order to define a non-equilibrium region, a steady state "healing length" will be introduced as a guide to the possible spatial extension over which non-steady situations may exist. An expression will be advanced relating the supercurrent and/or phase gradient to a normal potential. It will be shown that if the period of the harmonic potential $\sim\omega^{-1}$ is comparable to a relaxation time τ_s, it may lead to interference of the two "tails" of a wavefunction brought together at the bridge region of an interferometer due to relaxation processes. This is followed by a consideration of possible temperature dependence of τ_s, and a discussion of the non-equilibrium interference expression. Finally this idea will be applied to the earlier circuit analysis with due modifications leading eventually to a possible explanation for the observed temperature-modulation effect in quantum interference.

In the analysis of (2.4) it was assumed that the relaxation time is given by the G-L relaxation time τ_{GL} and that it is so short compared to an rf period ($\tau_{GL}\omega << 1$) that the pairs and quasiparticles are essentially at equilibrium most of the time, $\tilde{\mu}_p = \tilde{\mu}_e$. Since τ_{GL} increases as the temperature approaches the transition temperature T_c' of the bridge from below, it is conceivable that near T_c' this approximation of $\tau_{GL}\omega << 1$ may no longer be valid. Recall that the density of superconducting electrons $n_s = 2|\Psi|^2$ (Eq. 1-3) and the

electron charge $q = -e$, then Eq. (2-61a) can be written as

$$\bar{\mu}_p = \bar{\mu}_e - \frac{m\xi^2}{2q\tau_{GL}n_s}\nabla \cdot \vec{j}_s \quad . \qquad (2\text{-}64)$$

By Eq. (1-14), $-\hbar\dot{\phi} = 2\bar{\mu}_p$ the above equation then becomes

$$-\hbar\dot{\phi} = 2\bar{\mu}_p = 2\bar{\mu}_e - \frac{m\xi^2}{2qn_s\tau_{GL}} \nabla \cdot \vec{j}_s \quad . \qquad (2\text{-}65)$$

In the steady state, charge conservation requires

$$\nabla\cdot\vec{j} = \nabla\cdot(\vec{j}_s + \vec{j}_n) = 0 \quad . \qquad (2\text{-}66)$$

Hence using the fact that

$$\nabla\cdot\vec{j}_s = -\nabla\cdot\vec{j}_n = \frac{\sigma}{q}\nabla^2\bar{\mu}_e \quad , \qquad (2\text{-}67)$$

and if at steady state $\bar{\mu}_p$ is constant then

$$-\hbar\nabla\dot{\phi} = 2\nabla\bar{\mu}_p = 0 \quad , \qquad (2\text{-}68)$$

and the spatial extension of this effect is governed by

$$\nabla^2(\bar{\mu}_p-\bar{\mu}_e) - \frac{2n_sq^2\tau_{GL}}{m\xi^2\sigma}\ (\bar{\mu}_p - \bar{\mu}_e) = 0 \quad . \qquad (2\text{-}69)$$

The coefficient of $(\bar{\mu}_p-\bar{\mu}_e)$ defines a temperature-dependent "healing length" for the potential difference and is numerically of the order of $\sim 2\xi(T) \sim (T_c-T)^{-1/2}$. [22]

Figure 2.12 illustrates schematically the spatial dependence of the magnitude of the order parameter $|\Psi|$ plotted at the top (a), the super- and the normal current densities and the $\nabla\cdot\vec{j}_s$ in the center (b), and the electrochemical potentials of the pairs $\bar{\mu}_p$ and the quasiparticles $\bar{\mu}_e$ in the bottom (c) at a current-carrying S/N interface. As shown in (a) the magnitude of the order parameter vanishes deep inside the normal region. In the vicinity of a S/N boundary (Fig. 2.12c) at steady state the electrochemical potential of the pair $\bar{\mu}_p$ stays constant on the superconducting side of the interface and may extend slightly into the normal region due to the proximity effect (2.1) until thermal fluctuation destroys superconductivity. The quasiparticle potential $\bar{\mu}_e$ differs from $\bar{\mu}_p$ beginning on the superconducting side of the interface with localized excess quasiparticles due to depairing and deep inside the normal metal the slope of $\bar{\mu}_e$ is determined by the local electric field.

Experimental results on potential measurements very close to the current biased S/N interfaces (with probes placed on the superconducting side of the interface) have confirmed the existence of two distinct potentials $\bar{\mu}_p$ and $\bar{\mu}_e$ near the boundary.[19,20] In these experiments, on dc current biased S/N interfaces, a better quantitative agreement of $(\bar{\mu}_p-\bar{\mu}_e)$ and its temperature dependence with the theoretical predictions are obtained if the limiting relaxation time is assumed to be the branch mixing time $\tau_Q(T)$ rather than $\tau_{GL}(T)$ and the healing length is much longer than expected above (Eq. 2-69).[20] Thus in steady state Eq. (2-69) is qualitatively correct and the phase ϕ may remain constant on the superconducting side of the depairing region even though a

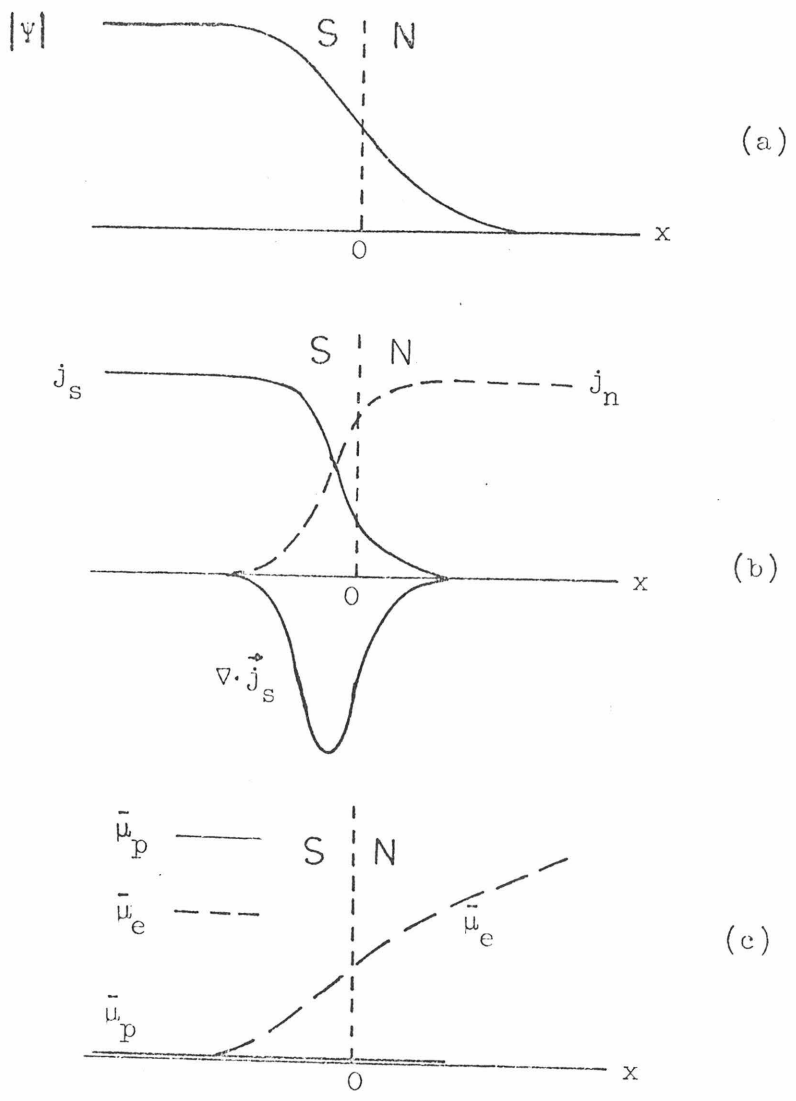

Fig. 2.12 Schematic representation of the spatial dependence of (a) the magnitude of the order parameter $|\Psi|$, (b) the supercurrent and normal current densities, as well as $\nabla \cdot \vec{j}_s$, (c) the electrochemical potentials of the pairs ($\bar{\mu}_p$) and the quasiparticles ($\bar{\mu}_e$), at a current-carrying S/N interface region.

voltage $\bar{\mu}_e/q$ exists within this region. Both theories (RSM and branching mixing) have very similar form. That the branch mixing time seems to be the bottleneck in the relaxation processes is not unreasonable since the quasiparticles are injected with a large imbalance between the two branches (usually $n_> >> n_<$). Being a phenomenological theory, the RSM theory cannot provide a detailed microscopic description of the non-equilibrium processes, but it does introduce a simple formalism for a generalized relaxation loss process in superconducting dynamics. Henceforth we will use τ_* instead of τ_{GL} in (2-61b) to represent some generalized relaxation time.

The second term in (2-65) is in effect a correction to the Josephson frequency-voltage relation (1-14) or (2-6), but in the steady state (2-68), $\bar{\mu}_p$ = constant, this correction effect does not show up. In order to be able to follow the physical idea without getting lost in trying to solve a complicated mathematical equation, we make the simplifying assumption that the supercurrent on either side of the weak region is related to the gradient of the phase as given by (2-62) while current through the weak region may depend on the phase difference.

For a non-stationary state, it is difficult to solve Eq. (2-61b) analytically for the effect of the correction term $(\sim\nabla\cdot\vec{j}_s)$ on phase $\tilde{\phi}$ without explicit knowledge of the exact functional forms of the potential $\tilde{\mu}_e$ and the supercurrent density j_s in the vicinity of the interface. The approach taken here is to look for the response of supercurrent or rather the phase gradient $\nabla\tilde{\phi}$ to the gradient of the quasiparticle potential $\nabla U = \nabla\tilde{\mu}_e/q$ in the limit of very weak

superconductivity where the superconducting electron density n_s is strongly position-dependent in comparison with the spatial dependence of the phase, and the coherence length ξ and the relaxation time τ_* in (2-61b) are taken as their equilibrium values.

Making use of the definitions $n_s = 2|\Psi|^2$, $q = -e$, and the relation $-\hbar\dot{\tilde{\phi}} = 2\tilde{\mu}_p$, Eq. (2-61b) becomes

$$-\hbar\dot{\tilde{\phi}} = 2qU - \frac{m\xi^2}{q\tau_*}\frac{1}{n_s}\nabla\cdot\vec{j}_s \qquad . \qquad (2\text{-}70)$$

Due to phase coherence in the superconducting ring we use, we can approximate $\oint \nabla\tilde{\phi}\cdot d\vec{r} \sim 2\pi$ or $\nabla\tilde{\phi} \sim d^{-1}$ where d is the diameter of the ring (3 mm); whereas the distance over which significant change of n_s occurs is of the order of a few coherence length ξ, $\nabla n_s/n_s \sim \xi^{-1}$, and thus we assume in the one-dimensional case

$$\frac{\nabla\cdot\left(\frac{\nabla n_s}{n_s}\right)}{\left(\frac{\nabla n_s}{n_s}\right)} >> \frac{\nabla^2\tilde{\phi}}{\nabla\tilde{\phi}} \qquad . \qquad (2\text{-}71)$$

Under such circumstances using the above mentioned assumption $j_s = n_s q\hbar\nabla\tilde{\phi}/m$, then the gradient of Eq. (2-70) is

$$\frac{-\hbar}{2q}\nabla\dot{\tilde{\phi}} = \nabla U - \frac{\xi^2\hbar}{2q\tau_*}\nabla\left[n_s^{-1}\nabla\cdot(n_s\nabla\tilde{\phi})\right] \qquad , \qquad (2\text{-}72a)$$

which upon using the approximation (2-71) and dropping all higher order terms in $\nabla\phi$ (i.e. $\left[\frac{\nabla n_s}{n_s}\cdot\nabla\right]\nabla\tilde{\phi}$ and $\nabla\left[\nabla^2\tilde{\phi}\right]$), reduces to:

$$\frac{\hbar}{2q}\left[-\nabla\dot{\tilde{\phi}} + \frac{\xi^2}{\tau_*}(\nabla\tilde{\phi}\cdot\nabla)\left(\frac{\nabla n_s}{n_s}\right)\right] = \nabla U \quad . \qquad (2\text{-}72)$$

For a nonsteady state where the potential U varies harmonically in time, to first approximation the phase and hence $\nabla\tilde{\phi}$ would also behave in a harmonic manner (which is true at thermodynamic equilibrium, for $2qU \equiv 2\tilde{\mu}_e = 2\tilde{\mu}_p = -\hbar\dot{\tilde{\phi}}$) and thus $U \sim \nabla\tilde{\phi} \sim e^{i\omega t}$. In the very weak limit ($j_n >> j_s$) the spatial dependence of the quasiparticle potential is mainly determined by the normal current density as the Ohmic law $j_n = \sigma E \sim -\sigma\nabla U$. And in the limit of steady state ∇U is constant in space deep inside the normal region. With this consideration in mind, in the one-dimensional case Eq. (2-72) becomes:

$$\nabla\tilde{\phi}\left[-i\omega + \frac{\xi^2}{\tau_*}\nabla\cdot\left(\frac{\nabla n_s}{n_s}\right)\right] = \frac{2q\nabla U}{\hbar} \quad . \qquad (2\text{-}73)$$

Spatial integration of $\nabla\tilde{\phi}$ in this equation leads to

$$\Delta\tilde{\phi} = \int \frac{\nabla U' \, dx}{-i\omega + \frac{\xi^2}{\tau_*}\nabla\cdot\left(\frac{\nabla n_s}{n_s}\right)} \quad , \qquad (2\text{-}74)$$

where we have normalized the potential U according to (2-26). In general, the integration in (2-74) cannot be performed without explicit knowledge of the spatial dependence of ∇U and n_s, but formally we can integrate (2-74) and express the result as follows

$$\Delta\tilde{\phi} = \frac{U'}{-i\omega + \tau_s^{-1}} \quad , \qquad (2\text{-}75)$$

where an effective relaxation time τ_s is defined to include the effect of integration and

$$\tau_s^{-1} \cong \frac{\xi^2}{\iota_*} \nabla \cdot \left(\frac{\nabla n_s}{n_s} \right) \quad . \qquad (2\text{-}76)$$

Equation (2-75) is the consequence of an attempt in seeking a solution of the quantum phase difference to Eq. (2-61b) in the non-stationary state. Without detail knowledge of the spatial dependence of n_s, j_s and U, we have resorted to looking for a solution in the weakly superconducting limit and for temperature T near T_c'. In this limit by making a few simplifying assumptions, we have arrived at the result given in (2-75) which is probably correct in indicating the qualitative feature of the phase difference $\Delta\tilde{\phi}$ across a non-equilibrium region. A detail functional dependence of $\Delta\tilde{\phi}$ on various parameters naturally depends on the degree of validity in the approximations and assumptions made. However a quantitative functional expression of the phase difference is not expected to significantly modify the conclusion regarding the general qualitative behavior based on (2-75). Short of an exact solution to (2-70), we will proceed to examine some of the possible implications of (2-75) subject to the various limitations mentioned (in particular, for the case of very weakly superconducting region and T near T_c'). When τ_*^{-1} approaches zero, (2-75) yields the usual London acceleration equation of (2-63) as expected for a thermodynamic equilibrium situation ($qU \equiv \tilde{\mu}_e = \tilde{\mu}_p$); whereas for $\tau_*^{-1} > \omega$, (2-75) gives the relaxation effect as would be expected by inspection of Eq. (2-57).

An understanding of the physical meaning of the relaxation time τ_s and its temperature dependence can be useful in considering the possible physical consequence of (2-75) later on. The meaning of τ_s becomes more transparent if it is expressed in terms of physically well understood parameters. At steady state $\dot{\phi} = \omega = 0$ we can identify the characteristic distance associated with the operation ∇^2 in $\nabla\cdot(\nabla n_s/n_s)$ of (2-73) with the healing length $[m\xi^2\sigma/(n_s q^2 \tau_*)]^{1/2}$ of the steady state Eq. (2-69). In terms of this healing length the relaxation time of (2-76) becomes

$$\tau_s \cong \frac{\sigma m}{n_s q^2} \quad . \qquad (2\text{-}77a)$$

Expressing the quasiparticle conductivity σ as a function of the quasiparticle density n and the quasiparticle (normal) relaxation time τ (as in a normal metal for T near T_c', 2.4.3), $\sigma = nq^2\tau/m$, results in

$$\tau_s \cong \frac{n}{n_s}\tau \quad . \qquad (2\text{-}77b)$$

This relation can be shown to be approximately correct at steady state from general transport considerations.[52] Thus at steady state the relaxation time τ_s for the perturbed condensate to revert back to the equilibrium superconducting state is directly proportional to τ and τ_s increases like the ratio of n/n_s which increases rapidly as temperature approaches the transition temperature ($n_s \sim [T_c - T]$). In addition, the ratio n/n_s can be fairly large in the very weakly superconducting region, although n and τ are nearly temperature independent over the

range of a fraction of a degree at liquid helium temperature.

In the non-equilibrium situation, since the detail spatial dependence of n_s and hence the characteristic healing length are not known, Eq. (2-77) will be used as a first order approximation of the relaxation time in (2-76) so that in the steady state limit τ_s has the proper functional dependence. The validity of this approximation improves especially in situations where the non-equilibrium state constitutes a small deviation from the equilibrium steady state. Thus within a scaling factor involving the ratio of the coherence length and the healing length in non-stationary state, the two relaxation times τ_s and τ_* can be used interchangeably in discussing the temperature-dependent behavior of the quantum phase difference in (2-75) in the weakly superconducting limit. For temperature near the transition temperature T_c' of the weak region, to first order approximation τ_s diverges like $(T_c'-T)^{-1}$.

In the usual Josephson effect (2-6) the term τ_s^{-1} in the denominator of (2-75) is identically equal to zero since it is assumed that there is no internal conversion or loss within the non-dissipating Josephson junction except for possible photon emission at $\Delta E = h\nu$. A vanishing $\tau_s^{-1}(\sim\tau_*^{-1})$ in (2-57) leads to an equilibrium Schroedinger equation for the superconducting wavefunction, and in (2-75) results in the equilibrium Josephson frequency-voltage relation for a harmonic potential as expected. This relaxation term is due to conversion loss in the dissipating proximity effect bridge as described by Rieger et al in their time-dependent GL equation.

All the assumptions and approximations made in arriving at Eq. (2-75) must be kept in mind in interpreting the result. Outside the non-equilibrium region, the pair and quasiparticle potentials $\tilde{\mu}_p$ and $\tilde{\mu}_e$ are equal and $\nabla\cdot\vec{j}_s$ is zero. Thus in this limit of thermodynamic equilibrium the term τ_s^{-1} in the denominator of (2-75) drops out, and (2-75) is just the equilibrium frequency-voltage relation as anticipated. Inside the non-equilibrium region at low enough frequency (or T sufficiently close to T_c') so that $\omega << \tau_s^{-1}$, (2-75) becomes $\Delta\tilde{\phi} \sim \tau_s U'$. In this nearly steady state (or nearly normal state), it is easier to interpret this result by taking the gradient of this expression: $\nabla\tilde{\phi} \sim \tau_s \nabla U'$ which becomes $j_s \sim \sigma\nabla U \sim -\sigma\vec{E}$ by using $j_s = n_s q\hbar\nabla\tilde{\phi}/m$ and (2-77a). This rather curious result arises since in this very weak region, $j_n >> j_s$, the normal current gives a potential gradient proportional to $+\sigma\vec{E}$ and the supercurrent gives a potential gradient proportional to $-\sigma\vec{E}$ or a <u>decrease</u> in dissipation. Thus this time-dependent GL theory gives a basis for the two fluid model in a weak superconductor (2.4.4) where the dissipation voltage U is given by the product of R and the total current I, IR, <u>less</u> an amount $v_s = RI_s$, i.e. $U = I_n R = (I-I_s)R$. And eventually as τ_s approaches infinity (which occurs at $T = T_c'$), in this limit of $\tau_s^{-1} > \omega$ the expression $\Delta\tilde{\phi} \sim \tau_s U'$ suggests a loss of quantum phase coherence as in the case of a normal metal where random oscillations of a macroscopic number of normal electrons lead to practically complete cancellation of the phase of different electrons.

In the high frequency limit or on a time scale ω^{-1} short relative to τ_s the unperturbed superconducting state inside the non-equilibrium

region does not have enough time to respond to the external perturbation and remains essentially in its initial state. In this limit (2-75) again gives the London relation for a harmonically driven potential (Eq. 2.4 or 2-63). In between these two limits when the frequency ω is comparable to τ_s^{-1}, large dispersion effects of the phase difference may occur in non-equilibrium S/N interface region. Such effects, as suggested by (2-75), are produced by relaxation processes driven by a potential difference U in a non-equilibrium region.

In order to take into account these non-equilibrium effects in quantum interference, we extend the above results across a single S/N interface to S/N/S structures in the very weakly coupled limit such as a proximity effect bridge with a relatively short (compared to the dimension of the strong regions on both sides of the bridge) normal region typically < 1μ. For such a short bridge the breakdown of phase coherence across the bridge is most likely to occur at the center of the weakened region where the two wavefunctions from both sides of the bridge taper off in the weak region and overlap to form the weakest spot (point 0) in the bridge (Fig. 2.13a). If $\Delta\tilde{\phi}_1$ is the phase difference between point 0 in the bridge and a point L in the equilibrium superconductor to the left of the bridge by traversing along a counter-clockwise path in the ring (Fig. 2.13b), then we have

$$\Delta\tilde{\phi}_1 = \tilde{\phi}_1(L) - \tilde{\phi}_1(0) = \frac{U'_{L0}}{-i\omega + \tau_s^{-1}} \quad , \qquad (2\text{-}78a)$$

where U'_{L0} is the normalized potential difference between points L and 0 along the same path as $\Delta\tilde{\phi}_1$. Similarly the phase difference $\Delta\tilde{\phi}_2$ taken

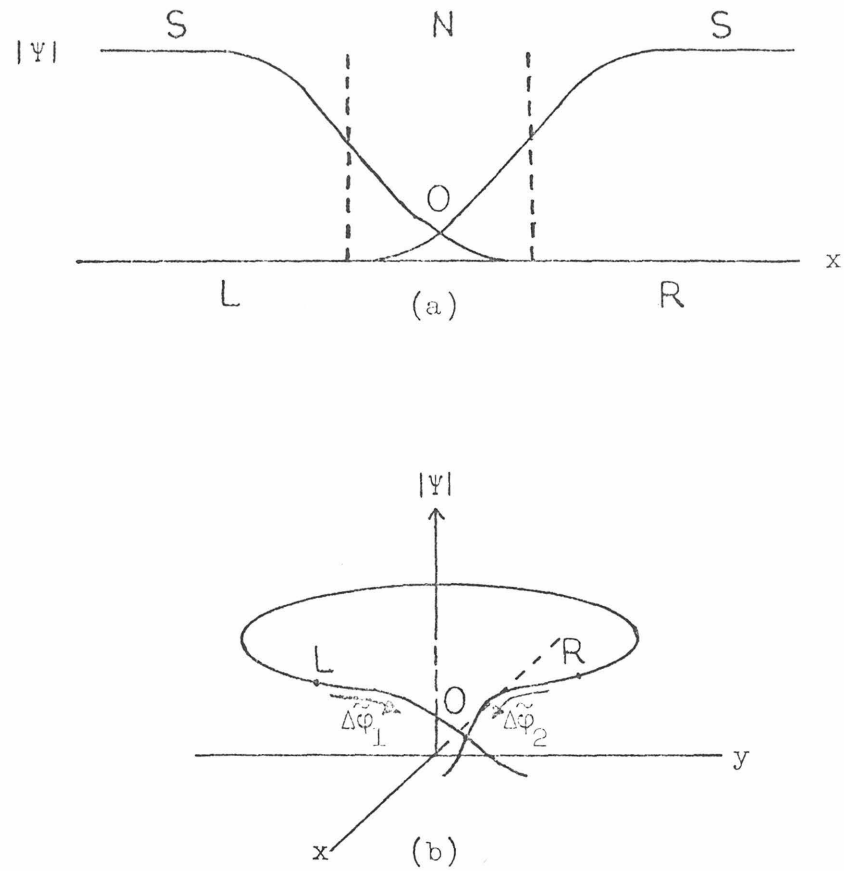

Fig. 2.13 Schematic diagram of the spatial dependence of the magnitude of the order parameter $|\Psi|$ of a proximity effect bridge (a) and a semiconductor interferometer (b). The wavefunctions from the adjoining strongly superconducting regions taper off in the bridge region and overlap to form the weakest spot (A) in the bridge.

between points 0 and R (Fig. 2.13) along a clockwise path in the ring is related to the respective potential difference U'_{RO} as

$$\Delta\tilde{\phi}_2 = \tilde{\phi}_2(R) - \tilde{\phi}_2(0) = \frac{U'_{RO}}{-i\omega + \tau_s^{-1}} \quad . \qquad (2\text{-}78b)$$

By taking the difference of the two equations, the phase difference $\Delta\tilde{\phi}(0) = \tilde{\phi}_1(0) - \tilde{\phi}_2(0)$ between the two "tails" of the same wavefunction, which are brought together at the bridge region in this configuration of an interferometer, is then given by

$$\Delta\tilde{\phi}(0) = \Delta\tilde{\phi}_{LR} + \frac{U'_{LR}}{i\omega - \tau_s^{-1}} \quad . \qquad (2\text{-}79)$$

where $\Delta\tilde{\phi}_{LR} = \tilde{\phi}_1(L) - \tilde{\phi}_2(R)$ is the phase difference maintained outside of the bridge region, and $U'_{LR} = U'_{LO} - U'_{RO}$ is the harmonic voltage which exists across the bridge.

For an rf inductively coupled interferometer, with the quantum effect v_s much smaller than the classical emf, U is essentially determined by the classical emf, $U = -i\omega\Phi_x$ and $\Delta\tilde{\phi}_{LR} = \Phi'_x + \Phi'_{dc}$ (for the time being, drop the factor R/Z in $(R/Z)\Phi_x$). Thus the effective phase difference to be used in this voltage biased situation -- include nonequilibrium effects -- is

$$\Delta\tilde{\phi} = \Phi'_{dc} + \Phi'_x - \frac{i\omega\Phi'_x}{i\omega - \tau_s^{-1}} = \Phi'_{dc} + \frac{\Phi'_x(t)}{1 - i\omega\tau_s} \quad . \qquad (2\text{-}80a)$$

This relationship indicates that whenever the frequency is higher than the reciprocal relaxation time, the response of the relative quantum phase will be diminished from the Josephson value and shifted in time-phase relative to the drive flux $\Phi_x(t)$. It is this nonequilibrium effect which we suggest may lead to the observed phenomena in Fig. 2.11

through the temperature dependence of τ_s. Keeping all the assumptions and approximations as in (2.4.5) except allowing for possible splitting of $\tilde{\mu}_p$ from $\tilde{\mu}_e$ in the nonequilibrium region and substituting $\Phi_x(t) = \Phi_x \sin\omega t$, Eq. (2-80a) becomes

$$\Delta\tilde{\phi} = \Phi'_{dc} + \gamma\Phi'_x \cos\omega t + \frac{\gamma}{\omega\tau_s} \Phi'_x \sin\omega t \quad , \qquad (2\text{-}80b)$$

where γ is defined as

$$\gamma = \frac{\omega\tau_s}{1 + \omega^2\tau_s^2} \quad . \qquad (2\text{-}81)$$

In the equilibrium case the supercurrent depends sinuosidally on the phase difference $(\Phi'_x \sin \omega t + \Phi'_{dc})$ as shown in (2-27). In the non-equilibrium case the sinusoidal dependence of I_s has contributions from both the sine and cosine terms of (2-80) plus the dc flux term. The two terms in (2-80) arise from the non-equilibrium interconversions of the pairs and quasiparticles and manifest themselves in the phase dependent supercurrent as an interference of the two "tails" of a wavefunction at the bridge. Substituting (2-80) into (2-27) for the time integral of U' leads to an expression for the quantum variation of I_s at the drive frequency as analogous to (2-32) for $\omega\tau_s < 1$

$$\delta I_s \cong \frac{2v_s}{Z} J_1\left(\frac{R}{Z}\gamma\Phi'_x\right) J_o\left(\frac{R}{Z}\frac{\gamma\Phi'_x}{\omega\tau_s}\right) \sin\Phi'_{dc} \quad . \qquad (2\text{-}82)$$

In the limit of $R >> \omega L$ the factor $J_1(\Phi'_x)$ in (2-34a) is replaced by $J_1(\gamma\Phi'_x)\, J_o\left(\frac{\gamma\Phi'_x}{\omega\tau_s}\right)$, and for $\omega L >> R$ the first order Bessel function in

(2-32b) is replaced by $J_1\left(\gamma \frac{R\Phi_x'}{\omega L}\right) J_0\left(\frac{\gamma}{\omega\tau_s} \frac{R\Phi_x'}{\omega L}\right)$.

The data of Fig. 2.11 represent measurements of the maximum amplitude of $\delta I_s(\tau_s)$, which were done by optimizing the drive flux Φ_x at each temperature to maximize J_1 and the dc magnetic flux. In this way $\gamma\Phi_x$ was kept approximately constant ($\gamma R|Z|^{-1}\Phi_x' \sim 0.6\pi$) as a function of temperature and the data should reflect the temperature dependence of $J_0(0.6\pi/(\omega\tau_s))$. These measurements were made at 10 and 30 MHz, and the periodicity of the data scales as ω^{-1} as expected. Except very near the transition temperature, these frequencies should lead to $\omega\tau_s < 1$ for any superconducting relaxation process and τ_s can be estimated from (2-82) to be of the order of (2-3) x 10^{-9} sec in order to be able to observe several oscillations at these frequencies.

In the temperature ranges of Fig. 2.11, as the temperature decreased, the rf drive amplitude was increased by about a factor of 1.5-2 which is consistent with the increase in Φ_x required to maintain the argument of J_1 constant in this temperature range. Experimentally the rate of oscillation in temperature increases with decreasing temperature and is in agreement with the J_0 factor of Eq. (2-82). As the temperature is lowered, the envelope of the maximum signal amplitude increases like the critical current.

The temperature dependence of the relaxation time is consistent with that of the quasiparticle branch mixing time τ_Q, i.e., $\tau_s(T) \tilde{=} \tau_s(0)(1 - t)^{-1/2}$ where $t \equiv T/T_c'$. The transition temperature T_c' can be estimated to be the temperature at which the envelope of the modulation

signal vanishes, e.g. in the case of the result shown in Fig. 2.11a, T_c' is estimated to be about 4.1°K. Using the value of $\tau_Q(0) \cong 0.65 \times 10^{-10}$ sec determined from dc measurements on similar structures for $\tau_s(0)$,[20] $\tau_s(\sim 0.99\ T_c')$ is found to be $\sim 0.7 \times 10^{-9}$ sec. The experimentally measured value for $\tau_s(T)$ can be estimated by the following method: since half of a period of J_0 corresponds to a variation of its argument by $\sim\pi$, the relaxation time at T near T_c' ($\sim 2\text{-}3 \times 10^{-9}$ sec) is obtained by equating $0.6\pi/(\omega\tau_s) \sim \pi$ for the argument of J_0. It is difficult to determine the relaxation time more accurately with this method due to the uncer - tainty of the value of T_c'.

The first few peak values of $J_1(z)$ are about +0.6, -0.35, +0.3 and -0.2 corresponding to z of about 1.8, 5.3, 8.6 and 11.8, and are referred to respectively as the first, second, third, and fourth Bessel-like peaks respectively. Since at low temperature the effect of critical flux sets in, the signal is proportional to $zJ_1(z)$ as given by Eq. (2-43). Thus at low temperature instead of the first peak being the maximum amplitude of all the Bessel-like peaks, it is the nth peak ($n > 1$) which has the maximum amplitude as is evident at T_4 of Fig. 2.8.

For interferometers with transition temperature $T_c' < 4.2$°K (the boiling point of liquid helium at 1 atm.) it is possible to conveniently observe the initial onset of the critical current I_c. In such situations the envelope of the Bessel-like peaks typically increases rapidly with decreasing temperature due to the initial exponential temperature dependence $(T_c' - T)$ of I_c in the factor $v_s(= RI_c/2)$ multiplying the two Bessel functions (J_1 and J_0). Figure 2.11a shows the variation of the

first Bessel-like peak as a function of temperature in the temperature range corresponding to T_1 and T_2 of Fig. 2.8. In addition, the observed frequency dependence of the oscillation signal as a function of temperature agrees with the ω^{-1} factor in the argument of J_o. Experimentally for the same interferometer (#2) measured at different frequencies (10 and 30 MHz) the period of the signal as a function of temperature is directly proportional to the rf frequency as predicted by the analysis. As the rf frequency is decreased from 30 to 10 MHz, the observed signal changes from a predominantly FM to an AM effect as indicated in Fig. 2.11b and c due to a corresponding increase of the $R/(\omega L)$ ratio.

However the envelope of the first Bessel-like peak signal as shown in Fig. 2.11c decreases with decreasing temperature. This is not inconsistent with the observation made on interferometer #1 (Fig. 2.11a) and the conclusion reached in the preceeding paragraph if we take into account the temperature range (relative to T_c' of this interferometer, #2) over which the observation was made. Experimentally it was observed that near 4.18°K the first Bessel-like peak gave the maximum signal amplitude, whereas near 4.05°K it was the nth ($n \sim 30$) Bessel-like peak which exhibited the largest amplitude. Figure 2.11c shows the variation of the signal of interferometer #2 with $T_c' > 4.2$°K in a temperature range corresponding to T_3-T_5 of Fig. 2.8 at 10 MHz, and hence the amplitude of the first Bessel-like peak decreases with decreasing temperature. This explains the apparent (but not a real) discrepancy between Fig. 2.11a and c for the temperature dependence of the first Bessel-like peak.

In going from 30 MHz to 10 MHz (Fig. 2.11b and c) for the same interferometer (#2 with $\omega L >> R$ at 30 MHz) the argument of $J_1\left(\frac{R}{\omega L}[\Phi_x'-\Phi_c']\right)$ of Eq. (2-43) increases because of its frequency dependence, and in order to give the same Bessel-like nth peak as at 30 MHz the effective flux $[\Phi_x'-\Phi_c'(T)]$ must decrease accordingly. In addition to a decrease in the drive flux (Φ_x) as discussed earlier, a reduction of the effective flux can also be achieved by an increase of the temperature-dependent (and thus shielding current dependent) critical flux Φ_c. Since the critical flux decreases with increasing temperature, in this sense the same interferometer appears to start working at a higher temperature when operated at 10 MHz than at 30 MHz. And hence at the same absolute temperature (say, 4.05°K in this example) while at 30 MHz the second Bessel-like peak gives the maximum signal amplitude, at 10 MHz the maximum amplitude comes from the nth ($n >> 1$) peak which is usually expected to occur near the lower end of the operating temperature range of an interferometer (Fig. 2.8). Such effect has also been observed when the same interferometer is tested at 30 MHz and 100 MHz.[53]

Finally, the dc magnetic response is not affected by the non-equilibrium interference in this analysis (2-82) which is entirely consistent with the experimental observation.

These non-equilibrium interference effects show up more prominantly and over a wider range of temperature in the shorter bridges (~ 0.7μ long). Experimental observation also seems to indicate that the oscillation

"period" of the signal as a function of temperature may be inversely proportional to the normal resistance of the bridge, R. These two points agree with the model proposed in this section (2.5) and can be inferred from the analysis by relating τ_s with the resistance R, the length ℓ, the cross section area A, and the supercurrent of the bridge. In terms of the bridge parameters the relaxation time in (2-77a) can be written as follows

$$\tau_s^{-1} = \frac{n_s q^2}{m} \cdot \frac{RA}{\ell} \quad . \qquad (2\text{-}83)$$

Since the supercurrent is proportional to $n_s(T)$ which increases with decreasing temperature, for a shorter bridge the argument of J_o in (2-82), $(\omega\tau_s)^{-1}$, is relatively larger and thus allows more oscillations in temperature to show up. Physically a shorter bridge also implies a relatively stronger overlap of the two "tails" of the wavefunction in the bridge region and hence a wider range of temperature over which these non-equilibrium interference effects can occur (Fig. 2.13a). Since the oscillation "period" in temperature for a given rf frequency scales like $\tau_s \propto R^{-1}$, in general this "period" is expected to increase with decreasing normal resistance of the bridge as observed (Fig. 2.11a and b).

Thus the temperature-modulated signal near the transition temperature as reported in Section (2.4.7 D) can be interpreted in terms of a non-equilibrium quantum interference such as discussed in this Section (2.5). It is the constructive and destructive interference of the two terms in (2-80) of the quantum phase difference across the bridge of

an interferometer, which gives rise to the observed temperature-modulated signal and is attributed here to the non-equilibrium interference phenomenon. Consequently the Josephson frequency-voltage relation (2-4) is modified by such non-equilibrium processes according to (2-61) and may be manifested on a macroscopic scale.

REFERENCES

1. F. London, Proc. Roy. Soc. (London), A152, 24 (1935).
2. B. D. Josephson, Phys. Lett., 1, 251 (1962).
3. P. G. de Gennes, Rev. Mod. Phys., 36, 225 (1964).
4. P. W. Anderson and A. H. Dayem, Phys. Rev. Lett., 13, 195 (1964).
5. H. A. Notarys and J. E. Mercereau, J. Appl. Phys., 44, 1821 (1973).
6. P. W. Anderson, Lectures on the Many-Body Problem, Ravello, 1963, Vol. 2, Ed. E. R. Caianell. (Academic Press, 1964), p. 115.
7. F. London, Superfluids, Vol. 1, Wiley, New York, 1950.
8. C. J. Gorter and H. G. B. Casimir, Phys. Z., 35, 963 (1934).
9. V. L. Ginzburg and L. D. Landau, J. Exptl. Theoret. Phys. (USSR) 20, 1064 (1950).
10. H. Fröhlich, Phys. Rev. 79, 845 (1950).
11. L. N. Cooper, Phys. Rev., 104, 1189 (1956).
12. J. Bardeen, L. N. Cooper, and J. R. Schrieffer, Phys. Rev., 108, 1175 (1957).
13. L. P. Gorkov, Soviet Phys. J. E. T. P., 9, 1364 (1959).
14. L. P. Gorkov, Soviet Phys. J. E. T. P., 7, 505 (1958).
15. P. W. Anderson, N. R. Werthamer, and J. M. Luttinger, Phys. Rev., 138A, 1157 (1965).
16. C. S. Owens and D. J. Scalapino, Phys. Rev. Lett., 28, 1559 (1972).
17. M. Tinkham, Phys. Rev. B6, 1747 (1972).
18. W. H. Parker and W. D. Williams, Phys. Rev. Lett., 29, 924 (1972).
19. J. Clarke, Phys. Rev. 28, 1363 (1972).
20. M. L. Yu, Ph.D. Thesis, California Institute of Technology, 1974.

21. A. C. Smith, J. F. Janak and R. B. Adler, Electronic Conduction in Solids, McGraw-Hill, New York, 1967.

22. T. J. Rieger, D. J. Scalapino and J. E. Mercereau, Phys. Rev. Lett., 27, 1787 (1971).

23. F. London, Phys. Rev., 74, 562 (1948).

24. (a) B. D. Deaver, Jr. and W. M. Fairbanks, Phys. Rev. Lett., 7, 43 (1961).

(b) R. Doll and N. Nabauer, Phys. Rev. Lett., 7, 51 (1961).

25. J. Bardeen, Phys. Rev. Lett., 7, 162 (1961).

26. T. K. Hunt and J. E. Mercereau, Phys. Rev., 135A, 944 (1964).

27. J. R. Schrieffer, Superconductivity, Benjamin, New York, 1964.

28. R. C. Jaklevic, J. Lambe, A. H. Silver, and J. E. Mercereau, Phys. Rev. Lett., 12, 159 (1964).

29. S. Shapiro, Phys. Rev. Lett., 11, 80 (1963).

30. R. K. Kirschman, Ph.D. Thesis, California Institute of Technology, 1972.

31. J. Clarke, Phil. Mag., 13, 115 (1966).

32. J. Bardeen, Rev. Mod. Phys., 34, 667 (1962).

33. J. Bardeen and J. L. Johnson, Phys. Rev., B5, 72 (1972).

34. R. K. Kirschman, H. A. Notarys and J. E. Mercereau, Phys. Lett., 34A, 209 (1971).

35. S. K. Decker and J. E. Mercereau, Appl. Phys. Lett., 23, 347 (1973).

36. R. K. Kirschman, J. Low Temp. Phys., 11, 235 (1973).

37. J. E. Mercereau, Rev. Phys. Appl. 9, 47 (1974).

38. R. K. Kirschman and J. E. Mercereau, Phys. Lett., 35A, 177 (1971).

39. W. C. Stewart, Appl. Phys. Lett. 12, 277 (1968).

40. A. H. Silver and J. E. Zimmerman, Phys. Rev., 157, 317 (1967).

41. H. A. Notarys and J. E. Mercereau, Proc. 1969 Intern. Conf. on Superconductivity, ed. by F. Chilton (North-Holland, Amsterdam, 1971).

42. J. Bardeen, Rev. Mod. Phys., 34, 667 (1962).

43. T. J. Rieger, D. J. Scalapino and J. E. Mercereau, Phys. Rev., B6, 1734 (1972).

44. R. P. Giffard, R. A. Webb and J. C. Wheatley, J. Low Temp. Phys., 6, 533 (1972).

45. H. A. Notarys, R. H. Wang, and J. E. Mercereau, Proc. IEEE, 61, 79 (1973).

46. J. E. Mercereau, Rev. Phys. Appl., 5, 13 (1970).

47. R. S. Thompson and C. R. Hu, Phys. Rev. Lett., 27, 1352 (1971).

48. J. Clarke and J. E. Paterson, J. Low Temp. Phys., to be published.

49. A. Rothwarf and B. N. Taylor, Phys. Rev. Lett., 19, 27 (1967).

50. P. G. deGennes, Superconductivity of Metals and Alloys, Benjamin, N. Y., 1966.

51. F. Bloch, Phys. Rev., 2, 109 (1970).

52. G. Rickayzen, Theory of Superconductivity, Interscience, N. Y., 1965, Chap. 7.

53. H. A. Notarys, private communication.

54. D. W. Palmer and S. K. Decker, Rev. Sci. Instrum. 44, 1621 (1973).

PART II

APPLICATIONS OF SUPERCONDUCTING QUANTUM MAGNETOMETER

INTRODUCTION

The measurement of magnetic susceptibility has long been a standard technique used in the study of the physical-chemical properties of materials, particularly those containing ions of the transition metals such as iron, copper, and nickel, etc. A need has existed, however, for improved sensitivity for demanding experiments involving material available in small quantities and on weakly magnetic materials exemplified by a variety of metal-containing biochemical compounds.

Over the past decade Josephson's predictions[1] have been extensively examined and verified in minute detail by many experimenters. Out of this study has come a scientific base upon which a new superconducting quantum electronics is being developed in many laboratories. Part II of this thesis is a description of the development of a magnetometer instrument, based on principles of quantum superconductivity, which is now in routine use in our laboratory for magnetochemical measurements. For this purpose the high sensitivity of the superconducting interferometer (sensor) must be matched by very high standards of reproducibility, reliability and precision of measurement over a temperature range from room temperature to below 4.2°K.

As an illustration of the great potential for this magnetometer instrument, we will describe in Chap. 1 its application in magnetochemistry.

The role of metal ions in metalloproteins and information that can be obtained from magnetic susceptibility measurements will be outlined. The usefulness of this information depends on the accuracy of the measurements and the temperature range over which the measurement is carried out. A description of the instrument and its methods of use are given. Data taken with this magnetometer on several proteins are presented. Possible limitations on performance of future development of the magnetometer will be discussed.

In Chap. 2, applications of this magnetometer in other scientific disciplines are briefly cited, details can be found in the various publications mentioned therein. The measurement of remanent magnetization of rocks will be indicated in light of its implications in the study of the geologically ancient history of the earth's magnetic field - paleomagnetism. In physics, an experimental measurement of superconducting pair density above the transition temperature due to thermodynamic fluctuations will be indicated with emphasis on the requirements on the magnetometer.

CHAPTER 1

MAGNETOCHEMICAL STUDIES

1.1 The Nature of the Magnetobiochemical Problem

Transition metal ions usually play a central role in many metal-containing proteins as the active sites of biological molecules.[2] The metal ions can participate in oxygen and electron transfer, bring about structural changes and affect enzymatic activities. Iron and copper can act as oxygen carriers in non-enzymic proteins such as hemoglobin, hemerythrin and hemocyanin. There are at least forty known metalloproteins which contain either iron or copper and still others with molybdenum, manganese, cobalt, zinc, vanadium, etc.[3] They are involved in various important metabolic pathways such as the biosynthesis of DNA, electron transfer in photosynthesis and protein digestion.

The magnetic moment of a metal ion in any chemical substance is sensitive to the geometrical arrangement of the ion's nearest neighbors. Often, if there is more than one metal in a molecule, intramolecular antiferromagnetic coupling may be present. An accuracy of 0.1 μ_B/ion or better is usually needed for meaningful correlation between the geometrical arrangement and the magnetic moment as well as for an estimate of the magnitude of the exchange constant (usually of the order of 150°K) in the case of antiferromagnetism. The temperature range of interest lies between room temperature and liquid helium temperature around which contributions from zero field splitting to paramagnetism show up. Between these two limits, a temperature dependent magnetic moment may

arise due to either incomplete quenching of orbital angular momentum or low-spin-high-spin thermal equilibrium or antiferromagnetic coupling between neighboring ions.[4,5] Hence measurements of magnetic moments of metalloproteins can provide useful information about the electronic state and the conformation of the metal ions involved. The presence of paramagnetism is usually associated with the unpaired electrons. The absence or tight coupling of unpaired electrons can lead to diamagnetism. Two metal ions bridged by a non-metallic ion (e.g. oxygen or sulfur) are not at all uncommon and may give rise to antiferromagnetic behavior. A metalloprotein may often contain only one or a few metal ions in a molecule of molecular weight typically of 10^5 to 10^6. X-ray structure determination can take years to complete if a stable crystal can be grown.

In most proteins the diamagnetic contribution ($\chi_D \sim -6 \times 10^{-7}$ emu/cm^3) of the protein host is usually 10^2 - 10^3 times larger than the magnetic contribution from the metal ions. In the temperature range of interest an accuracy of about 0.1 μ_B/ion for a change of a few Bohr magnetons amounts to an accuracy of a few parts of 10^{-9} emu/cm^3 for the corresponding change of susceptibility of 10^{-7} emu/cm^3. Since most protein samples are available only in quantities of less than a few tens of milligrams, a static susceptibility instrument of very high reproducibility over a wide range of temperature is needed to detect such a small signal.

A magnetometer which meets all of these requirements by using different properties of superconductors has been developed: perfect

diamagnetism with the well known volume susceptibility $-(4\pi)^{-1}$ emu/cm^3 for calibration standard, persistent current to provide stable magnetic field and shielding as well as the basis for flux transformer, and flux quantization as the basis for high sensitivity magnetic sensor. One useful feature of this superconducting magnetometer is the capability of nulling the large diamagnetic contribution from the protein host by measuring only the temperature dependent part of susceptibility due to extremely dilute transition metal ions. This feature will be illustrated by data taken on hemerythrin.

1.2 The Superconducting Magnetometer and Its Performance

The basis for using single junction quantum interferometers as magnetometers is the periodic variation in modulation signal as the ambient magnetic field is changed slowly ($\sin(2\pi\Phi_{dc}/\Phi_o)$ factor discussed in Chap. 2 of Part I). The variations in ambient magnetic field are usually caused by the change in the temperature-dependent magnetization of a sample in a constant magnetic field. The magnetometer instrument, the procedures used in measurements, tests and performance of the instrument, and data taken on protein samples are given in the following reprint[6*].

---

*Arabic numerals adjacent to the Roman numerals of the reprint are chosen to be consistent with the Arabic numerals throughout the text of Chap. 1.

MAGNETOCHEMICAL STUDIES WITH A NEW ULTRASENSITIVE SUPERCONDUCTING QUANTUM MAGNETOMETER+

H. E. Hoenig*, R. H. Wang, G. R. Rossman, and J. E. Mercereau
California Institute of Technology
Pasadena, California

A magnetometer utilizing quantum superconductivity as the basis for the flux sensor element has been designed and used for biochemical susceptibility measurements in the temperature range from 1.5°K to 300°K. The sensitivity and reproducibility of this instrument have been tested by measurements on small amounts of material of well-known susceptibilities. Using this instrument the temperature dependence of the magnetic susceptibilities of oxy- and metaquohemerythrin have been measured and for the first time their anti-ferromagnetic components have been unambigiously resolved. From this data the exchange coupling constants between the two high-spin iron (III) atoms in each subunit have been determined to be -77 and -134 cm^{-1} respectively.

1.2.1 I. Introduction

Magnetic susceptibility measurements for years have been a standard technique used in chemical investigations of metal ion containing substances providing information about structure, oxidation states and bonding. A need exists, however, for improved sensitivity for demanding experiments on weakly magnetic biochemical compounds.

After discovery of the Josephson effect and quantum phase coherence in superconductors, it was soon realized that a new type of sensitive instrumentation could be developed which would detect very small changes in magnetic fields. Although at one time this possibility was drawn to the attention of workers in the chemical fields[1,2], the development of these capabilities has remained within the realm of low temperature physics.

A cryogenic quantum magnetometer system has been developed which employs the principles of quantum superconductivity for the sensor as well as superconducting magnets and shielding to provide the steady, noise free magnetic fields necessary for these sensitive measurements. Even in this early state of development, this scientific tool is already capable of measuring static susceptibilities over a broad temperature range with sensitivity and reproducibility unmatched by conventional techniques.

A description of the apparatus and its methods of use are given. Data taken with some previously characterized chemical substances are presented which demonstrate some of the special features of the system. Also the application of the system to measurements of proteins containing low concentrations of metal ions is demonstrated.

1.2.2 II. Experimental Apparatus

A simplified schematic diagram of the experimental arrangement is shown in Fig. 1 which also includes the essential electronic detection circuit. The specimen (A) is placed inside a thin extension of a glass dewar (B) surrounded by a superconducting solenoid (C) immersed in a liquid helium bath with its temperature stabilized to within 1 m°K. The details of the specimen region are shown in Fig. 2. The solenoid is enclosed by a superconducting shield and the dewars are mounted inside a Mu-Metal shield. The entire dewar system is shock mounted to minimize the effects of vibration. To provide adequate electromagnetic shielding, the entire experiment is carried out in an rf-shielded room.

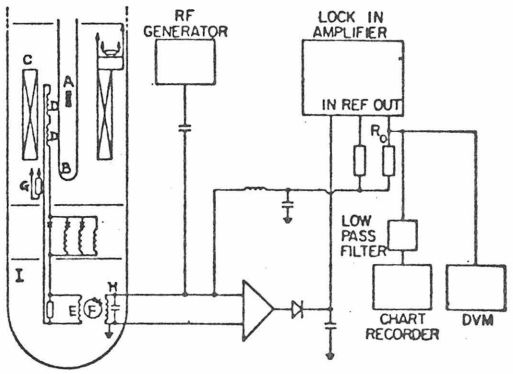

Fig. 1. Schematic diagram of the magnetometer including the electronic detection system: (A) sample, (B) inner glass dewar, (C) superconducting solenoid, (D) pick-up coils, (E) secondary coil of flux transformer, (F) superconducting sensor, (G) heat switch for flux transformer, (H) RF tank circuit, (I) superconducting sensor compartment. R_o is the feedback resistor.

Any change in the magnetic flux in the sample compartment (caused by either the introduction of the sample or a change in its susceptibility) is detected by two superconducting pick-up coils (D) which are constructed to automatically compensate the magnetization changes due to sample holder and its surroundings to within 0.15%. These coils and the secondary coil (E) comprise a dc superconducting flux transformer which transforms any flux change in the sample (A) to the superconducting sensor (F). A heat switch (G) is provided in the flux transformer line to open up the transformer circuit and isolate the sensor during large changes in the magnetic field of the solenoid. In this way the magnetic field around the sensor can be kept less than 1 mG. The flux transfer ratio was optimized for a three coil-system composed of the primary gradiometer coil around the sample, the secondary coil around the sensor, and leads that connect the primary to the secondary with inductances L_1, L_2 and L_3 respectively. From fluxoid conservation one can easily show that maximum flux transfer between sample and sensor occurs when

$L_2 = L_1 + L_3$ in the flux transfer relation

$$\frac{\varphi_2}{\varphi_1} = \frac{n_1}{n_2} \frac{L_2}{L_1+L_2+L_3}$$

where φ_1 and φ_2 are the fluxes through the primary and secondary coils respectively, and n_1, n_2 are the numbers of turns of primary and secondary coils respectively. To insure optimal flux coupling between the sensor and the flux transformer secondary, the secondary coil is wound directly around the thin film sensor and the length of the secondary coil exceeds that of the sensor. Our maximum flux transfer ratio has been 22% which is within a few percent of the theoretical limit. The flux transfer ratio (sensitivity of the system) can be changed from 0.2 to 10^{-4} in four steps by successively breaking superconducting wires which short out inductors placed in series with the pick-up coils. The superconducting sensor consists of a thin, cylindrical, superconducting film with one weak link due to a non-superconducting (normal) metal underlayer deposited on a 3-mm diameter glass rod. Both this ring and an rf tank circuit (H) which is inductively coupled to the ring are placed in a separate superconducting compartment (I) which further schields the electronics from unwanted external fields.

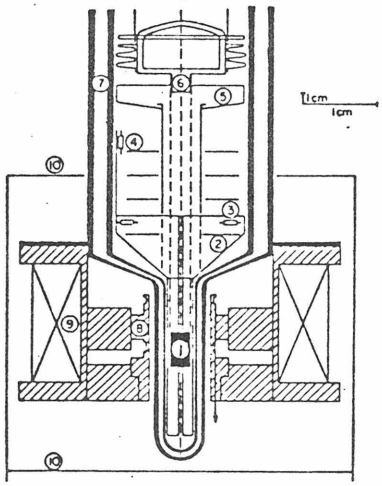

Fig. 2. Details of the sample region: (1) sample, (2) copper shield, (3) thermometer, (4) heater, (5) radiation shield, (6) connector for sample holder, (7) inner glass dewar, (8) flux transformer coils, (9) superconducting solenoid, (10) superconducting shield in He dewar.

The details of the operations of the sensor and the electronic detection system have been described elsewhere,[3,4] but since this is a relatively unfamiliar device, we give a brief description of the operation of the complete system. We start with the case where the feedback loop is open, i.e., R_o (in Fig. 1) is taken out. An rf current is introduced to the tank circuit at the resonant frequency ω. If, in addition, there is a low frequency sample-related flux Φ_{DC} enclosed by the ring, then the resultant Emf in the ring at frequency ω becomes a periodic function of the flux Φ_{DC} and is given by:[3]

$$\text{Emf} \propto \Phi_{rf}\omega J_1\left(\frac{2\pi\Phi_{rf}}{\Phi_o}\right)\cos\left(\frac{2\pi\Phi_{DC}}{\Phi_o}\right)\sin\omega t$$

where J_1 is the first order Bessel function, Φ_{rf} is the rf flux in the ring and the flux quantum $\Phi_o = hc/2e \approx 2.07 \times 10^{-7}$ G·cm^2. In the usual mode of operation the Emf is maximized by choosing the drive flux Φ_{rf} in such a way that the induced current in the superconducting sensor reaches the critical current of the weak link at the peak of each cycle, making $J_1 \simeq 1/2$. This Emf is then amplified and rectified to produce a dc "signal voltage" which is only a function of the sample-related flux Φ_{DC}:

$$V_{DC} \propto \omega\Phi_o \cos\left[2\pi\left(\frac{\Phi_{DC}}{\Phi_o}\right]\right.$$

Thus the signal is a periodic function of the sample-related flux with period Φ_o and the flux sensitivity is independent of the background field. Actually in order to eliminate dc drifts in the instrument the above dc signal is usually converted to low frequency ac by applying a small, low frequency modulation to the device. The amplitude of this ac signal is also periodic in Φ_{DC} as above. In order to linearize the system this signal is used to drive a feedback loop in such a way as to exactly compensate for flux changes due to the sample. The magnetometer is thus "locked on" to some specific value of the magnetic flux enclosed by the sensor. A change in the flux $\Delta\Phi_{DC}$ due to the susceptibility change in the sample is compensated by feeding the dc output signal of the lock-in amplifier back into the rf coil so as to generate an opposing field. The compensation current thus depends linearly on the flux change $\Delta\Phi_{DC}$. A digital readout of the voltage across the feedback resistor R_o can be accurately converted into the corresponding value of $\Delta\Phi_{DC}$ in terms of the flux quantum Φ_o since the Φ_o -voltage ratio can be determined to within one part in 10^4.

The response time of the sensor is roughly ω^{-1}, at least up to the gap frequency of the superconductor, $\omega \sim 10^{12}$, and thus is not a practical limitation. In the operation described here the response time was typically 1 sec and was set by requirements on the amplifier noise.

1.2.3 III. Experimental Procedures

At a fixed temperature and magnetic field, the total susceptibilities $\chi(T_o)$ and magnetic moments $\mu(T_o)$ are measured by moving the sample from one pick-up coil into the other with the phase and frequency of the signal remaining locked on. The output voltage of the lock-in amplifier is recorded. Digital data are taken at the initial and final positions of the sample. The signal can change beyond the range provided by the phase sensitive detector because a skip of an integral mul-

tiple of the flux quantum Φ_o is allowed and can be counted.

Changes of susceptibility as a function of temperature can be determined by first adjusting the sample position to be within the pick-up coil with the aid of the digital voltmeter read-out and then the sample temperature is changed with the phase sensitive detector locked-on while the system records changes in the flux at the sample. The background effect of the sample enclosure can be measured when the sample is moved out of the pick-up coil area. However, the effect of the sample holder is automatically compensated by the use of a long uniform synthetic quartz holder extending through both compensated pick-up coils. Thus accurate relative changes in susceptibility $\Delta\chi(T)$ and magnetic moments $\Delta\mu(T)$ can be made. The total susceptibility of the sample does not enter into the measurement. Thus small changes in strongly magnetic samples can be measured at the same sensitivity as small changes in diamagnetic materials.

For measurements in the range of 1.3°- 5.2°K, liquid helium is introduced into the inner dewar and the temperature is regulated by controlling the helium vapor pressure. For investigations in the temperature range of 2° to 300°K, a copper foil of high thermal conductivity and high purity surrounds the sample which provides a uniform temperature distribution around the sample area and allows one to make remote temperature changes and measurements. The sample is first cooled down to 2°K (approximately the temperature of the helium bath under working conditions) by first introducing about 10^{-3} torr of helium exchange gas into the vacuum space of the inner dewar and about 10 torr of purified coupling gas in the inner dewar. To raise the temperature of the sample, the helium exchange gas in the dewar vacuum space is removed by a helium cryogenic adsorption pump. Above 20°K an electrical heater is used to raise the temperature of the sample by warming the copper foil which surrounds the sample.

1.2.4 IV. Tests of the System

The flux transformer was initially calibrated with a superconducting sample which has the well established volume susceptibility, $-1/(4\pi)$ emu/cm^3 characteristic of superconducting metals. The detection system is calibrated by determining the Φ_o to voltage ratio.

Tests of the system have been performed with chemical compounds of well known susceptibilities to demonstrate the ability of the system in obtaining data with small quantities of materials. The temperature dependence of the susceptibility for a randomly oriented single crystal of 164 microgram of hydrated copper sulfate was determined in a magnetic field of 47 G (not kG). In figure 3, the susceptibility data for $CuSO_4 \cdot 5H_2O$ are plotted versus temperature. The data points represented by solid circles are total susceptibility points while the open circles come from relative measurements with respect to the 38°K point. From a similar plot of inverse susceptibility versus temperature one can derive the magnetic moment $\mu(6^oK) = 1.81 \pm 0.02\mu_B$/copper(II) ion and a Curie-Weiss temperature $\theta = (0.6 \pm 0.2)^oK$ which compare favorably with data obtained with conventional systems for sample quantities four orders of magnitude larger.[5]

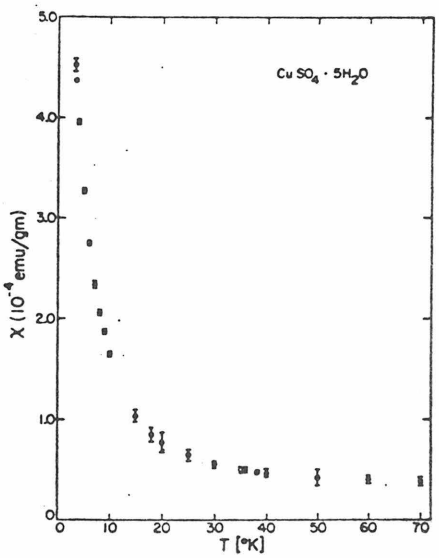

Fig. 3. Susceptibility versus temperature for 164 μg $CuSO_4 \cdot 5H_2O$ in a magnetic field of 47 G. Data shown as solid and open circles are obtained from measurements of total susceptibilities and susceptibility changes respectively.

The ability to work with near-zero susceptibilities has been similarly demonstrated by measurements on dimeric copper(II) acetate which in the solid state consists of pairs of antiferromagnetically-coupled copper ions. The day to day reproducibility of our instrument lies within the experimental scatter of a given run.

1.2.5 V. System Performance

The present sensitivity and reproducibility of this magnetometer for a typical 0.050 cm^3 sample in a magnetic field ranging from 12 G to 800 G are as follows: In the temperature range of 2° to 120°K the reproducibilities in relative changes of the volume susceptibility, $\Delta\chi(T)$, and the magnetic moment, $\Delta\mu(T)$, are $\pm$ 1.5 x 10^{-9}emu/cm^3 and $\pm$ 1 x 10^{-9}emu respectively for a sample whose total change in susceptibility is $\lesssim$ 1.2 x 10^{-5}emu/cm^3; for $\Delta\chi \gtrsim$ 1.2 x 10^{-5}emu/cm^3 the reproducibility in $\Delta\chi(T)$ is $\pm$ [4 x 10^{-4} x $\Delta\chi(T)$]. At higher temperature, the reproducibility is mainly limited by the background magnetism contribution due to construction material. For total absolute susceptibility measurements between 2° and 200°K where the sample is moved from one coil into another, the reproducibilities in $\chi(T_o)$ and $\mu(T_o)$ are $\pm$ 1.5 x 10^{-8}emu/cm^3 and $\pm$ 9 x 10^{-9}emu respectively for $\chi(T_o) < 4 \times 10^{-5}$emu/cm^3; and for $\chi(T_o) > 4 \times 10^{-5}$ emu/cm^3, [$\pm$ 4 x 10^{-4} x $\chi(T_o)$] and [$\pm$ 4 x 10^{-4} x $\mu(T_o)$] respectively. The uncertainties quoted here include all the background effects. The reproducibility is highest in the determination of

susceptibility changes $\Delta\chi(T)$. This feature is particularly useful in measuring materials which show small changes in a large susceptibility such as biological compounds. Metalloproteins usually have large diamagnetic backgrounds arising from the organic matter which do not contribute to the temperature dependent susceptibility one is interested in. Some examples of these are discussed below.

The present limitations on our system are related to the construction compromises which we have made in assembling this first apparatus and are not related to any intrinsic sensitivity limit. In fact, we are at least a factor of 10 less sensitive than the intrinsic sensitivity of our present sensor. And even this intrinsic sensitivity can be improved by modifying the amplifier-sensor system. Our design limits the sample size to a volume less than or equal to 0.2 cm^3. And though, while the system was designed for use with small samples, there is no fundamental limit to the size of the sample such as exists with some of the conventional techniques.

The principal sources of noise and background effects which now limit the performance are vibrations, flux-creep and the magnetic contribution of the construction materials. Trace amounts of ferromagnetic impurity or oxygen are especially troublesome. To reduce thermal fluctuations and magnetic disturbance from gas bubbles we usually operate our sensor immersed in liquid helium below the λ temperature. This procedure also maintains thermal equilibrium of the sensor in the presence of large temperature differences between sample and sensor. To maintain thermal equilibrium independent of the level of liquid nitrogen a copper radiation shield is inserted at nitrogen temperature between the helium and nitrogen dewars. The sample dewar is covered with a cloth "sock" which protects and supports a helium II film over a constant area of dewar surface independent of helium level. In this way large temperature differences can be maintained between sample and sensor while preserving a constant temperature at both the sample and sensor. Our present field limit of 800 gauss is determined by ambient vibration and flux creep.

1.2.6 VI. Biochemical Studies

The applications of magnetochemical techniques to problems in biochemistry is of interest for a variety of structural and mechanistic reasons.[6,7] The most obvious applications involve the study of the static susceptibility of metalloproteins which contain one or more transition metal atoms within a protein molecule whose molecular weight can approach 10^6. Much of the primary activity of the molecule is centered at these atoms. From the examination of their magnetic properties one can obtain informations about the oxidation state, the spin-state, the coordination environment, and about the existence of antiferromagnetic interactions among the metal atoms. Such studies require a susceptibility measuring system of high sensitivity because of the low concentration of paramagnetic ions in the diamagnetic protein host.

The iron containing protein, oxyhemerythrin, an oxygen carrier in lower invertebrates provides a challenging test of the magnetometer system. This protein has a molecular weight of 108,000 and contains only 0.81% iron distributed in eight identical subunits of the protein, each containing two iron atoms. Previous attempts to measure the susceptibility of oxyhemergythrin were unable to detect any temperature dependence in the susceptibility leading to the postulation of strong antiferromagnetic coupling between pairs of iron ions.[8,9]

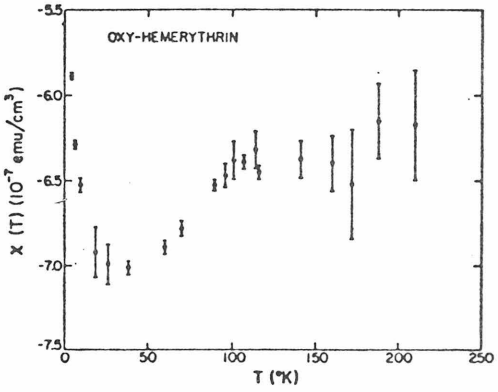

Fig. 4. Susceptibility versus temperature for 0.162 ml of an alcoholic suspension of oxyhemerythrin containing 460 μg of iron at 47 G. The meaning of the solid and open symbols is the same as in Fig. 3.

The temperature dependence of the susceptibility of 0.162 ml of a suspension of oxyhemerythrin containing a total of 460 μg of iron measured in a field of 47 gauss is presented in figure 4. Again the solid data points correspond to measurements of the total susceptibility, the others to relative measurements. The corresponding temperature dependence of the magnetic moment per Fe-ion is shown in Fig. 5 which is obtained by assuming that the rise in susceptibility below $40^{\circ}K$ is due to paramagnetic impurities. The susceptibility contribution of these impurities has been subtracted out assuming Curie-law behavior with $C = 4.94 \times 10^{-7}$ $^{\circ}K$-emu/cm^3. The results clearly indicate the presence of antiferromagnetic contribution to the susceptibility. A similar antiferromagnetic behavior has also been measured in metaquohemerythrin. A full discussion and interpretation of the hemerythrin results in connection with chemical and optical properties appears elsewhere.[10]

VII. Conclusion

A new experimental technique for measurements of the temperature dependence of magnetic susceptibilities of biochemicals in the temperature range

of 1.5° to 300°K has been developed based upon new principles of measurement using superconducting electronics. A superconducting quantum magnetome-

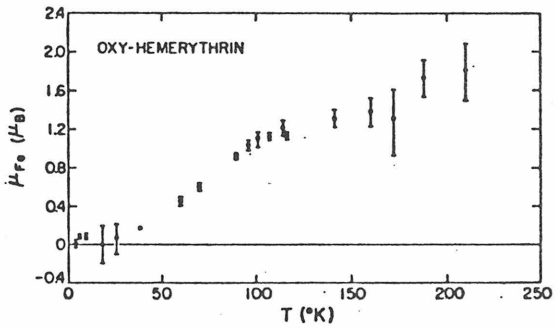

Fig. 5. Magnetic moment per Fe-ion versus temperature for 0.162 ml of an alcoholic suspension of oxyhemerythrin containing 460 μg of iron at 47 G assuming paramagnetic impurities with a Curie constant $C = 4.94 \times 10^{-7}$ °K-emu/cm^3.

ter system using these techniques has been built which when applied to a variety of measurements provided results with an accuracy which compares favorably with those obtained by using conventional methods of magnetic susceptibility determination. The unsurpassed sensitivity of the system opens a new realm of magnetic measurements on weakly magnetic materials. Already data have been obtained on biochemical compounds which were unmeasurable with previously existing techniques. The method is still in its infancy and unlike conventional techniques shows great promise for considerable improvement in sensitivity and convenience.

We wish to thank Dr. H. A. Notarys for several helpful discussions.

References

1. D. J. Matisoo, Anal, Chem. 41, 83A (1969).

2. D. J. Matisoo, Anal. Chem. 41, 139A (1969).

3. J. E. Mercereau, Revue de Physique Appliquee 5, 13 (1970).

4. M. Nisenoff, Revue de Physique Appliquee 5, 21 (1970).

5. R. J. Benzie and A. H. Cooke, Proc. Phys. Soc. (London) 64A, 124 (1951).

6. B. L. Valee and W. E. C. Wacker, The Proteins (ed. H. Neurath), Vol. V Metalloproteins, (Academic Press, New York, 2nd ed. 1970).

7. C. E. Johnson, J. Appl. Phys. 42, 1325 (1971).

8. H. B. Gray, Advances in Chemistry Series, No. 100, American Chemical Society, Washington, D. C. 1971, pp. 378-382.

9. T. H. Moss, C. Moleski, and J. J. York, Biochem. 10, 840 (1971).

10. J. W. Dawson, H. B. Gray, H. E. Hoenig, G. R. Rossman, J. M. Schredder, and R. H. Wang, Biochem. 11, 461 (1972).

---

† Work supported in part by the Office of Naval Research, Contract No. N00014-67-A-0094-0013 and the International Business Machines Corporation Grant No. 30058 and Deutsche Forschungsgemeinschaft.

* Present address: Physikalisches Institut der Universitaet, Frankfurt am Main, Germany.

1.2.7 Stereochemical Identification

In the preceding reprint the non-destructive measurement of magnetic susceptibility was shown to be useful in deducing the type of coupling between the two iron ions in oxy-hemerythrin. As a second example, the susceptibility data were used in the identification of certain stereochemistries, whether a metal ion is in an octahedral or a tetrahedral or some other environment.[7]

The enzyme carboxypeptidase A (CPA, Mol. Wt. 34,900) is present in the pancrease of mammals where it removes the C-terminal amino acid from peptide chains ingested as food. Each native protein molecule contains a zinc ion which is essential for its enzymatic activity.[8] Three positions of the distorted tetrahedral coordination around the zinc ion are occupied by ions from the protein, and the fourth position is the binding site for a substrate or a water molecule.[9]

The "entatic" site hypothesis proposes that the catalytic action of CPA results at least in part from the strained or distorted coordination sphere of the metal ion. Such distortion is said to produce a high energy configuration at the metal ion resembling a transition state.[10] One can substitute the diamagnetic Zn^{2+} ion by Ni^{2+}, Co^{2+} and Cu^{2+} among others.[9] While Co-CPA and Ni-CPA retain enzymatic activity, Cu-CPA has none. This loss of enzymatic activity has been taken as evidence in favor of the "entatic" site hypothesis since Cu^{2+} is known to prefer a different geometrical arrangement, i.e., a square planar coordination.

The magnetic moments of Ni-CPA and Co-CPA have been determined. The magnetic susceptibility of 14 mg of Ni-CPA containing 16.8 μg of Ni

was measured in the range of 2.5°K and 75°K at a field of 150 gauss using the "relative" mode of operation to remove the temperature independent contributions of susceptibility. The resulting temperature dependent paramagnetic susceptibility versus inverse temperature is shown in Fig. 1. The corresponding magnetic moment in units of Bohr magneton is determined to be $\mu_e = (2.53 \pm 0.10)\mu_B$/ion assuming that the deviation from Curie behavior below 10°K is due to possible contribution from zero field splitting. "Total" susceptibility measurement was carried out for 24.4 mg Co-CPA containing 29.7 μg Co at fields of about 40 gauss between 2°K and 130°K. After substracting out the temperature independent contributions, the susceptibility was plotted against inverse temperature (Fig. 2.) and the magnetic moment is $\mu_e = (4.77 \pm 0.15)\mu_B$/ion.

In light of ligand field calculations and overall magnetochemical evidence, both Ni-CPA and Co-CPA fall in the ranges for an octahedral coordination with magnetic moments of 2.8 - 3.2 μ_B and 4.7 - 5.2 μ_B respectively, whereas in a tetrahedral coordination their respective moments would be 3.2 - 4.0 μ_B and 4.3 - 4.7 μ_B. Thus contrary to the entatic site hypothesis, the Ni-(II) ion is seen to be in a six-coordinate environment and not necessarily have a high energy structure. The "irregular tetrahedral" coordination of the cobalt (II) ion proposed in this hypothesis[11] is not supported by the measurement of magnetic susceptibility. The spectroscopic results also support this conclusion.[12] A detail discussion of the nature of the ground states of Co(II) and Ni(II) CPA based on the magnetic and spectroscopic data has been published.[13]

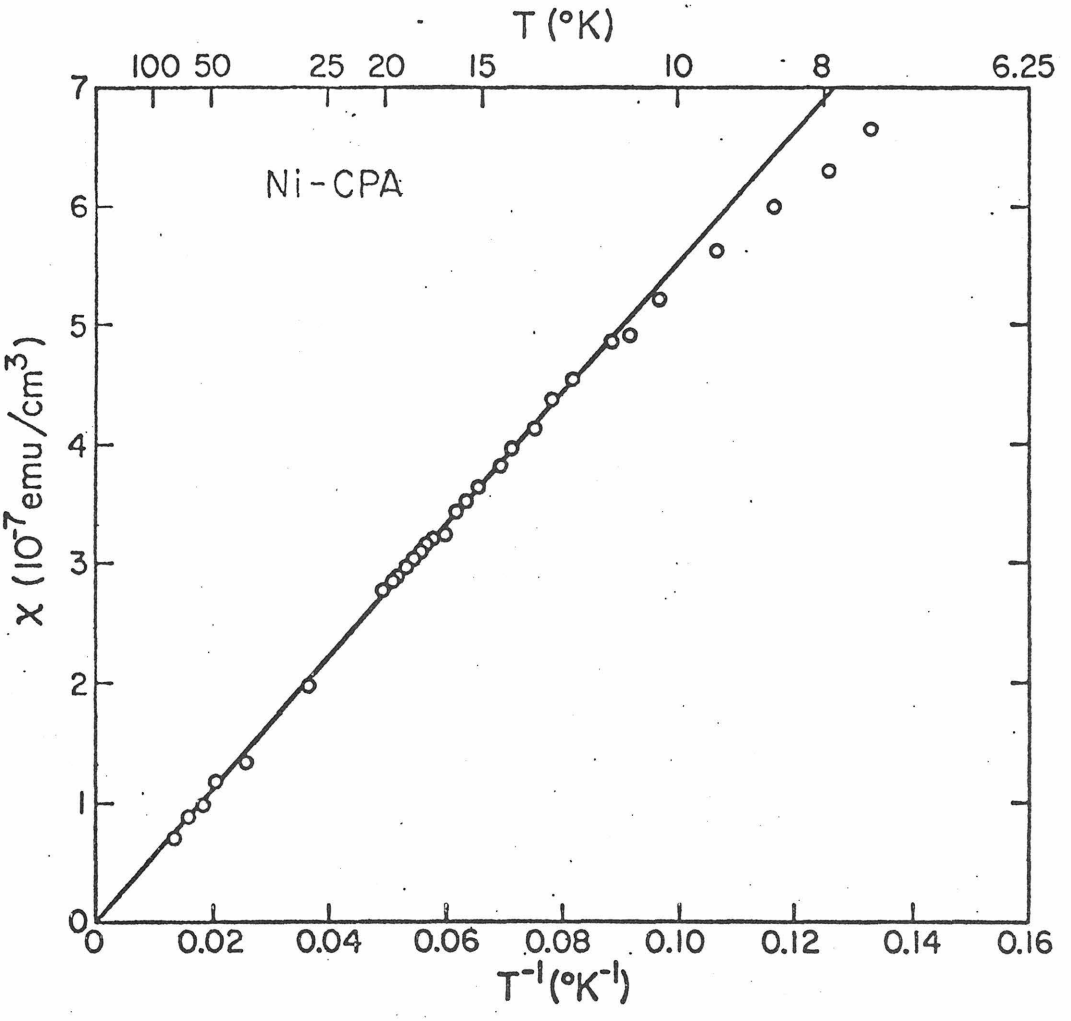

Fig. 1 Temperature dependence of the magnetic susceptibility (χ) of Ni(II)CPA in the range 8-75°K.

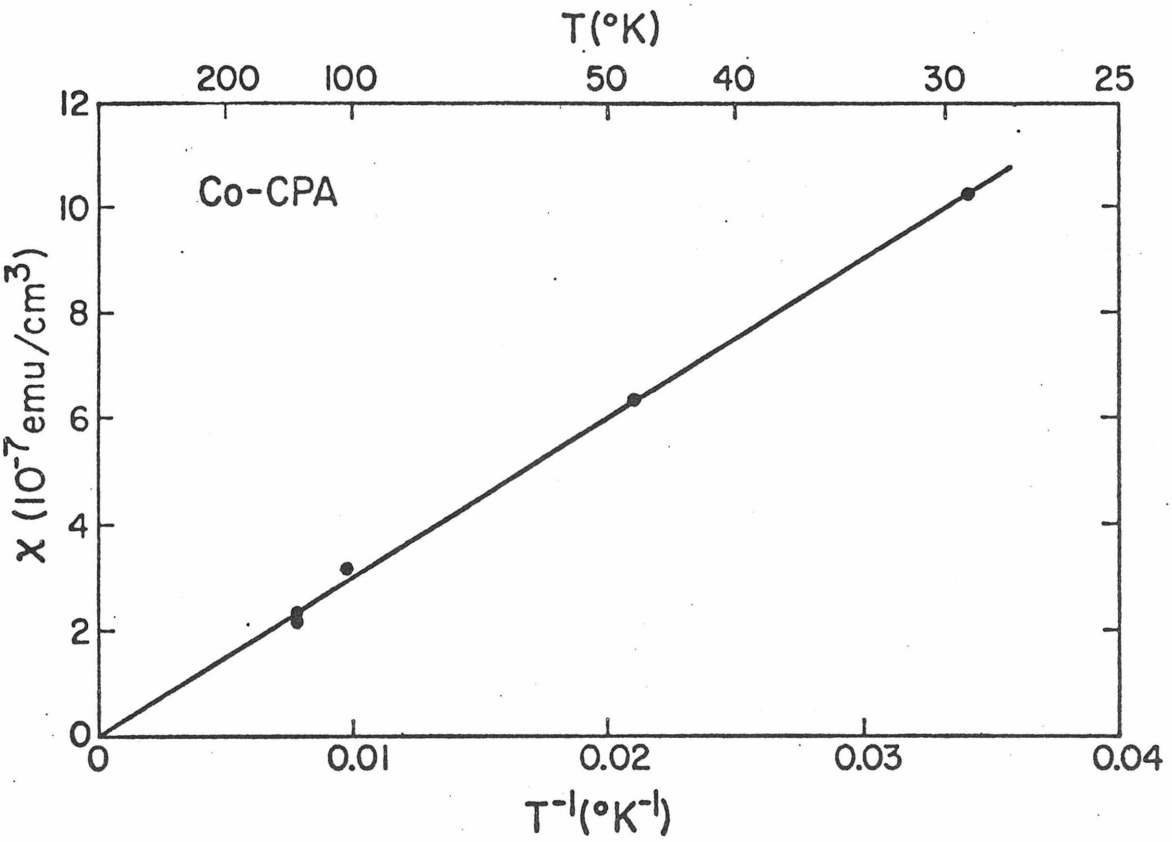

Fig. 2 Temperature dependence of the magnetic susceptibility (χ) of Co(II)CPA in the range 30-130°K.

With some modifications in the magnetometer and the experimental procedure it is possible to use this instrument in magneto-kinetic studies of reactions and flow systems. Such modifications are being undertaken in the investigation of possible dual roles of photoreception and photosynthesis in the purple membrane of Halobacterium Halobium.[14]

1.3 General Experimental Considerations

Besides the limitations mentioned in Ref. 6, a few additional effects of possible relevance to the operation and limitations of the instrument will be discussed.

1.3.1 The Effect of Temperature Variations on Penetration Depth

The change of penetration depth due to variations in the temperature is given by

$$\frac{\partial\lambda}{\partial T} = 2\lambda(T)\,\frac{t^3/T_c}{1 - t^4} \quad , \qquad (1\text{-}1)$$

where t is the reduced temperature defined as $t = T/T_c$. For a Niobium ($T_c = 9.22°K$, $\lambda(0) = 470$ Å) pickup coil of diameter 1 cm at 2°K and in a magnetic field of 200 Oe, the relative change in the magnetic field associated with a temperature variation of 1 m°K is about $\Delta H/H \sim 10^{-11}$. For a sample of cross-section area 0.1 cm^2 in such a pickup coil, the associated change in flux is $\Delta\Phi \simeq 10^{-3}\Phi_0$ at the pickup coil of the flux transformer.

1.3.2 Paramagnetic Materials and Thermal Contractions

Often electronic paramagnetic impurities in the vicinity of the pick-up coils can cause serious problems in certain susceptibility measurements.

The instrument operates by detecting magnetic flux within the volume enclosed by the sensor and as such measures a volume susceptibility. Since the sample is subject to thermal contraction, the volume susceptibility is in turn a function of temperature. The temperature dependent diamagnetic background is particularly noticeable in the case of frozen solutions which may undergo 10-20 per cent thermal contraction upon cooling. The problem is not serious for compacted powders since the packing density remains nearly constant.

The present sensitivity in the susceptibility measurement is about 10^{-11} emu/cm^3 for a given sample temperature. As far as the feasibility of a magnetometer of higher sensitivity (say 10^{-13} emu/cm^3) is concerned, all materials can be considered paramagnetic. Apart from electronic paramagnetism, a second effect of temperature variation is manifested in the nuclear paramagnetism of the construction material.[15] Since the nuclear susceptibility of copper is 4.3×10^{-8}°K-emu/cm^3, at 4°K a temperature difference of 0.1°K in the copper shield of diameter 3 mm and thickness 5 mil. can cause a change of flux $\Delta\Phi \simeq 10^{-4}\Phi_0$ at the pickup coil in a 100 Oe field. Temperature control and choice of construction materials are important for further improvement in sensitivity.

1.3.3 Johnson Noise and Eddy Current in Copper Shield

Johnson noise in the copper shield can give rise to a fluctuating magnetic fields and hence flux noise. By equating $\mu_0\Phi_n^2/L \cong 4\pi kTB\tau$, the flux noise Φ_n at the pickup coil for a cylindrical sheet of copper at a detection bandwidth B of 1 sec^{-1} is estimated to be $10^{-3}\Phi_0$ at

helium temperature where $\tau = L/R = 2\pi rt\ 10^{-7}/\rho$ (MKS unit) $= 2.5 \times 10^{-3}$ sec with radius r = 1.5 mm, thickness t = 0.13 mm and resistivity $\rho \cong 5 \times 10^{-9}$ Ω-cm. The length of the circumferential current sheet is taken to be that of the pickup coil (4 mm) for the largest noise. The flux noise is reduced by an order of of magnitude or more in a vertically slotted sheet due to reductions in both τ and coupling to the pickup coil. Another advantage of reducing τ is in making the effect of Eddy current in the copper shield at the audio modulation frequency negligible and hence not a limiting factor in improving the response time of the instrument if so desired.

With the possible exception of the noise due to temperature gradient in the copper shield between the two pickup coils, the other noise effects are probably not likely to be the limiting factors in the present magnetometer because these effects are compensated and reduced by three orders of magnitude due to the antisymmetric arrangement of the pickup coils. In any case, the noise detected by the superconducting sensor is reduced by a factor of the flux transfer ratio from the un-compensated noise in the pickup coils.

CHAPTER 2

PALEOMAGNETISM AND FLUCTUATION EFFECTS IN SUPERCONDUCTIVITY

2.1 Paleomagnetism

2.1.1 Reversal of the Earth's Magnetic Field

When igneous rocks are allowed to cool from above their Curie temperatures in a magnetic field, they acquire a weak but extremely stable remanent magnetization with direction parallel to and intensity proportional to that of the ambient magnetic field. If the magnetization is acquired by natural processes, it is referred to as natural remanent magnetization (NRM).[16]

From a large collection of NRM data, it has been found that approximately half of all rocks are reversely magnetized with respect to the earth's present magnetic polarity (defined to be the normal polarity). Remarkably few intermediate directions have been found. Less than five percent of reversals have been attributed to mineralogically controlled self-reversal. Geophysicists have generally agreed that reversals of the earth's magnetic field are the cause of magnetization reversals in most rocks. Magnetic polarity correlation in age from rocks all over the earth and the symmetric magnetic profiles with respect to the central anomaly in the midocean ridge system lend support to the theory of geomagnetic field reversal. The time required to complete a transition between different polarity states is estimated to be 10^3 - 10^4 years with intervals between polarity reversals of the order of 10^6 years.[17]

2.1.2 Paleomagnetism and Superconducting Magnetometry

The shape of the geomagnetic field is approximately that of a dipole with the magnetic dipole axis differing from the rotation axis by 5° to 25° upon averaging over thousands of years. The origins of the earth's field and especially its reversal are not well understood. The verification of the dipole nature and the tests of the theories put forward for the origins of field and reversals naturally depend on the quality and the quantity of data available. In addition, radiometric time scale using K-Ar decay for reversals is usually limited to the young rocks (about 10^6 years before present). A secondary time scale for geochronologic correlation based upon the field reversal information stored in natural magnetism of rocks does not suffer from the above time limit.[18]

Remanent magnetizations measurements on cubic rock samples of volume $(2\ mm)^3$ were made by using the magnetometer described in Chap. 1. Its field sensitivity is at least 2×10^{-8} G or equivalent magnetic moment sensitivity of 2×10^{-10} emu for a 1 sec time constant which is about two orders of magnitude better than the conventional spinner magnetometer. Significant field amplification by nearly two orders of magnitude is possible by using typical rock samples of volume $(1\ in.)^3$. A similar magnetometer with direct room temperature access and capable of measuring magnetizations along two orthogonal axes simultaneously is now in routine use with an effective thirty fold increase in the output rate of data over the spinner magnetometer.[18] The overall improvements in the collection of paleomagnetic data made possible by the superconducting quantum magnetometer may play a significant role in our

understanding of the dipole hypothesis, polar wondering, continental drift, and the origin and possible biological effects of field reversals.

2.2 Fluctuation Effects in Superconductivity

Thermodynamic fluctuations in superconducting pair density above the superconducting transition temperature represents the onset of local superconductivity. Superconducting fluctuations above T_c are known to cause a monotonic onset of superconductivity[20] as experimentally verified in the temperature dependence of the dynamical conductivity σ and the diamagnetic susceptibility χ_D: $\sigma \propto \chi_D \propto (T-T_c)^{-1/2}$ in the zero frequency limit.[21,22]

However, according to Schmid and Burgess,[24] the high frequency ($\omega \neq 0$) density fluctuations as a whole do not lead to such an onset of the mean superconducting pair density. For $T > T_c$, as the temperature increases, within the validity of G-L equations the decrease of the temperature dependent coherent length $\xi_{GL}(T) = \xi_0(T/T_c - 1)^{-1/2}$ gives rise to an increase of the mean superconducting pair density n_s as follows[23]

$$n_s = (m/\pi)\, k_B T/\xi_{GL}(T) \qquad T \gtrsim T_c \qquad . \qquad (2\text{-}1)$$

A plausible argument leading to Eq. (2-1) can be like this: At temperatures below T_c it is energetically favorable for a normal metal to be in the superconducting state. For $T > T_c$ it takes energy to form superconducting electron pairs. Since there is an amount of thermal energy kT available, this makes it possible for droplets of Cooper pairs

to grow and decay as a result of thermodynamic fluctuations. From the uncertainty principle the kinetic energy associated with a Cooper pair is about $\hbar^2/2m\xi_{GL}^2$. By equating the total kinetic energy $(n_s\xi_{GL}^3)\hbar^2/2m\xi_{GL}^2$ to the thermal energy k_BT, Eq. (2-1) can be obtained to within a constant of order unity.

Even under the most favorable condition (ξ_{GL} small), this increase of mean pair density with increasing temperature was shown to be a small effect.[25] A resolution of about 2 parts in 10^4 of the total susceptibility is needed. Using the superconducting magnetometer described in this thesis, the experimental results[26] indicate that indeed there is an increase of the mean superconducting pair density n_s as temperature increases above T_c, caused by thermodynamic fluctuations.

REFERENCES

1. B. D. Josephson, Phys. Lett., 1, 251 (1962).
2. B. L. Vallee and W. E. C. Wacker, The Proteins, H. Neurath, ed. Vol. V. Metalloproteins. (Academic Press, New York, 1970), 2nd ed.
3. E. Frieden, "The Chemical Elements of Life," Sci. Am., July 1972.
4. See for example: B. N. Figgis, Introduction to Ligand Fields, (Interscience, New York, 1965).
5. A. Earnshaw, Introduction to Magnetochemistry, (Academic Press, New York, 1968).
6. H. E. Hoening, R. H. Wang, G. R. Rossman, and J. E. Mercereau, in Proc. Applied Superconductivity Conf. (Annapolis, Md., May 1-3, 1972).
7. M. Cerdonio, R. H. Wang, G. R. Rossman, and J. E. Mercereau, Proc. 13th Intern. Conf. on Low Temp. Physics, Boulder, Colorado, 1972.
8. B. L. Vallee, J. A. Rupley, T. L. Coombs, and H. Neurath, J. Biol. Chem. 235, 66 (1960).
9. J. A. Harsmith and W. N. Lipscomb, "Carboxypeptidase A" in The Enzymes, P. D. Boyer, ed., Vol. 3, Hydrolysis: Peptide Bonds, (Academic Press, New York, 1971), 3rd ed., p. 1.
10. B. L. Vallee and R. J. P. Williams, Proc. Natl. Acad. Sci. U.S., 59, 498 (1968).
11. S. A. Latt and B. L. Vallee, Biochem. 10, 4263 (1971).
12. C. Root and R. Rosenberg, private communication.
13. R. C. Rosenberg, C. A. Root, R. H. Wang, M. Cerdonio and H. B. Gray, Proc. Nat. Acad. Sci. U.S. 70, 161 (1973).

14. M. Delbrück, private communication.

15. E. P. Day, PhD Thesis, Stanford University, 1972.

16. D. W. Strangway, History of the Earth's Magnetic Field, (McGraw Hill, N. Y., 1970).

17. A. Cox, Science, 163, 237 (1969).

18. E. Shoemaker, private communication.

19. R. Uffen, Nature, 198, 143 (1963).

20. H. Schmidt, Z. Phys., 216, 336 (1968).

21. I. S. Shier and D. M. Ginsberg, Phys. Rev. 147, 384 (1966).

22. J. P. Gollub, M. R. Beasley, R. S. Newbower and M. Tinkham, Phys. Rev. Lett., 22, 1288 (1969).

23. A. Schmid, Phys. Rev. 180, 527 (1969).

24. R. E. Burgess, in Proc. of the Intern. Conf. on Fluctuations in Superconductors, Asilomar, Calif., 1968, ed. by W. S. Goree and F. Chilton (Stanford Research Institute, Menlo Park, Calif., 1968).

25. P. Fulde and S. Straessler, Phys. Rev. B1, 3017 (1970).

26. H. E. Hoenig and R. H. Wang, Phys. Rev. Lett., 27, 850 (1971).